DEM-CFD ANALYSIS OF MICROMECHANICS FOR DRY POWDER INHALERS

by

JIECHENG YANG

A thesis submitted to the University of Birmingham for the degree of

DOCTOR OF PHILOSOPHY

School of Chemical Engineering

University of Birmingham

April 2015

ABSTRACT

Dry powder inhalers (DPIs) are widely used for the therapy of respiratory and pulmonary diseases. In this study, a coupled discrete element method and computational fluid dynamics (DEM-CFD) is employed to investigate the micromechanics of carrier-based DPIs. The effects of van der Waals forces and electrostatic forces on the mixing process, and the influences of air flow and particle-wall impact on the dispersion process are examined.

For the mixing of carrier and active pharmaceutical ingredient (API) particles in a vibrating container, it is found that vibration conditions affect the mixing performance. While there is an optimal mixing condition to maximise the number of API particles attaching to the carrier (i.e. contact number) for van der Waals cases, the contact number decreases with increasing vibration velocity amplitude and frequency for electrostatic force cases. It is also revealed that van der Waals forces (short range) and electrostatic forces (long range) result in different mixing behaviours.

For the air flow induced and impact induced dispersion, it is found that the dispersion performance improves with increasing air velocity, impact velocity and impact angle, and reduces with increasing work of adhesion. The dispersion performance can be approximated using the cumulative Weibull distribution function governed by the ratio of air drag force to adhesive force or the ratio of impact energy to adhesion energy.

Keywords: dry powder inhaler, DEM-CFD, mixing, dispersion, micromechanics.

ACKNOWLEDGEMENTS

I would like to express my sincere gratitude to my supervisors, Prof. Chuan-Yu Wu and Prof. Michael Adams for mentoring me throughout my PhD study. They teach me how to carry out scientific work and grow as a professional researcher. Without their unreserved support and persevering help, this study would not have been completed so smoothly. I also wish to express my special thanks to Prof. Mostafa Barigou for his kind help during my PhD study.

I would also like to thank Dr. Yu Shen, Dr. Chunlei Pei, and other group members not only for their help on my project, but also for their accompany during my PhD study.

The financial supports from the Chinese Scholarship Council (CSC) and the School of Chemical Engineering at the University of Birmingham are gratefully acknowledged.

Finally, I would like to thank my family for their support and love.

TABLE OF CONTENTS

LIST OF FIGURES

LIST OF TABLES

CHAPTER 1: INTRODUCTION

1.1 Background

Dry powder inhalers (DPIs) have been widely used for treating pulmonary and respiratory diseases, since they have a number of advantages compared to other drug delivery approaches. DPIs can directly deliver drugs to the target areas, therefore they have a rapid onset of activity and they need smaller doses. DPIs are breath actuated and propellant free, so that they are more suitable for the elderly and children. In addition, DPIs provide more drug choices since they are useful for drugs that are poorly absorbed orally. Furthermore, DPIs contain no Freon and are environmentally friendly. Therefore, the DPI is considered as an important and promising method for pulmonary drug delivery (Aulton and Taylor, 2001; Islam and Gladki, 2008; Newman and Busse, 2002; Smith and Parry-Billings, 2003).

Since the active pharmaceutical ingredient (API) particles that can be directly delivered to the lungs and respiratory tracts are generally small (< 5 μm), they are extremely cohesive and have poor flowability (Pritchard, 2001). In order to improve the flowability and dispersion efficiency of DPI formulations, API particles are either mixed with large carrier particles or aggregated into large agglomerates to be transported more effectively, and then they need to be dispersed as fine particles so that they can be delivered to the lung and deep respiratory tracts. Therefore, particle-particle interactions such as van der Waals potentials, electrostatic interactions and capillary forces are of significant importance in controlling the performance of DPIs (Hinds, 1999). The

complicated nature of this process results in the relatively low efficiency of current DPIs (normally < 30%).

In order to improve the performance of DPIs, much research has been focused on the formulations, the design of the inhaler device and the patients' inspiratory manoeuvre, which are three main factors governing the performance (Jones and Price, 2006). The effects of particle size, particle concentration, particle morphology, particle surface roughness, particle density, and crystal form have been investigated experimentally (Kaialy *et al.*, 2012a; Kaialy *et al.*, 2012b; Kaialy and Nokhodchi, 2012; Kaialy *et al.*, 2012c; Shur *et al.*, 2012; Young *et al.*, 2005). Numerical modelling based on Computational Fluid Dynamics (CFD) has also been employed to explore the influence of air flow (patients' inspiratory manoeuvre) and the design of the device, such as the grid structure, the mouthpiece geometry, the mouthpiece length and the size of the air inlet (Coates *et al.*, 2005a; Coates *et al.*, 2006; Coates *et al.*, 2004; Coates *et al.*, 2007).

However, experimental and CFD studies cannot provide the micro-scale information of particle-particle interactions, which is pivotal for understanding the underlying mechanism of DPIs. Therefore, as a useful method to simulate the behaviour of an assembly of particles, the discrete element method (DEM) has also been employed to explore the de-agglomeration and dispersion process of loose agglomerates in DPIs (Calvert *et al.*, 2009; Calvert *et al.*, 2011; Tong *et al.*, 2011; Tong *et al.*, 2010). Most of the DEM research was focused on loose (drug-

only) agglomerates and not much work on carrier-based agglomerates could be found.

This study develops a coupled DEM-CFD model to investigate the micro-mechanics in carrier-based DPIs. The processes of API particles attaching to and dispersing from the carrier particles are modelled respectively and the effects of van der Walls forces, electrostatic force, air flow and particle-wall impact are explored.

1.2 Objectives

This study aims to investigate the micromechanics in carrier-based DPIs using DEM-CFD. The objectives are summarised as follows:

a) Explore the effect of van der Waals forces on the attaching process of API particles to a carrier particle;
b) Explore the effect of electrostatic forces on the attaching process of API particles to a carrier particle;
c) Explore the effect of air flow on the dispersion process of API particles from a carrier particle;
d) Explore the effect of particle-wall impact on the dispersion process of API particles from a carrier particle.

1.3 Layout of this thesis

Chapter 1 presents an introduction to the background, objectives and layout of this thesis.

Chapter 2 reviews the current research on DPIs, including experimental and numerical work. The development of DEM is also summarised in this chapter.

Chapter 3 investigates the effects of van der Waals forces on the attachment process of API particles to a carrier particle. Firstly a critical velocity criterion is proposed to determine the lowest impact velocity at which two elastic auto-adhesive spherical particles will rebound from each other during impact. Then the attachment process of API particles to a large carrier in a vibrating container is investigated and a mechanism is proposed to describe this process.

Chapter 4 discusses the effects of electrostatic forces on the attachment process of API particles to a carrier particle. The mixing process of pre-charged carrier and API particles in a vibrating container is investigated and the influences of charge on particle and size of the container on the mixing performance are explored. A mechanism is proposed to describe this mixing process governed by a long range adhesive force, and it is compared with the mechanism for the mixing process governed by a short range adhesive force described in Chapter 3.

Chapter 5 investigates the effect of air flow on the dispersion process of API particles from a carrier particle using a coupled DEM-CFD method. A carrier-based agglomerate is initially formed and then dispersed in a uniformed air flow. The influences of the air velocity and work of adhesion are examined. The preferred location for API particles to detach is also explored. Furthermore, a mechanism is proposed to describe the air flow induced dispersion performance.

Chapter 6 investigates the effect of particle-wall impact on the dispersion process of API particles dispersing from a carrier particle. A carrier-based agglomerate is set to impact with a wall at various impact velocities and angles. The influence of impact energy and adhesion energy are examined. Moreover, a mechanism is proposed to describe the impact induced dispersion performance.

Chapter 7 summarises the findings and the limitations of this study, and proposes the possible future work.

According to the regulations of University of Birmingham, the format of Publication-style Chapter is used for Chapter 3 to 6. Although all the seven chapters in this thesis have a logical sequence, each result chapter (i.e. Chapter 3 to 6) is self-contained and has been published as a journal paper. Therefore, the introduction and DEM model parts in Chapter 3 to 6 may have some overlaps with each other or with those in Chapter 1 and Chapter 2.

CHAPTER 2: LITERATURE REVIEW

*Part of the content in this chapter was published as “Yang, J., Wu, C.Y., Adams, M. Numerical modelling of agglomeration and deagglomeration in dry powder inhalers: A review. *Current Pharmaceutical Design*, 2015.

2.1. Dry powder inhalers

2.1.1. Background and development

Dry powder inhalers (DPIs) have been developed to deliver medicines directly to the lungs and airways in the form of dry powders for treating pulmonary and respiratory diseases, such as asthma, bronchitis and emphysema. Using DPIs, a drug can be directly delivered to its site of action and act rapidly, resulting in a few advantages compared with other drug delivery approaches (e.g. injection and oral administration), such as direct delivery of drugs to the target areas resulting in a rapid onset of activity and smaller doses; providing more drug choices especially for those poorly absorbed orally; and its environmentally friendly label (Aulton and Taylor, 2001; Frijlink and De Boer, 2004; Islam and Gladki, 2008; Newman and Busse, 2002).

Drug particles are usually micronized to obtain a suitable size for use in DPIs (preferably less than 5 μm). However, due to their size range, the particles are extremely cohesive and thus have poor flowability. To overcome this behaviour, the drug particles are generally mixed with large carrier particles (usually 30 – 70 μm). The attraction between the drug and carrier particles is mainly due to van der Waals forces, Coulombic forces and capillary forces, in which van der Waals forces are the most dominant. The adhesive forces have to be sufficiently strong to transport the particles, but weak enough to be overcome by the removal forces generated during the de-agglomerate process.

A dry powder inhaler normally consists of four primary parts as shown in Fig. 2.1, including a powder formulation element, a dose system, a powder de-agglomeration part and the mouthpiece (Frijlink and De Boer, 2004). Drug particles and other excipients are pre-mixed and stored in the formulation element, gauged by the measuring part to produce the required amount of formulation, then delivered to the de-agglomerate system where they are broken into fine particles and finally inhaled with the inspiratory air flow to the targeted area through the mouthpiece.

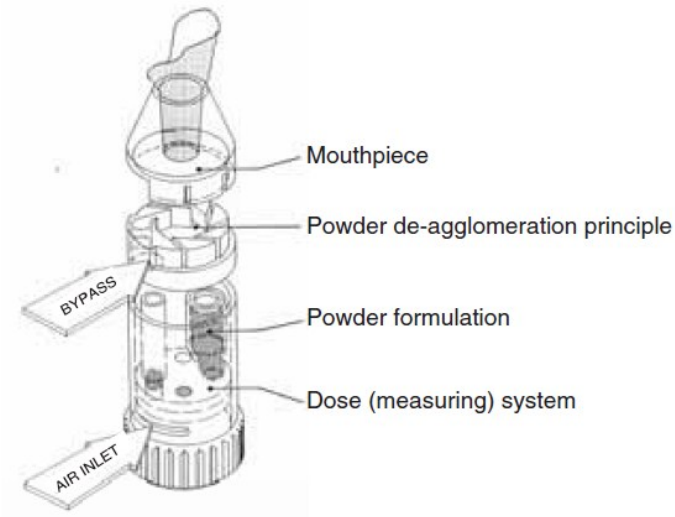

Fig. 2.1. Primary parts of a dry powder inhaler (Frijlink and De Boer, 2004).

In the dose measuring part, orifices in a disk or cavities in a slide are filled with powder from the powder formulation part where the formulated powders are stored. In some cases the filling relies on gravity action and, in other cases, on other forces such as those generated using compressed air.

In the powder de-agglomerate process, the drug particles should ideally detach from the surface of the carrier, so that they can reach the targeted action area. Depending on the powder de-agglomerate mechanism, the powder de-agglomerate systems can be classified into breath operated systems and auxiliary energy operated systems. The former uses kinetic energy of the inspiratory air flow to break up the mixture while the latter uses other means such as compressed air.

The mouthpiece can also be used for several functional purposes. In addition to controlling the resistance to air flow with bypass channels and reducing the deposition of the drug in the mouth from back flows, mouthpiece design is also relevant to the shape of the released aerosol cloud (Frijlink and De Boer, 2004).

The more recent DPI shown in Fig. 2.1 provides a multi-dose choice and is more convenient to patients. However, the single dose DPI is also applicable to the current market. The typical DPI using this mechanism is the first generation of DPI devices, i.e. Spinhaler® as shown in Fig. 2.2 (Aulton and Taylor, 2001). Capsules or blisters containing unit dose of inhalation powders are preloaded into the dose system, then different piercing or opening mechanisms are applied to break the capsules or blisters to disperse the powder into the inspiratory air stream. This kind of inhaler is single dose but more easy to operate.

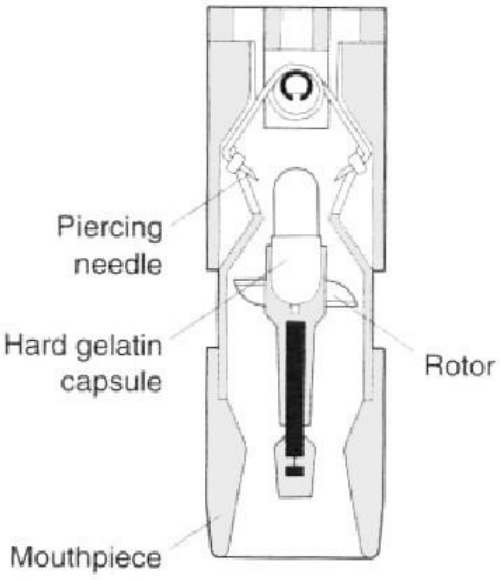

Fig. 2.2. The Spinhaler® (Aulton and Taylor, 2001).

DPIs have been developed for decades and currently there are many brands of DPIs available in current market. Normally, it is recognized that there are three main governing factors (i.e. Formulation design, Inhaler device design and Patients' respiratory manoeuvre) and two main dispersion mechanisms (i.e. air flow induced and mechanical impact induced) for DPIs, which are reviewed in details in the following sections.

2.1.2. Three main governing factors

It is widely acknowledged that there are three main factors governing the performance of DPIs, including the formulation design, the device design and the inspiratory manoeuvre of the patients. The effects of these three factors are reviewed respectively. However, it should be noted that the three factors actually affect the DPI performance in a collective manner and they also make influence

on each other. For example, a specific formulation (e.g. particle rugosity) with a specifically designed DPI device (e.g. the geometry of the mouthpiece) could enhance the DPI performance for a specific group of patients (e.g. sufficient inspiratory capacity) but it may reduce the lung deposition with another device or for other patients.

1) Formulation design

Since the optimal size distribution of drug particles for an inhaled medication is considered to be 1-5 μm, such small particles are very cohesive and not free flowing. It can cause drug retention within the device and reduce the amount of drug particles delivered by the inhaler. The uniformity in metering individual doses can also be reduced. Therefore, drugs delivered by an inhaler are formulated either by pure drug particles or with inactive excipient particles (i.e. drug-only formulation and carrier-based formulation) to form large agglomerates (Newman and Busse, 2002). The use of large agglomerates can help to increase the delivery dose and improve the dose uniformity as larger particles flow more easily and meter accurately. The budesonide agglomerate used in Turbuhaler® (made by AstraZeneca) is an example of drug-only formulation. The lactose-salbutamol blends used in Rotahaler® (made by GlaxoSmithKline) is an example of carrier-based formulations. Normally the inactive excipient particles are much larger than drug particles (i.e. active pharmaceutical ingredient (API) particles), with a diameter range of 30-120 μm; more recent researches also show that the addition of fine excipient particles may also be a promising approach to improve

the DPI efficiency (Jones and Price, 2006; Zeng *et al.*, 1999). Jones and Price (2006) showed that the addition of fine excipient particles during the mixing process increased the pulmonary delivery of the drug and there was an optimal concentration of added excipients. Zeng *et al.* (1999) used a twin stage impinger to investigate the effect of different sequences of addition on *in vitro* deposition. They found that the formulation prepared by first blending micronized lactose with coarse lactose before mixing with salbutamol sulphate produced a greater fine particle fraction (FPF) and fine particle dose (FPD) of salbutamol sulphate than the same formulation prepared using a different mixing order of the three components. “Active sites” occupied by either excipients or drugs was believed to have a considerable effect on the formulation dispersion performance.

There are three different formulation types: adhesive mixtures, nucleus agglomerates and spherical pellets as shown in Fig. 2.3. In adhesive mixtures (carrier-based formulation), drug particles are homogeneously distributed on the surface of the carrier particle due to the van der Waals adhesion. When the drugs are attached in multi-particulate layers around the carrier particle, nucleus agglomerates are formed. Spherical pellets are formed of pure micronized drug or mixtures of micronized drug and micronized excipient particles, resulting high porosity and low mechanical stability (Frijlink and De Boer, 2004).

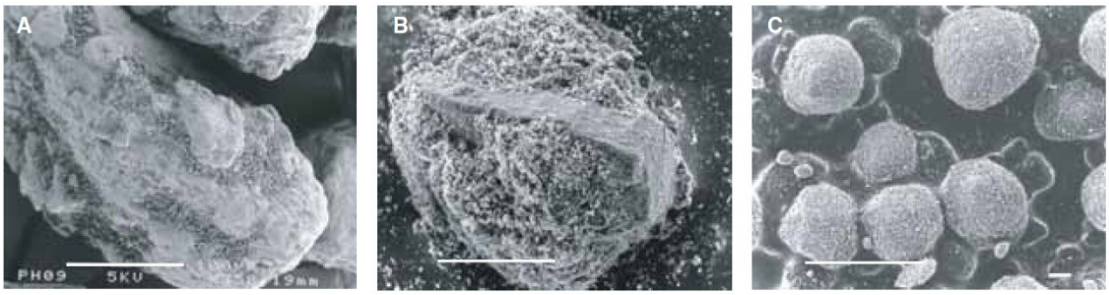

Fig. 2.3. SEM pictures of three types of formulation: a) an adhesive mixture, b) a nucleus agglomerate and c) a spherical pellet (Frijlink and De Boer, 2004).

The interactions between drug particles and carrier particles or drug particles and drug particles are critical for the DPI performance and have attracted a lot of research. The effective forces have to be sufficiently strong so that fine API particles can adhere with the carriers or form large agglomerates for storage or to be transported, but weak enough so that they can be detached or dispersed by a de-agglomeration process and thus allow the delivery of the API particles into the respiratory tracts and lungs. Therefore an ideal formulation should provide good homogeneity, stability and dispersion ability. Variables, such as particle size (Guenette *et al.*, 2009; Kaialy *et al.*, 2012a), particle shape (Kaialy *et al.*, 2011; Kaialy *et al.*, 2012b), density and porosity (Kaialy *et al.*, 2011; Kaialy and Nokhodchi, 2012), particle surface roughness (Kaialy *et al.*, 2012c; Young *et al.*, 2008), electrostatic charge (Adi *et al.*, 2010; Kaialy *et al.*, 2014; Pu *et al.*, 2009), surface energy (Cline and Dalby, 2002; Kaialy and Nokhodchi, 2012), crystal form (Shur *et al.*, 2012), storage conditions (Jashnani *et al.*, 1995; Le *et al.*, 2012), particle concentration (Steckel and Muller, 1997; Young *et al.*, 2005), material properties (Hassan and Lau, 2010; Steckel and Bolzen, 2004), flowability (Rabbani and Seville, 2005) and the type of ternary additives (Kaialy and Nokhodchi, 2013), have been investigated.

The influence of the particle size of a lactose carrier on the DPI performance was experimentally examined by Kaialy *et al.* (2012a). They demonstrated that the DPI performance improved with decreasing carrier particle size due to a decreasing adhesion. A study of the effect of carrier particle size (Guenette *et al.*, 2009) also showed that, while increasing the amount of fine lactose particles improved the DPI aerosolisation performance. It also led to increasing capillary forces and a poor storage stability. Therefore, the beneficial effect of finer carriers must be balanced with their negative effects.

Particle shape is also an important factor that affects the DPI performance. The dispersion performance of salbutamol sulphate from DPI formulations containing different carrier particles with different elongation ratio (ER) that is to characterise the particle shape was investigated by Kaialy *et al.* (2011). It was found that carrier particles with higher ER have smaller density, higher porosity and poor flow properties. Hence using carrier particles with higher ER can enhance the DPI performance by delivering more drug particles to lower airways. However, other limitations, such as higher drug retention in inhaler device, more deposition on throat and lower drug emission, also existed. Particle shape could also affect the electrification process, and sequentially influence the particle interactions and the formulation dispersion performance.

For the influence of particle density and porosity, Kaialy and Nokhodchi (2012) suggested that engineered lactose with smaller bulk and tap density and higher

porosity improved the homogeneity of drug content and the dry powder inhaler performance.

Recently, various techniques were employed to modify the surface roughness and adhesion of particles in order to optimise DPI performance. Adi *et al.* (2013) used spray drying to prepare the API particle with different surface roughness and used atomic force microscopy to measure the surface roughness and adhesion force properties. Significantly better de-agglomeration was found in corrugated particles than in smooth particles, which was attributed to the lower adhesion forces between corrugated particles. Kaialy *et al.* (2012c) also found that lactose particles with a rougher surface, an elongated shape and more irregular shapes could deliver more API particles to lower airway regions.

Previous experimental results showed that blending of positively charged carrier particles and negatively charged API particles can improve their uniformity because it strengthened the inter-particle adhesion (Pu *et al.*, 2009). However, Adi *et al.* (2010) initially charged mannitol powder to varying magnitudes by tumbling inside containers of different materials and then examined the dispersion performance. They found that the initial charge from tumbling did not significantly affect the aerosolisation.

The surface energies of drug and carrier particles of dry powder inhaler formulations were measured by Cline and Dalby (2002) using inverse gas chromatography (IGC) in two commercial DPIs. However, it was found that the

FPF increased with the increased surface energy. It was inconsistent with the intuition, and the authors argued that a minimum surface energy interaction between carrier and drug particles was needed to pull cohesive drug particles apart during the blending and dispersion processes, otherwise drug particles would keep aggregated. However, the mechanism behind this phenomenon was still unknown.

Seed crystals and supercritical carbon dioxide crystallization was used by (Shur *et al.* (2012) to produce ipratropium bromide monohydrate and anhydrous crystals, respectively, and they found that these two crystals exhibited similar mechanical and interfacial properties, which also resulted in the similar DPI performance.

The dispersion performance at various humidity conditions was examined by (Le *et al.* (2012) using a twin stage impinge. Results showed that the FPF decreased as the relative humidity is increased.

The relationship between API dosage (drug/lactose ratio) and aerosolisation performance of carrier based formulations was investigated by Young *et al.* (2005) using a twin stage impinge. It was found that the FPF decreased with increasing API dosage when the API dosage was low (10-135 μg/50 mg), while the FPF increased with increasing API dosage at large API dosages (135-450 μg/50 mg). These results were attributed to the effect of "active sites", which were preferentially occupied by API particles due to large contact area, high

surface energy and simple geometric constrains. Therefore, there was a critical API dosage below which the FPF decreased since API particles were adhered to the active sites, and above which FPF increased since the active sites were fully occupied with excessive API particles present in the formulation.

Particles of different materials have different properties, which can make considerable influence on DPI formulation performance. The potential use of a variety of alternative carriers in DPI formulations rather than lactose, such as mannitol, glucose, sorbitol, maltitol and xylitol, was evaluated by (Steckel and Bolzen (2004). It was found that different sources and qualities of carriers led to considerable differences in the FPF. Mannitol was found as a potential candidate as the alternative carrier whereas the more hygroscopic sugars presented poor dispersibility.

2) Inhaler device design

Besides the dedication to the study and development of DPI formulation, considerable attention has been focussed on device design. The design of a DPI device must be coordinated with the formulation design (Newman and Busse, 2002). The inhaler design is directly related to the air flow generated in the device, which is critical for lifting and delivering drug particles to lungs and lower airways. In addition, the materials of the DPI device affect the accumulation of electrostatic charge, which can change the amount of the drug remained in the inhaler as well as dispersion behaviour (Carter *et al.*, 1998). An increase of fine

particle dose of DPI was also reported by Heng *et al.* (2013) through coating the drug capsule and inhaler device to reduce drug retention in inhaler device. Therefore, the effect of device design was widely investigated and the influence of changes on mouthpiece, grid, and inlet are summarized as below.

Coates *et al.* (2004) used CFD and relevant experiment to explore how the modifications to an inhaler (Aerolizer®), including changing the grid voidage (Fig. 2.4) and the length of mouthpiece, influenced the DPI performance, which was measured with a mannitol powder using a multi-stage liquid impinger at 60 l/min. It was found that the amount of particles remained in the device doubled and the FPF reduced as the grid voidage increased while the length of the mouthpiece had little impact on the DPI performance.

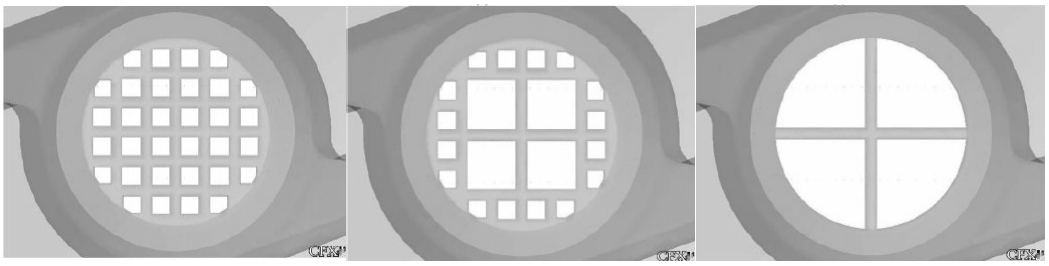

a) b) c)

Fig. 2.4. Schematic of the grid structures. a) original grid; b) modified grid 1; c) modified grid 2 (Coates *et al.*, 2004).

An investigation of the effect of the air inlet size (Fig. 2.5) on the air flow in the inhaler and the DPI performance was carried out by Coates *et al.* (2006). It was found that at low flow rates (30 and 45 l/min), reducing the air inlet size increased the inhaler dispersion performance due to increasing flow turbulence

and particle impaction velocities above their critical levels for maximal powder dispersion, while at 60 l/min, reducing the air inlet size reduced the inhaler dispersion performance resulted from releasing a large amount of powder from the device before the turbulence levels and particle impaction velocities could be fully developed.

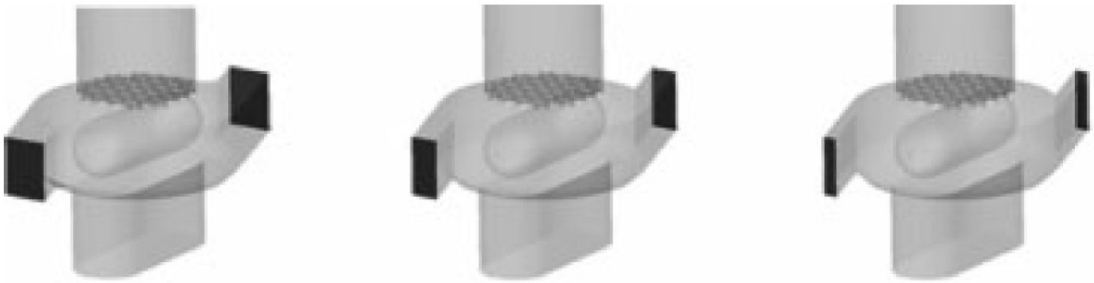

a) b) c)

Fig. 2.5. Schematic of the inlet size. a) full size; b) 2/3 size; c) 1/3 size (Coates *et al.*, 2006).

Coates *et al.* (2007) also examined the influence of mouthpiece geometry (including cylindrical, conical and oval designs) on the device retention, throat deposition and the overall inhaler performance. It was found that the mouthpiece geometry had no effect on device retention and the overall DPI performance while it significantly affected the throat deposition by controlling the axial component of the exit air flow velocity.

The effect of the spinning capsule on the overall performance of DPI inhaler Aerolizer® was explored by Coates *et al.* (2005b) through visualizing the capsule motion using high-speed photography. CFD was also applied to determine the air flow in the inhaler with and without the presence of different sized capsules. It

was found that the capsule size had no effect on the device flow field, particle-device impaction frequency and the DPI dispersion performance. However, the presence of the capsules actually had a considerable influence on the dispersion behaviour due to providing additional strong mechanisms for formulation de-agglomeration.

3) Patients' respiratory manoeuvre

The patients' respiratory manoeuvre, in conjunction with the resistance of a DPI, determines the air flow through the inhaler (Newman and Busse, 2002). The peak inspiratory flow rate (PIFR) affects the process of lifting particles of the drug formulation from the drug chamber or capsule and the process of de-agglomeration (Newman *et al.*, 1989; Vidgren *et al.*, 1988). Therefore, patients are advised to inhale with full inspiratory effort in order to optimize drug delivery. Less inspiratory effort will lead to a lower PIFR through the device, a lower amount of particles omitted from the device and deposited in the lungs (Clark, 1995). On the other hand, DPIs with high-resistance reduces the inter-patient variability in PIFR compared to low-resistance devices, resulting in more reproducible inhaler performance (Pauwels *et al.*, 1997). In conclusion, the patients' respiratory manoeuvre mainly determines the air flow in the inhaler device, which is widely considered as one of the most important dispersion mechanisms for the dispersion process in DPIs.

An ideal inhaler should diminish the influence of patients' respiratory manoeuvre, i.e. reproducible flow rate. However, for current DPIs in the market, their performances are actually affected by the PIFR generated through the device. In addition, the rate of increase in flow, or "rise time" to peak air flow rate, also plays an important role in controlling the performance (Everard *et al.*, 1997). The inspiratory flow rate, rise time (defined by the time between 10 and 30 l/min), and duration of inhalation of adults with mild-to-moderate and severe asthma are compared in Fig. 2.6. Two group of patients produced similar mean PIFRs and rise times but the inhalation durations of the mild-to-moderate patients were longer (Newman and Busse, 2002). This indicated that most patients were able to generate the required air flow to operate the DPI. However, the effects of their unique inspiratory manoeuvre cannot be ignored.

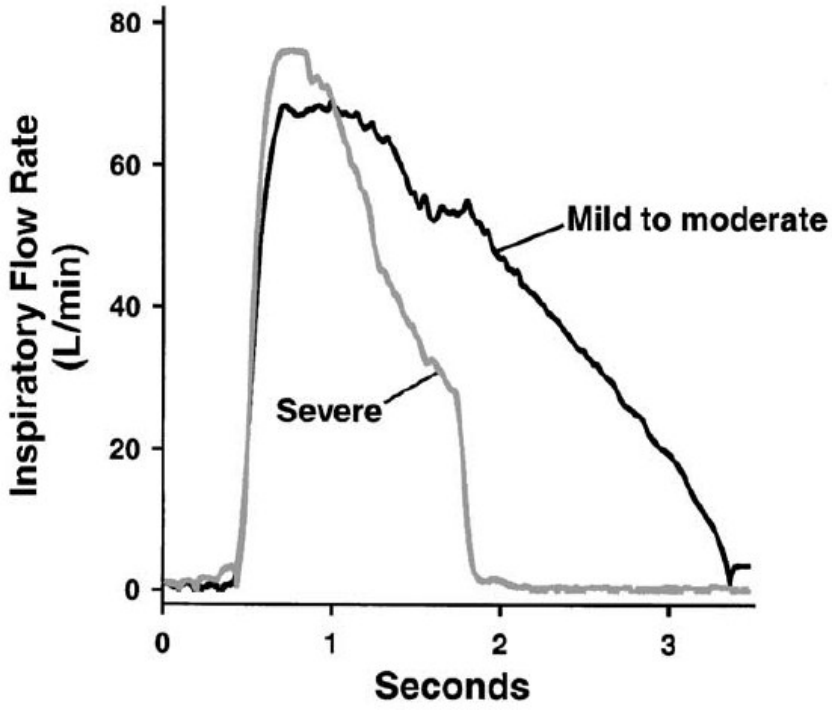

Fig. 2.6. Examples of inspiratory flow rates produced by adults with mild-to-moderate persistent asthma and severe asthma (Newman and Busse, 2002).

2.1.3. Dispersion mechanisms

It is well recognized that the dispersion process in DPIs is primarily governed by two mechanisms: i) air flow and ii) mechanical impact (De Boer *et al.*, 2003; Donovan *et al.*, 2012; Voss and Finlay, 2002). However, inconsistent results still exist. For example, it was reported that air flow can dominate the dispersion performance while particle-particle and particle-wall impacts were also found to play an important role in dispersion process of DPIs. In fact, the DPI performance is governed by so many variables as described in Fig. 2.7, also as we summarised in the previous sections, that the current research results are based on some specific conditions and assumptions and the results or arguments can only be valid under the specific conditions. It is believed that both the air flow and the impact play an important role on the dispersion process in DPIs. Therefore, in this section, the effects of the two main mechanisms are discussed.

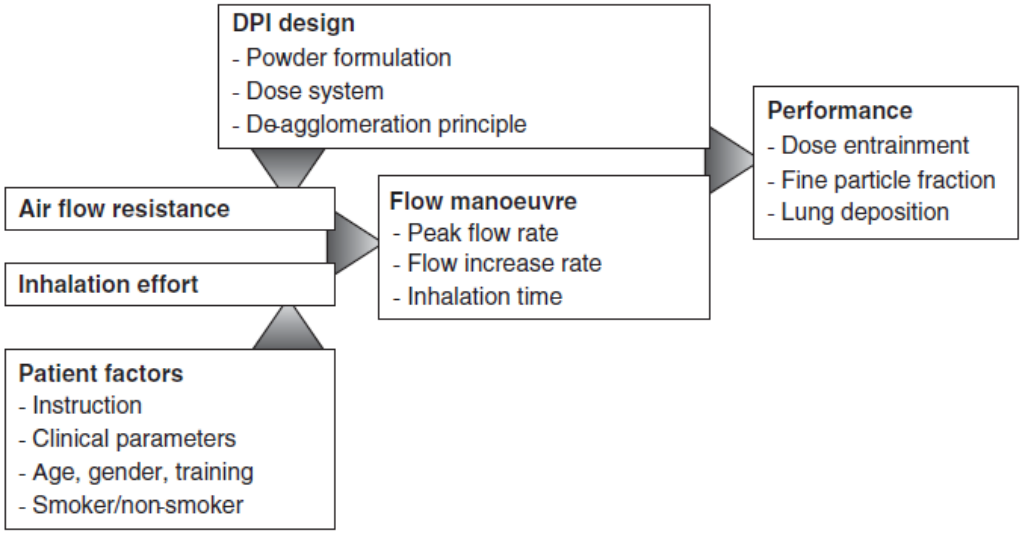

Fig. 2.7. Scheme of the major variables and interactions in DPI performance (Frijlink and De Boer, 2004).

Voss and Finlay (2002) developed a powder de-agglomeration device, which was designed to entrain a dose of powder into the air stream and expose the powder to either a controllable level of turbulence or a mesh; the aim was to explore the effects of turbulence and mechanical impaction on dry powder de-aggregation. They found that the extent of de-aggregation increased as the level of turbulence was increased.

The rate at which API particles are detached from carrier particles in adhesive mixtures in an air classifier was investigated by De Boer *et al.* (2004). They found that the rate increased with increasing flow rate and the dispersion time.

Aerodynamic dispersion of loose aggregates in a uniform fluid flow was investigated using DEM-CFD by Calvert *et al.* (2011). They found that there was a threshold velocity above which dispersion occurred quickly and approached equilibrium asymptotically.

On the other hand, impact induced dispersion/de-agglomeration also drew much attention of researchers.

The impact of a cuboidal agglomerate with a wall was investigated by (Thornton and Liu (2004). It was found that the fracture occurred as a result of strong force transmission into the agglomerate creating a heterogeneous velocity distribution.

Ning *et al.* (1997a) simulated the agglomerate-wall impact induced breakage of a lactose agglomerate that consisted of 2000 primary particles within a size range of 9-11 μm. They found that the dynamic features and loading compliance of loose agglomerates were distinctly different from solid particles and strongly bonded agglomerates.

Recently, the impact between a loose agglomerate of fine mannitol particles and a wall was modelled using the discrete element method (DEM) by Tong *et al.* (2009). They found that agglomerate breakage was promoted with increasing impact velocity and an optimal breakage performance was obtained at an impact angle of 45°.

Although the influence of turbulence on the break-up and aerosol performance of DPI formulations was investigated by Wong *et al.* (2010) using a combination of computational fluid dynamics and standardized entrainment tubes, they argued that there was no correlation between the extent of the turbulence and aerosol performance and the impact dominated agglomerate break-up in the system considered. The influence of impact on DPI performance was further examined by Wong *et al.* (2011), who found that particle-wall impacts resulted in initial agglomerate fragmentation followed by re-entrainment in the airstream.

Tong *et al.* (2010) performed a combined CFD and DEM approach and investigated powder dispersion. In their study, agglomerates of different particle sizes and poly-dispersities were dispersed in a cyclonic flow at different flow

velocities. It was shown that the dispersion was governed by particle-wall impacts and particle-particle adhesion.

These studies provided a better understanding of the underlying mechanisms of air flow induced and impact induced dispersion/de-agglomeration. However, they were generally concerning the overall behaviour of the DPIs and the mechanical analysis of dispersion behaviour of loose agglomerate (i.e. drug-only formulations). The investigation for carrier-based DPIs at the micro-mechanical level was rarely reported. In addition, it should be noted that these two main dispersion mechanisms need to be discussed under specific conditions and they determine the overall DPI performance collectively.

2.2. DEM and its applications in DPIs

2.2.1. The theory and development of DEM

The discrete element method (DEM) was first proposed by Cundall and Strack (1979) and then developed in the last few decades for modelling the behaviour of an assembly of particles. Owing to its distinguished advantages of providing the detailed information of the particulate system at single particle level, such as the trajectory of and the transient force acting on the particle, which is difficult to obtain in conventional experiments, and providing a relationship between the macroscopic and microscopic properties of particulate matter, which is truly

demanded for current particle and science research, DEM has been widely used in many fields, such as chemical engineering, pharmaceutical engineering, environmental engineering, energy engineering and food industry (Zhu *et al.*, 2007).

There are two common DEM models. While the simple hard-sphere model, which cannot explicitly calculate the interaction forces between particles and treat the impacts as instantaneous ones, is typically used for rapid granular flows, the soft-sphere model is more popular. In the soft-sphere model, the particles are able to suffer deformations which are used to calculate the interactional forces between particles though the force-displacement relationship. In addition, the soft-sphere model is capable of handling multiple particle contacts.

With the contact force and other kinds of forces, the motion of every single particle in the system is determined by Newton's second law, including translational and rotational movement, as bellows:

$$m_i \frac{\mathrm{d}\mathbf{v}_i}{\mathrm{d}t} = \mathbf{f}_{ci} + \mathbf{f}_{nci} + \mathbf{f}_{fpi} + m_i \mathbf{g} \tag{2.1}$$

$$I_i \frac{\mathrm{d}\boldsymbol{\omega}_i}{\mathrm{d}t} = \mathbf{T}_i \tag{2.2}$$

where m_i , I_i , $\mathbf{v}_i$, $\boldsymbol{\omega}_i$ are the mass, moment of inertia, translational and rotational velocities of particle i, respectively. $\mathbf{f}_{ci}$, $\mathbf{f}_{nci}$, $\mathbf{f}_{fpi}$, and $\mathbf{T}_i$ are the contact force, non-contact force, particle-fluid interaction force and torque acting on the

particle. $\mathbf{g}$ is the gravitational acceleration. Typical forces and torques are shown in Fig. 2.8. For particle i in that figure, the contact force is the force caused by the impact with particle j, which can be devided into the normal component and the tangential component. The non-contact force is the capillary force caused by the liquid bridge between particle i and k.

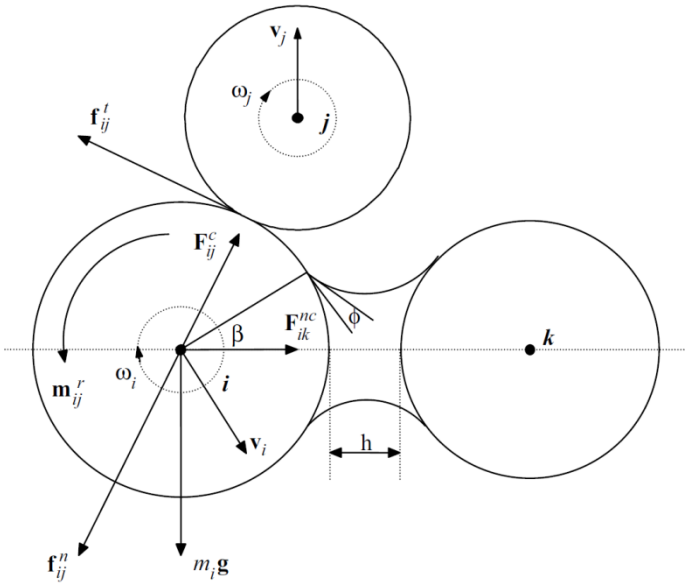

Fig. 2.8. Forces and torques acting on particle *i* from particle *j* and *k* (Zhu *et al.*, 2007).

2.2.1.1 Forces calculation

1) Elastic contact force

Accurate calculation of forces acting on particles is important for DEM. A number of models have been proposed to calculate these forces and torques. The contact force can be decomposed into two components, the normal direction that

is perpendicular to the contact plane and the tangential one that is parallel to the contact plane. The most common and simplest model to calculate these two forces is the linear spring-damping model, in which the spring and damping are used for the elastic deformation and viscous dissipation, respectively (Cundall and Strack, 1979):

$$\mathbf{f}_{cn} = -k_n \boldsymbol{\delta}_n - C_n \mathbf{v}_n \tag{2.3}$$

$$\mathbf{f}_{ct} = -k_t \boldsymbol{\delta}_t - C_t \mathbf{v}_t \tag{2.4}$$

where $\boldsymbol{\delta}$ and $\mathbf{v}$ are the displacement and relative velocity between particles, respectively; n and t denote the normal and tangential direction, respectively.

Based on contact mechanics, Hertz (1882) proposed a more complex nonlinear model, normally known as Hertzian model, to calculate the contact force in the normal direction as:

$$F_{cn} = \frac{4}{3} E^* R^{*1/2} \alpha^{3/2} \tag{2.5}$$

where F_{cn} and α are the magnitude of the normal contact force and overlap, respectively. E^* and R^* are the effective Young's modulus and radius, which are defined as:

$$\frac{1}{E^*} = \frac{1-\nu_1^{\,2}}{E_1} + \frac{1-\nu_2^{\,2}}{E_2} \tag{2.6}$$

$$R^* = \frac{R_1 R_2}{R_1 + R_2} \tag{2.7}$$

where E_i, R_i ,and υ_i are the Young's modulus, radius, and Poisson's ratio of the particles i. With Hertzian model, the radius of the contact area a is given as:

$$a = \sqrt{\alpha R^*} \tag{2.8}$$

Mindlin and Deresiewicz (1953) proposed a model for the calculation of contact force in the tangential direction, in which the incremental tangential force ΔF_{ct} arising from the incremental tangential displacement $\Delta\delta_t$ depends on the incremental normal force ΔF_{cn} and the loading history:

$$\Delta F_{ct} = 8G^* a\theta_k \Delta\delta_t + (-1)^k \mu \Delta F_{cn}(1-\theta_k) \tag{2.9}$$

where μ is the coefficient and friction and G^* is the effective shear modulus defined as:

$$\frac{1}{G^*} = \frac{2-\nu_1}{G_1} + \frac{2-\nu_2}{G_2} \tag{2.10}$$

in which G_i is the shear modulus of particle i.

There is a no-slip solution that:

$$\theta_k = 1 \text{ when } \left|\Delta F_{ct}\right| < \mu \Delta F_{cn} \tag{2.11}$$

Otherwise partial-slip solution that:

$$\theta_k = \sqrt[3]{1 - \frac{F_{ct} + \mu \Delta F_{cn}}{\mu F_{cn}}} \text{ when } k = 0 \tag{2.12}$$

$$\theta_k = \sqrt[3]{1 - \frac{(-1)^k (F_{ct} - F_{ct}^{\ c}) + 2\mu \Delta F_{cn}}{2\mu F_{cn}}} \text{ when } k = 1,2 \tag{2.13}$$

k=0, 1, 2 represent loading, unloading and reloading paths, respectively. $F_{ct}^{\ c}$ is the historic tangential force at which loading or reloading commenced.

2) Adhesive forces

When the sizes of particles are small, normally less than 100 μm, van der Waals forces are comparable with the weight of particles and cannot be ignored as shown in Fig. 2.9.

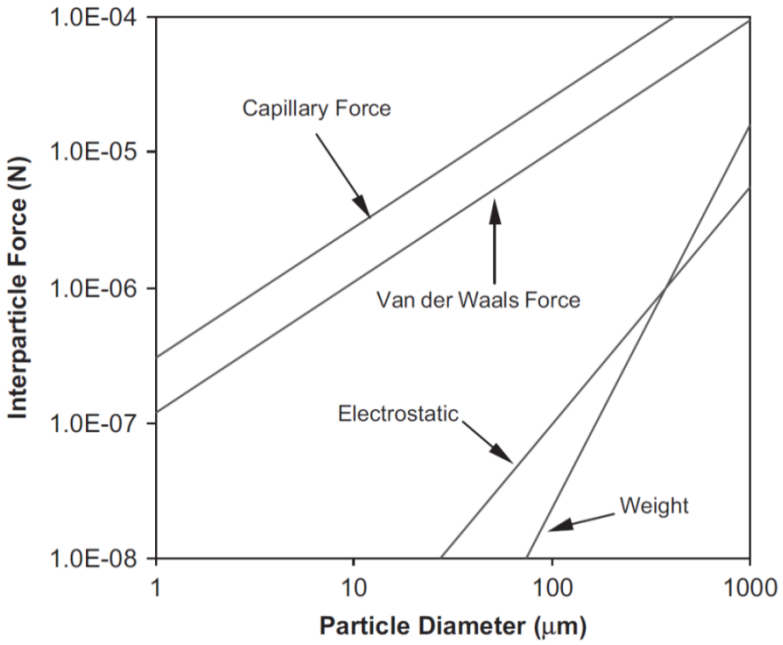

Fig. 2.9. Comparison of forces on particles (Zhu *et al.*, 2007a).

Based on Hertzian model, Johnson *et al.* (1971) proposed a model, namely JKR model, to take the surface energy into account and calculate the normal force for the so-called auto-adhesive particles. The radius of the contact area for the contact with adhesion is then defined as:

$$a = \left(\frac{3R^* F_{cn}'}{4E^*} \right)^{1/3} \tag{2.14}$$

Where F_{cn}' is the effective Hertzian force and defined as:

$$F_{cn}' = F_{cn} + 2F_C \pm \sqrt{4F_{cn}F_C + 4F_C{}^2} \tag{2.15}$$

in which F_{cn} is the applied force and F_C is the pull-off force:

$$F_C = \frac{3}{2}\pi\Gamma R^* \tag{2.16}$$

where Γ is the thermodynamic work of adhesion. The relative approach of the two contacting particles α is related to the contact area by:

$$\alpha = \frac{a^2}{R^*} - \sqrt{\frac{2\pi\Gamma a}{E^*}} \tag{2.17}$$

Besides JKR model, there is another common model proposed by (Derjaguin *et al.* (1975), namely DMT model, to calculate the adhesive normal force. The difference of these two models is that while there are two kinds of force in the contact area: the compressive force in the inner circular and the tensile force in the outer annulus that are infinite at the perimeter; the DMT model assumes that the compressive force acts in the contact area and the tensile force act out of the contact area and decreases with surface separation. Therefore, DMT model proposes a pull-off force $F_C = 2\pi\Gamma R^*$ other than Eq. (2.16) in JKR theory.

Thornton and Yin (1991) developed a model that combine the theory of Mindlin and Deresiewicz (1953), Savkoor and Briggs (1977), and JKR theory and implemented it into the DEM code. The JKR theory is adopted to calculate the incremental normal force ΔF_{cn} that is related to the incremental relative approach $\Delta\alpha$ in DEM as:

$$\Delta F_{cn} = 2E^* a \left(\frac{3\sqrt{F_{cn}'} - 3\sqrt{F_C}}{3\sqrt{F_{cn}'} - \sqrt{F_C}} \right) \Delta\alpha \tag{2.18}$$

For the calculation of tangential force, Thornton and Yin (1991) proposed that a peeling phenomenon occurs first, which causes a reduction of the contact area, and during this stage the tangential interactions are modeled using the no-slip solution of Mindlin and Deresiewicz (1953) as:

$$\Delta F_{ct} = 8G^* a \Delta\delta_t \tag{2.19}$$

with a updated contact area defined as:

$$a^3 = \frac{3R^*}{4E^*} \left(F_{cn} + 2F_C \pm \sqrt{4F_{cn}F_C + 4{F_C}^2 - \frac{{F_{ct}}^2 E^*}{4G^*}} \right) \tag{2.20}$$

The peeling process continues until a critical value of tangential force ${F_{ct}}^C$ is reached. ${F_{ct}}^C$ is defined as:

$${F_{ct}}^C = 4\sqrt{\frac{G^*}{E^*}\left(F_{cn}F_C + {F_C}^2\right)} \tag{2.21}$$

When the peeling process is complete, the contact area is reduced to:

$${a_p}^3 = \frac{3R^*}{4E^*}\left(F_{cn} + 2F_C\right) \tag{2.22}$$

There is a smooth transition from peeling to sliding when the peeling process is complete: 1) if the critical tangential force F_{ct}^{C} is smaller than the sliding force, a subsequent slip annulus is assumed to spread radially inwards. The partial-slip solution of Mindlin and Deresiewicz (1953), which is described in Eqs. (2-12) and (2-13), is used with F_{cn} replaced by $F_{cn}+2F_C$ until sliding occurs; 2) if the critical tangential force F_{ct}^{C} is larger than the sliding force, the tangential force fall to the sliding force immediately and post-peeling behavior is modeled by:

$$F_{ct}=\mu F_{cn}'\left(1-\frac{F_{cn}'-F_{cn}}{3F_{cn}'}\right)^{3/2} \quad \text{when } F_{cn}<-0.3F_C \tag{2.23}$$

$$F_{ct}=\mu\left(F_{cn}+2F_C\right) \quad \text{when } F_{cn}\geq -0.3F_C \tag{2.24}$$

The Hamaker theory (Hamaker, 1937) is also applied by some researchers in DEM to calculate the van der Waals force (Yang *et al.*, 2008; Zhu *et al.*, 2007a). The van der Waals force is determined by:

$$F_v=-\frac{Ad_p}{24h^2} \tag{2.25}$$

in which A is the Hamaker constant, d_p the particle diameter, and h is the separation between particles. Then the van der Waals force is directly added to the right-hand side of Eq. (2.1) as a single term, other than incorporating the concept surface energy, to take into account the adhesion.

Besides the van der Waals force, electrostatic force and capillary force also play important roles in particle adhesion as shown in Fig. 2.9. Pei *et al.* (2010) developed a model to consider the electrostatic force between particles $\mathbf{f}_{ei}$ in DEM. In this model, a cut-off distance is introduced to improve the computational efficiency and the electrostatic force is considered only when the distance between the particles is smaller than the cut-off distance; otherwise it is neglected. Coulomb's law (Seville *et al.*, 1997) is employed to model the electrostatic force between particles as follows:

$$\mathbf{f}_{21} = \frac{1}{4\pi\varepsilon_0\varepsilon_r}\frac{q_1 q_2}{r_{21}^{\ 2}}\hat{\mathbf{r}}_{21} \tag{2.26}$$

where $\mathbf{f}_{21}$ and $\hat{\mathbf{r}}_{21}$ are the electrostatic force and unit vector from particle 2 to 1, respectively. ε_0 and ε_r are the permittivity of free space and the relative permittivity of the medium in the vicinity of the particles. q_1 and q_2 are the charges on the two particles, and r_{21} is the distance between the two particles.

The capillary force is mainly resulted from the surface tension at gas/liquid/solid interfaces. The force due to the reduced hydrostatic pressure in the bridge itself as shown in Fig. 2.8 can be defined as (Fisher, 1926):

$$F_l = 2\pi\gamma R\sin\phi\sin(\phi+\theta) + \pi R^2\Delta p\sin^2\phi \tag{2.27}$$

where γ is the liquid surface tension, R is the particle radius, ϕ is the half-filling angle, and θ is the contact angle.

3) Particle-fluid interaction force

When the fluid is in presence, the fluid-particle interactions can make a considerable effect on the particle behaviour. Anderson and Jackson (1967a) proposed that the force exerted by the fluid on each particle can be written as:

$$\mathbf{f}_{fpi} = v_{pi}\nabla.\xi_f + \mathbf{f}'_{fpi} \tag{2.28}$$

where v_{pi} is the volume of particle i, ξ_f is the local average fluid stress tensor, and $\mathbf{f}'_{fpi}$ is the effective drag force in the direction of the relative velocity between fluid and particle.

According to the assumption of Anderson and Jackson (1967a), ξ_f and $\mathbf{f}'_{fpi}$ can be expressed as:

$$\xi_f = -p\boldsymbol{\delta} + \boldsymbol{\tau}_f \tag{2.29}$$

$$\mathrm{f}'_{fpi} = \varepsilon\mathbf{f}_{di} \tag{2.30}$$

where p is the fluid pressure, $\boldsymbol{\delta}$ is the identity tensor, $\boldsymbol{\tau}_f$ is the viscous stress tensor in the fluid, ε is the local void fraction, and $\mathbf{f}_{di}$ is the drag force obtained from the experimentally based correlations. Therefore, Eq. (2.28) is rewritten as:

$$\mathbf{f}_{fpi} = -v_{pi}\nabla.p + v_{pi}\nabla.\boldsymbol{\tau}_f + \varepsilon\mathbf{f}_{di} \tag{2.31}$$

The effect of fluid-particle interaction is considered by incorporating Eq. (2.31) to Eq. (2.1). According to Newton's third law, there is also a force acting to the fluid by the particle. The motion of fluid in computation fluid dynamics (CFD) is governed by the Navier-Stokes equation as:

$$\frac{\partial(\varepsilon\rho_f)}{\partial t} + \nabla.(\varepsilon\rho_f\mathbf{u}) = 0 \tag{2.32}$$

$$\frac{\partial(\varepsilon\rho_f\mathbf{u})}{\partial t} + \nabla.(\varepsilon\rho_f\mathbf{u}\mathbf{u}) = -\nabla.p + \nabla.\boldsymbol{\tau}_f - \mathbf{F}_{fp} + \varepsilon\rho_f\mathbf{g} \tag{2.33}$$

The particle-fluid interaction is considered for the fluid phase from the particle-fluid interaction force per unit volume $\mathbf{F}_{fp}$, which is defined as:

$$\mathbf{F}_{fp} = \frac{\sum_{i=1}^{n_c}\mathbf{f}_{fpi}}{\Delta V_c} \tag{2.34}$$

where n_c is the number of particles in a fluid cell of volume ΔV_c. The DEM and CFD are hence coupled in a two-way coupling scheme.

2.2.1.2 DEM capacity

In order to increase its capacity, DEM has been advanced in a number of aspects to enhance its application in many fields.

1) Irregular particles

Normally the shape of the particle in DEM is assumed spherical (or circular in 2D). This is for the convenience of contact detection and inter-particle force calculation. However, the shape of particles in reality is rarely spherical. In addition, the effect of particle shape on particle mechanical behaviour has been demonstrated by many researchers (Latham and Munjiza, 2004; Shinohara *et al.*, 2000).

Therefore, particles with irregular shape should be applied in DEM simulations if needed. This can be implemented by the so-called single-particle method or multi-sphere method.

The particle is a single object but the shape is as complicated as required, such as polyhedron (Latham and Munjiza, 2004), ellipsoid (Lin and Ng, 1997), and superquadric (Hogue, 1998) in the single-particle method. The algorithm for contact detection is based on the particle shape and therefore is much more computationally expensive. Moreover, the force-displacement relationship for

non-spherical particle is not fully developed as those for spherical particles (Hoehner *et al.*, 2011; Hogue, 1998).

In the multi-sphere method, the particle with irregular shape is consisted of a cluster of primary spheres (Favier *et al.*, 1999; Kodam *et al.*, 2009). The required shape can be approximated by arranging the position of primary spheres and the multi-sphere is treated as a rigid body. Although there is a difference between the shape of the constructed multi-sphere and the prescribed shape, other advantages of the multi-sphere method, such as same contact detection algorithm and contact force as those for spherical particles, make it popular in DEM applications (Hoehner *et al.*, 2011; Kodam *et al.*, 2009).

2) Coupling with other modelling tools

In addition to CFD-DEM, many other numerical methods with different time and length scales for fluid flow, such as Lattice-Boltzmann (LB) (Cook *et al.*, 2004), direct numerical simulation (DNS) (Hu, 1996; Pan *et al.*, 2002), large eddy simulation (LES) (Zhou *et al.*, 2004a; Zhou *et al.*, 2004b; Zhou *et al.*, 2004c), and pseudo-particle method (PPM) (Ge and Li, 2001; Ge and Li, 2003), were coupled/combined with DEM to describe the particle-fluid flow.

These coupling/combinations enable DEM to be used in a wider range of areas to setup more realistic models to provide insights into correlating the macroscopic particulate behaviour with microscopic inter-particle interactions.

These methods were not used in current study that focused on exploring the fundamental micromechanics, but they could be helpful for the further research.

2.2.2. The applications of DEM in DPIs

Interactions between particles or a particle and a wall play a significant role in controlling DPI performance. In addition to the improvement for computing power, the advantage of DEM over the conventional experimental approach and other modelling tools, such as providing the detailed information of particle behaviour including trajectory and transient force at single particle level, make DEM widely used in particle science and technology area, including the development and optimisation of DPIs. This section will review the applications of DEM in DPIs, including the mixing/agglomeration process and dispersion/de-agglomeration process.

Thornton *et al.* (1996) first used a two dimensional DEM to model the impact between an agglomerate and a wall. The agglomerate was formed by 1000 monodisperse primary particles with a radius of 100 μm and a surface energy up to 3.0 J/m^2. All primary particles were initially randomly generated within a prescribed region and then a centripetal gravity field was imposed to bring the particles together. Once the particles were satisfactorily packed together, the surface energy was applied in very small increments until the desired level was reached. Then the gravity field was gradually changed from the centripetal one to the normal vertical one until a dense agglomerate was formed, as shown in Fig.

2.10. Thereafter, the velocities of all primary particles were set to zero first and then specified as the desired impact velocity to make the agglomerate impact the wall. The authors proposed three regimes of behavior described as shattering, semi-brittle fracture and elastic rebound, which depended on the magnitudes of impact velocity and surface energy. This work first demonstrated the capability of DEM to model the agglomeration and de-agglomeration process by providing the consistent qualitative trends with experimental studies.

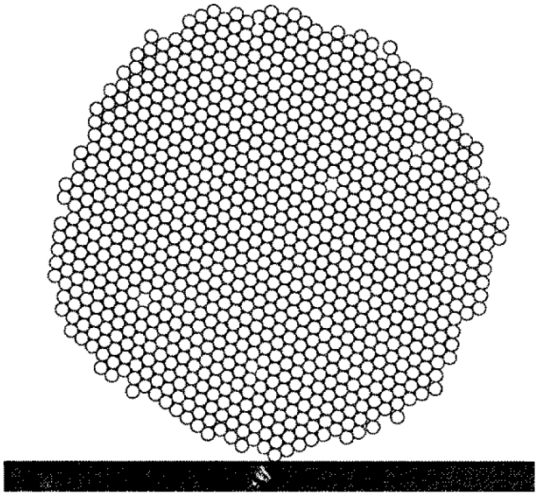

Fig. 2.10. A model agglomerate (Thornton *et al.*, 1996).

An improved 3D model with a dense spherical agglomerate constituting a random polydisperse system of autoadhesive particles impacting a wall was also proposed by Thornton *et al.* (1999). They found higher impact velocities lead to higher wall forces, local contact damage, number of broken bonds and amount of debris produced, and proposed two major processes, corresponding to the

loading and unloading stages, identified to contribute to the breakage. During the loading process, a conical ‘‘damage zone’’, in which most of the input energy was dissipated, was formed due to the plastic deformation caused by the impact. Several mechanisms in the zone were involved including irreversible deformation of the microstructure, interparticle sliding and randomly distributed microcrack formation. Meanwhile, other contacts were broken to form randomly distributed microcracks along sets of half-meridian planes. During the unloading process, while certain preconditioned half-meridian planes experienced further microcrack formation and coalescence, leading to subsequent fracture along these planes; the broken contacts along other half-meridian planes tended to close.

Following the above work, Kafui and Thornton (2000) performed another DEM investigation on the micromechanics of impact of a spherical crystalline (face-centred cubic) agglomerate with a target wall. It was reported that increasing impact velocity led to a higher maximum value of wall force, a shorter impact event and more broken bonds and increasing bond strength resulted in an increasing maximum value of wall force, reducing broken bonds. They argued that for any given bond strength there was a critical impact velocity producing a complete set of fracture planes. While impacts at low velocities only produced subsets of this fracture pattern, impacts with higher velocities did not produce extra fracture planes but weakened the residual fragments due to internal bond breakage and resulted in shattering. They also found that during the loading process, a set of potential fracture planes were formed by shear-induced weakening, whose pattern was dictated by the geometry of the interface and the

orientation of the agglomerate. During the unloading process, further shear-induced bond breakage occurred along the same set of planes.

The effects of impact velocity, solid fraction, contact density, and the local arrangement of particles near the impact zone on the breakage of agglomerates were further investigated by Mishra and Thornton (2001). It was found that fracture occurred for densely-packed agglomerate above a critical impact velocity whereas disintegration for loosely-packed one. For agglomerates with intermediate packing densities, the mode of failure can change from disintegration to fracture by either increasing the contact density or changing the location on the agglomerate surface that is used as the impact site. This emphasized the importance of the microstructure on the agglomerate breakage behaviour.

Thornton and Liu (2004) summarized that fracture was the result of the manner in which strong interparticle forces were transmitted into the agglomerate and the consequent development of a heterogeneous distribution of primary particle velocities. This heterogeneous velocity field produced strong velocity discontinuities along which shear weakening occurs. Consequently, the strong velocity discontinuities became the potential fracture planes.

Utilizing DEM to obtain the comprehensive information of particle positions, velocities and forces acting on them, Thornton's work provided an insight to the agglomerate breakage at microscopic level.

Ghadiri and co-workers applied DEM to carry out a series of studies on the breakage process of loose agglomerates. They first formed an agglomerate consisting 2000 primary particles representing large lactose crystals with polydisperse size (Ning *et al.*, 1997b). The agglomerate was loose since weak interface forces due to surface energy hold the primary particles together and no binder was used. It was proposed that the breakage performance was correlated to the square of impact velocity. It was found that loading compliance and dynamic feature of loose agglomerates differed significantly from those of solid particles and strong strength agglomerates. While at lower impact velocities, residual clusters remained, disintegration occurred at higher impact velocities. These findings were further validated with experimental results.

The influence of agglomerate size and humidity on loose agglomerate breakage and the mechanism of breakage were investigated (Boerefijn *et al.*, 1998). It was observed that smaller agglomerates were more likely to break. While agglomerates stored at low humidity levels exhibited internal shear and large overall deformation, with no appearance of a clear crack plane, those stored at high humidity levels experienced a classical semi-brittle failure mode.

Oblique impacts between an isotropic (mass distribution and coordination number) spherical agglomerate and a wall was examined by Moreno *et al.* (2003). It was found that the normal component of the impact velocity was dominant for the breakage performance. However, the breakage pattern was

affected by the tangential component of the impact velocity. This work elucidated the influence of impact angle on agglomerate breakage.

An model was proposed by Moreno-Atanasio and Ghadiri (2006), based on the assumption that the work required for breaking contacts was proportional to the incident kinetic energy, to predict the agglomerate breakage. The damage ratio D_R, defined as the ratio of broken contacts to the number of initial ones, was correlated to a dimensionless group as:

$$D_R \propto We I_e^{2/3} \tag{2.35}$$

where We is the Weber number and I_e is the elastic adhesion index:

$$We = \rho D V^2 / \Gamma \tag{2.36}$$

$$I_e = ED / \Gamma \tag{2.37}$$

where ρ is the particle density, D the particle diameter, V is the impact velocity, E the elastic modulus, and Γ the work of adhesion. Results of DEM simulations of four different agglomerates impacting with a wall for three different values of the work of adhesion showed the new model could describe the breakage behaviour better than the Weber number.

They also investigated air flow induced dispersion of loose agglomerates. The dispersion process of an agglomerate in a uniform fluid flow was modelled using CFD-DEM (Calvert *et al.*, 2011). It was found that increasing adhesion decreased the extent of breakage and there was a critical air velocity beyond which dispersion occurred quickly and asymptotically reached a stable state. This indicated that, again as aforementioned, the dispersion process was a competitive process balanced by the removal and adhesive potential. Therefore, an index based on the ratio of the air drag force and the adhesive force was proposed to describe the dispersion behaviour as:

$$D_R = f\left[We\left(\frac{D_{agg}}{D}\right)\right] \tag{2.38}$$

where D_{agg} and D are the diameters of agglomerate and particle, respectively.

The mechanism of the aerodynamic dispersion for agglomerates with different sizes in a uniform air flow was further explored by Calvert *et al.* (2013). It was found that the relative agglomerate size, defined as the ratio of agglomerate size to primary particle size, had a significant influence on the dispersion behaviour: while small agglomerate disintegrated, particles from the outer surface layer were gradually peeled to disperse for larger agglomerates. It was also found that the dispersion rate decreased as the agglomerate size increased. Furthermore, for larger agglomerates particles at the surface dispersed more rapidly than

internal particles; but dispersion occurred in the whole agglomerate for smaller ones.

The work of Ghadiri and co-workers demonstrated again, that DEM is useful to examine the micro-dynamics of agglomerate dispersion.

Yu and co-workers also conducted a series of work on the agglomeration and de-agglomeration processes in DPIs using DEM or CFD-DEM.

They started from the DEM modelling of agglomeration of fine particles subjected to centripetal compaction (Yang *et al.*, 2008). 10000 spherical particles representing the glass beads with a fix size of down to 1 μm were agglomerated under an assumed centripetal force in addition to the van der Waals force between particles. It was found that the coordination number and the packing density exponentially decreased with increasing agglomerate size. The tensile strength also decreased with the increase of particle size.

Using the method of agglomeration described above (Yang *et al.*, 2008) to form loose agglomerates of fine mannitol particles, they continued with the exploration of the breakage process (Tong *et al.*, 2009) caused by the impact between an agglomerate and a wall. It was observed that the agglomerates on impact experienced large plastic deformation and then disintegrated into small fragments, which was consistent with Thornton's previous both simulated and experimental findings as shown in Fig. 2. 11 (Ning *et al.*, 1997a; Thornton *et al.*,

1999). They found that a higher impact velocity led to a better agglomerate breakage performance. For a given impact velocity, a 45-degree impact angle resulted in the maximum breakage compared to those with other impact angles. They also suggested that impact energy including the normal and tangential ones should be used to characterize the breakage performance.

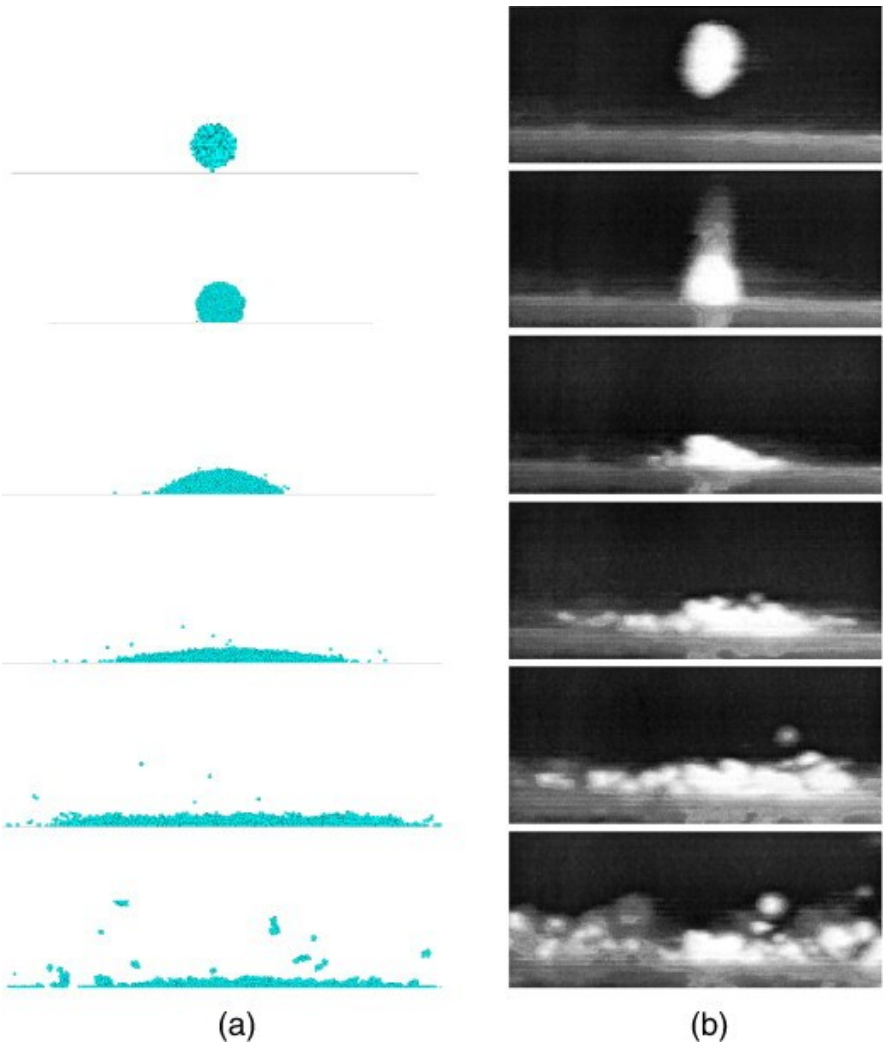

Fig. 2.11. Comparison of the deformation process between simulated and experimental results (Tong *et al.*, 2009).

Their research was further conducted to investigate the dispersion process of agglomerates of different particle sizes and polydispersities in a cyclonic flow at different flow velocities using a combined computational fluid dynamics and discrete element method (CFD-DEM) approach (Tong *et al.*, 2010). It was found that the finer the constituting particles were, the agglomerates were more difficult to disperse at low flow rates but more efficient at high flow rates. Decreasing the particle size distribution range improved the dispersion performance. They also proposed that since the air flow actually affected the particle–wall impact, the dispersion was governed by two competitive interactions, particle–particle cohesion and particle–wall impact. Therefore an index based on the ratio of particle–wall impact energy and agglomerate cohesion energy was proposed to predict the dispersion performance.

The effect of mechanical impact on the de-agglomeration process was also examined by Tong *et al.* (2011). A coupled CFD-DEM approach was utilized to simulate the de-agglomeration of mannitol agglomerates in impact throats containing one or two angles at different flow rates as shown in Fig. 2.12. The results showed that mechanical impact played a dominant role on the agglomerate breakage and the air flow induced shear did not affect the breakage much. It was also found that the two angles played different roles: the first one for causing major damage and the second one for improving the dispersion performance by further breaking the damaged clusters into fine particles. Similar index based on energy ratio was again proposed to characterise the impact induced dispersion performance, indicating that dispersion was a competitive

process. However, it should be noted that the calculations of the impact energy and cohesion energy in their work were based on the step-by-step information of the contact force between the agglomerate and the wall calculated using DEM, which caused difficulties for predicting of other cases or realistic process.

.

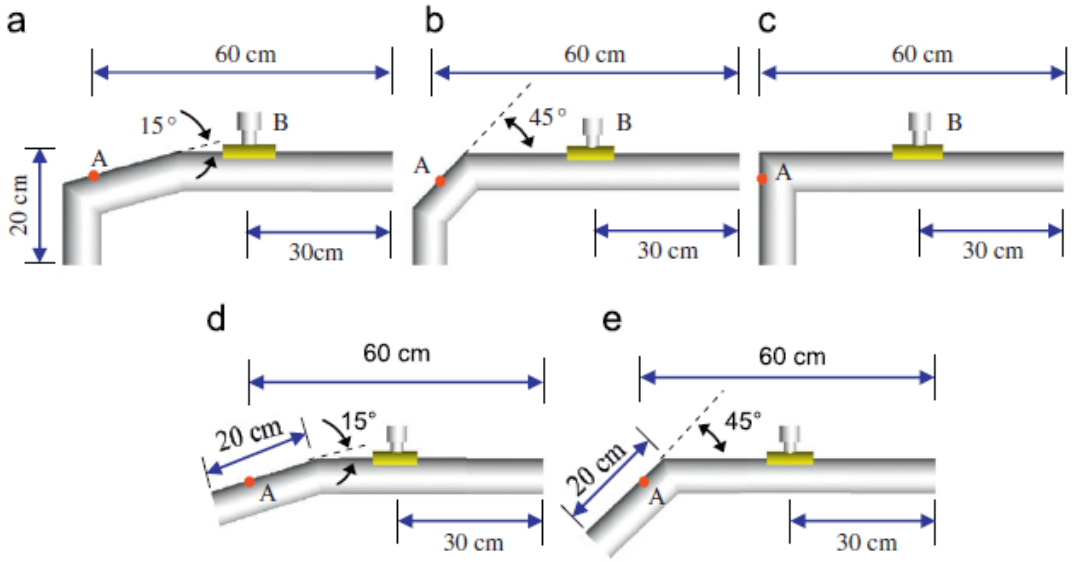

Fig. 2.12. Schematics of impaction throats (Tong *et al.*, 2011).

An improved model, which employed CFD-DEM to simulate the dispersion process of agglomerates formed by polydisperse mannitol powders in commercial dry powder inhaler Aerolizer® as shown in Fig. 2.13, was proposed by Yu and co-workers (Tong *et al.*, 2013). It was found that while impacts between agglomerates and inhaler walls first break the agglomerates into large pieces of fragments, sbusequent impacts between the fragments and the inhaler grids played the role of disintegrating the fragments into fine particles to

dramatically increase the FPF. The inhaler exhibited a better performance at higher air flow rate, but further increasing the air flow rate decreased the FPF due to the larger depositions. This work explored the collective effects in a realistic commercial inhaler, other than mainly focusing on a single factor in the previous works, demonstrated the strong capability of DEM coupled with other modelling tools to provide the detailed information of particle-particle and particle-wall interactions for better understanding the underlying mechanisms and optimization of the realistic inhaler devices.

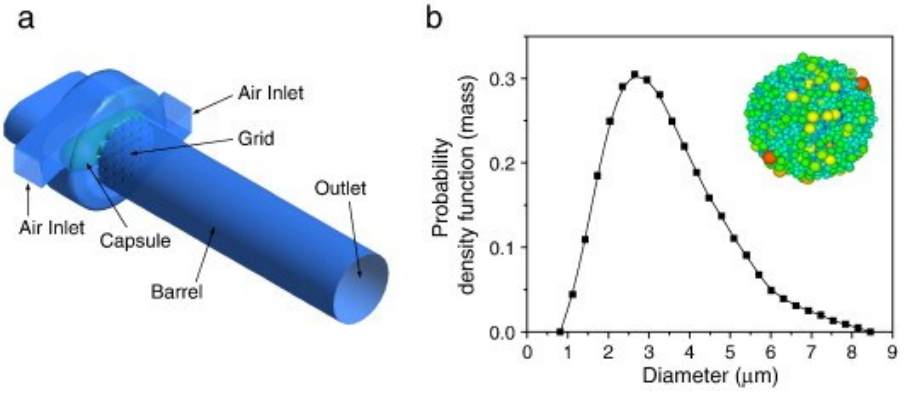

Fig. 2.13. (a) Schematic view of the inhaler and (b) formation of agglomerates (Tong *et al.*, 2013).

The above work provided a comprehensive investigation on the agglomeration and de-agglomeration processes in dry powder inhalers. However, they were focused on the drug-only agglomerates. On the other hand, carrier-based agglomerates were also widely used in DPIs but the agglomeration and de-agglomeration mechanisms for carrier-based ones can be different from those of drug-only ones due to the distinct difference between the microstructures.

More recently, CFD-DEM was applied to investigate the influence of inhaler device design on the dispersion performance of a carrier-based formulation Foradile® in dry powder inhaler Aerolizer® by Zhou *et al.* (2013). It was shown that reducing the inlet size significantly increased the FPF and increasing grid voidage lead to a higher deposition in the induction port. The authors also argued that for the carrier-based formulation, the dispersion mechanism was drug particles sliding and/or rolling on the carrier surface to detach, but for the drug-only formulation, agglomerates were broken up into smaller fragments and primary drug particles for dispersion. Therefore, the mechanisms for agglomeration and de-agglomeration of carrier-based formulations need to be further investigated.

2.3. Summary

Dry powder inhalers as a promising approach for the therapy of respiratory and lung diseases have drawn increasing attention since the complicated nature can be affected by many factors. This chapter first provided an introduction to the background and development of DPIs, and then reviewed the work on the three main factors that govern the DPI performance: the formulation design, the device design and the inspiratory manoeuvre of the patients. Furthermore, the effects of air flow and particle-wall impact on the dispersion performance of DPIs were summarized.

The discrete element method, a numerical approach that provides the positions and velocities of particles and the transient force acting on them and correlate the macroscopic behaviour with the microscopic interactions of particulate systems, was applied to investigate particulate issues in many fields including powder agglomeration and de-agglomeration. The theory and development of DEM was reviewed followed by the summary of its applications in DPIs.

CHAPTER 3: VAN DER WAALS FORCE INDUCED ADHESION

*Published as “Yang, J., Wu, C.Y., Adams, M. DEM analysis of particle adhesion during powder mixing for dry powder inhaler formulation development. *Granular Matter*, 2013, 15, (4) 417-426”.

Abstract

Understanding the adhesive interactions between active pharmaceutical ingredient (API) particles and carrier particles in dry powder inhalers (DPIs) is critical for the development of formulations and process design. In the current study, a discrete element method (DEM), which accounts for particle adhesion, is employed to investigate the attachment processes in DPIs. A critical velocity criterion is proposed to determine the lowest impact velocity at which two elastic auto-adhesive spherical particles will rebound from each other during impact. Furthermore, the process of fine API particles adhering to a large carrier in a vibrating container is investigated. It was found that there are optimal amplitude and frequency for the vibration velocity that can maximise the number of particles contacting with the carrier (i.e. the contact number). The impact number and detachment number during the vibration process both increase with increasing vibration amplitude and frequency while the sticking efficiency decreases as the amplitude and frequency are increased.

Keywords: adhesion; discrete element method; attachment; mixing; granular materials.

3.1. Introduction

Dry powder inhalers (DPIs) are widely used for treating pulmonary and respiratory diseases, which can directly deliver micron-sized active pharmaceutical ingredient (API) particles to the lungs and respiratory tracts (Islam and Gladki, 2008; Newman and Busse, 2002; Smith and Parry-Billings, 2003). Since the API particles are generally very small (< 5 μm), they are extremely cohesive and have poor flowability (Pritchard, 2001). To improve the flowability and dispersion efficiency of DPI formulations, API particles are either mixed with large carrier particles or aggregated into large agglomerates (Aulton and Taylor, 2001). The attractive potential between API and carrier particles or other API particles is mainly due to van der Waals forces, electrostatic forces and capillary forces (Hinds, 1999). The effective forces have to be sufficiently strong so that fine API particles can adhere with the carriers or form large agglomerates to be transported, but weak enough so that they can be detached or dispersed by a de-agglomeration process and thus allow the delivery of the API particles into the respiratory tracts and lungs. Therefore, particle-particle interactions play a significant role in controlling the performance of DPIs and hence many studies have been performed to explore the dependency of these interactions on particle size (Guenette *et al.*, 2009; Kaialy *et al.*, 2012a), material properties (Hassan and Lau, 2010; Steckel and Bolzen, 2004), particle concentration (Steckel and Muller, 1997; Young *et al.*, 2005), particle morphology (Kaialy *et al.*, 2011; Kaialy *et al.*, 2012b), particle surface roughness (Kaialy *et al.*, 2012c; Young *et al.*, 2008), storage conditions (Jashnani *et al.*,

1995; Le *et al.*, 2012), surface area (Cline and Dalby, 2002), density and porosity (Kaialy and Nokhodchi, 2012), and crystal form (Shur *et al.*, 2012). For example, Kaialy *et al.* (2012a) experimentally examined the influence of the particle size of lactose carrier on the DPI performance and demonstrated that the DPI performance improved with decreasing carrier particle size. Young *et al.* (2005) investigated the relationship between API dosage (drug/lactose ratio) and aerosolisation performance of conventional carrier based formulations using the twin stage impinger and found that the fine particle fraction (FPF) decreased with increasing API dosage when the API dosage was low (10-135 μg/50 mg), while the FPF increased with increasing API dosage at large values of the API dosage (135-450 μg/50 mg). These results were attributed to the effect of "active sites", which were preferentially occupied by API particles due to large contact area, high surface energy and simple geometric constrains. Therefore, there was a critical API dosage below which FPF decreased since API particles were adhered to the active sites, and above which FPF increased since the active sites were fully occupied with excessive API particles presenting in the formulation. Kaialy *et al.* (2012c) also found that lactose particles with an elongated shape, more irregular shapes and a rougher surface could deliver more API particles to lower airway regions. Le *et al.* (2012) employed a twin stage impinger to evaluate the dispersion performance at various humidity conditions and found that the FPF decreased as the relative humidity is increased. Cline and Dalby (2002) found that the FPF increased with the increased surface area. Kaialy and Nokhodchi (2012) suggested that engineered lactose with smaller bulk and tap density and higher porosity improved the

homogeneity of drug content and the dry powder inhaler performance. Shur *et al.* (2012) used seed crystals and supercritical carbon dioxide crystallization to produce ipratropium bromide monohydrate and anhydrous crystals, respectively, and found that these two crystals exhibited similar mechanical and interfacial properties, which also resulted in the similar DPI performance.

As the first step in preparing DPI formulations, the attachment of API particles to carrier particles is a critical stage for controlling the performance of DPIs. This is generally realised through mixing APIs with carriers in a blender, which determines the formulation quality and efficiency (Jones and Price, 2006; Le *et al.*, 2012; Selvam *et al.*, 2011; Zeng *et al.*, 1999). Both mixing conditions (e.g. mixing time, mixing speed) and mixing processes can influence the formulation properties. For example, Selvam *et al.* (2011) explored the effect of mixing time on the drug attachment process and found that the drug loading increased with increasing mixing time. They argued that this was due to the formation of drug-drug aggregates on the surface of the carrier particles as more drug particles were adhered over time. However, Le *et al.* (2012) investigated the influence of mixing conditions on the API content and demonstrated that the mean API contents of the blends were poorly correlated with the mixing time. These discrepancies might be caused by the different mixing times used (i.e. 1-30 min by Selvam *et al.* (2011) and 60-180 min by Le *et al.* (2012)) and different materials investigated (i.e. Selvam *et al.* (2011) used budesonide drug and polyolefin medical packaging films, while Le *et al.* (2012) considered lactose carrier and Fluticasone Propionate drug).

The effect of mixing processes on formulation properties and DPI performance has also been investigated (Dickhoff *et al.*, 2003; Jones and Price, 2006; Saleem *et al.*, 2008; Zeng *et al.*, 1999). Johns *et al.* (2006) showed that the addition of fine excipient particles during the mixing process increased the pulmonary delivery of the drug and there was an optimal concentration of added excipients . Zeng *et al.* (1999) used a twin stage impinger to investigate the effect of different sequences of addition on *in vitro* deposition. They found that the formulation prepared by first blending micronized lactose with coarse lactose before mixing with salbutamol sulphate produced a greater fine particle fraction and fine particle dose of salbutamol sulphate than the same formulation prepared using a different mixing order of the three components. Saleem *et al.* (2008) used two lactose carrier systems (spray-dried and milled) and investigated the effects of surface energy and the so-called 'rate of blending' on the aerosol dispersion performance. They observed that the surface energy was inversely proportional to the DPI performance while the blending rates positively correlated with the performance. Dickhoff *et al.* (2003) explored the effect of carrier payload (0.4-6.0% w/w of drug) on the dispersion performance of drug particles from adhesive mixtures and demonstrated that the amount of the residual drug on the carrier decreased with increasing carrier payload at a flow rate of 60 l/min. All these studies demonstrated that mixing is crucial in controlling the formulation quality, efficiency and performance of DPIs. Therefore, an improved understanding of the mechanism of particle adhesion and the drug attachment process during mixing is critical for enhancing not only the formulation quality, but also the performance of DPIs.

Although many efforts have been made to investigate the attachment process of DPI formulations, the underlying mechanisms, especially at the microscopic level, are still not well understood. Therefore, a Discrete Element Method (DEM) analysis is reported in this paper in order to provide insights into the attachment process during mixing. The impact between two spheres is first analysed to establish a criterion for determining whether two particles will attach or rebound during an impact. In addition, the adhesive interaction between API particles and a large carrier particle in a vibrating container is analysed and the effects of vibration conditions are examined.

3.2. DEM with adhesion

The DEM for adhesive particles developed by Thornton and Yin (1991) is used in this study. The translational and rotational motions of a particle are governed by the Newton's second law:

$$m_i \frac{\mathrm{d}\mathbf{v}_i}{\mathrm{d}t} = \mathbf{f}_{ci} + m_i \mathbf{g} \tag{3.1}$$

$$I_i \frac{\mathrm{d}\boldsymbol{\omega}_i}{\mathrm{d}t} = \mathbf{T}_i \tag{3.2}$$

where m_i , I_i , $\mathbf{v}_i$, $\boldsymbol{\omega}_i$ are the mass, moment of inertia, translational and rotational velocities of particle i , respectively. $\mathbf{f}_{ci}$ and $\mathbf{T}_i$ are the contact force and torque acting on the particle. $\mathbf{g}$ is the gravitational acceleration.

Due to the particle sizes of APIs and carriers used in DPIs, adhesion becomes important in governing the interaction between particles. Therefore, JKR theory (Johnson *et al.*, 1971) is applied to model the adhesion between particles, in which the relationship between the normal contact force P (i.e. normal component of $\mathbf{f}_{ci}$) and relative normal displacement α is given as (Johnson, 1985):

$$\frac{\alpha}{\alpha_F} = \frac{3\left(\frac{P}{P_C}\right) + 2 \pm 2\left(1+\frac{P}{P_C}\right)^{1/2}}{3^{2/3}\left[\frac{P}{P_C} + 2 \pm 2\left(1+\frac{P}{P_C}\right)^{1/2}\right]^{1/3}} \tag{3.3}$$

where α_F and P_C are the displacement at which the two adhesive spheres are separated and the "pull-off" force with which the two adhesive spheres can be separated, and given as:

$$\alpha_F = \frac{3}{4}\left(\frac{\pi^2\Gamma^2 R}{E^2}\right)^{1/3} = \left(\frac{3P_C{}^2}{16RE^2}\right)^{1/3} \tag{3.4}$$

$$P_C = \frac{3}{2}\Gamma\pi R \tag{3.5}$$

$$R = \frac{R_1 R_2}{R_1 + R_2} \tag{3.6}$$

$$\frac{1}{E} = \frac{1-\nu_1{}^2}{E_1} + \frac{1-\nu_2{}^2}{E_2} \tag{3.7}$$

in which Γ is the thermodynamic work of adhesion, and R and E are the effective radius and Young's modulus, R_i, E_i and υ_i are the radius, Young's modulus and Poisson's ratio of the particles i. The meaning of $\pm$ is: while + indicates that the α/α_F increases with increasing P/P_C, - indicates that the α/α_F decreases with increasing P/P_C.

3.3. DEM models

Using DEM, impacts between two adhesive particles and mixing of API particles with a carrier particle in a vibrating container are simulated. The corresponding DEM models are presented in this section.

3.3.1. Impact between two spheres

Two identical particles with the properties given in Table 3.1 are created to impact collinearly with each other in the presence of adhesion as shown in Fig. 3.1. The initial velocities of the two particles are V_1 and V_2, which have the same magnitudes but are in opposite directions (i.e. $V_1 = -V_2$). Gravity is not considered in this case.

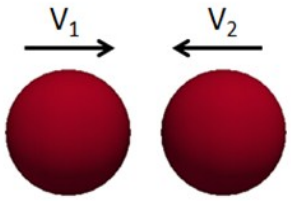

Fig. 3.1. Illustration of the normal impact between two spheres.

Table 3.1. Physical properties of particles for the impact between two spheres.

Parameter	Value
Diameter (μm)	1-100
Density (kg/m^3)	2650
Young's modulus (GPa)	70
Poisson's ratio	0.3
Coefficient of friction	0.3
Thermodynamic work of adhesion (J/m^2)	0.044-4.4

3.3.2. Mixing of carrier and API particles in a vibrating container

Mixing of one carrier particle and N API particles in a vibrating cubic container is modelled in 3D. The side length of the container is l. All the carrier and API particles are spherical particles. The diameter of the carrier particle and mono-sized API particles are 70 μm and 5 μm, respectively. The carrier particle is initially located at the centre of the container while the API particles are randomly generated in the empty space in the container as shown in Fig. 3.2a. The carrier and API particles are then allowed to settle to the bottom of the container under gravity as shown in Fig. 3.2b. Once the kinetic energy of the system (carrier and

API particles) becomes negligible, the container is set to vibrate vertically with a velocity profile defined as:

$$V = V_0 \sin(2\pi f t) \tag{3.8}$$

where V is the velocity of the container; V_0 is the amplitude; f is the frequency; t is the time. The simulation parameters are given in Table 3.2. It is assumed that the API particles and the carrier have the same material properties as α-lactose monohydrate (Alderborn and Nystrom, 1996). The time step, determined by the Rayleigh criterion using the properties of the API particle, is 4.5×10^{-10} s. A viscous damping is introduced to consider the energy dissipation in the system.

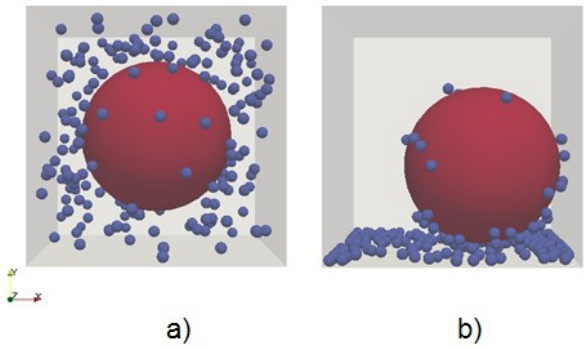

Fig. 3.2. Model setup for vibrating container cases.

Table 3.2. Simulation parameters for mixing of the carrier with APIs in a vibrating container.

Parameter	Value
Density (kg/m^3)	2650
Young's modulus (GPa)	24

Poisson's ratio	0.3
Friction coefficient	0.3
Thermodynamic work of adhesion (J/m^2)	0.006
V_0 (m/s)	0.02 - 0.06
f (Hz)	30 - 120
l (μm)	105
N	200

3.4. Impact between two spheres with adhesion

3.4.1. Impact behaviour

Fig. 3.3 shows the evolution of the relative displacement, normal force and relative velocity during the impact of two spheres at V_1 = -V_2 =0.0058 m/s. The abscissa shows the time normalized by the duration from the beginning of the contact until the time instant at which the relative displacement reduces to zero. It can be seen that for auto-adhesive particles, the relative displacement initially increases until a maximum value is reached, when the relative velocity reaches zero. Thereafter the relative displacement reduces. However, due to the adhesion, the two spheres cannot separate from each other when the relative displacement reduces to zero, and they continue to move in opposite directions until the relative displacement reduces to a certain value (i.e. α_F as described in Eq. (3-4)). Correspondingly, once the two spheres come into contact a finite

normal force is suddenly induced due to auto-adhesion. Then the normal force increases with increasing the relative displacement until the relative velocity of the two spheres reaches zero, which corresponds to a maximum contact force. The normal force then starts to reduce until it reaches $-P_C$ as described by Eq. (3-5). Thereafter it reduces to zero at the moment of separation. The relative velocity increases first due to the auto-adhesion and then decreases until a minimum value is reached, where the force reduces to zero. Thereafter it increases again until the two spheres separate from each other. On the other hand, without auto-adhesion, both the relative displacement and the normal force firstly increase from zero to maximum values at which the velocity reaches zero, and then decrease to zero with time.

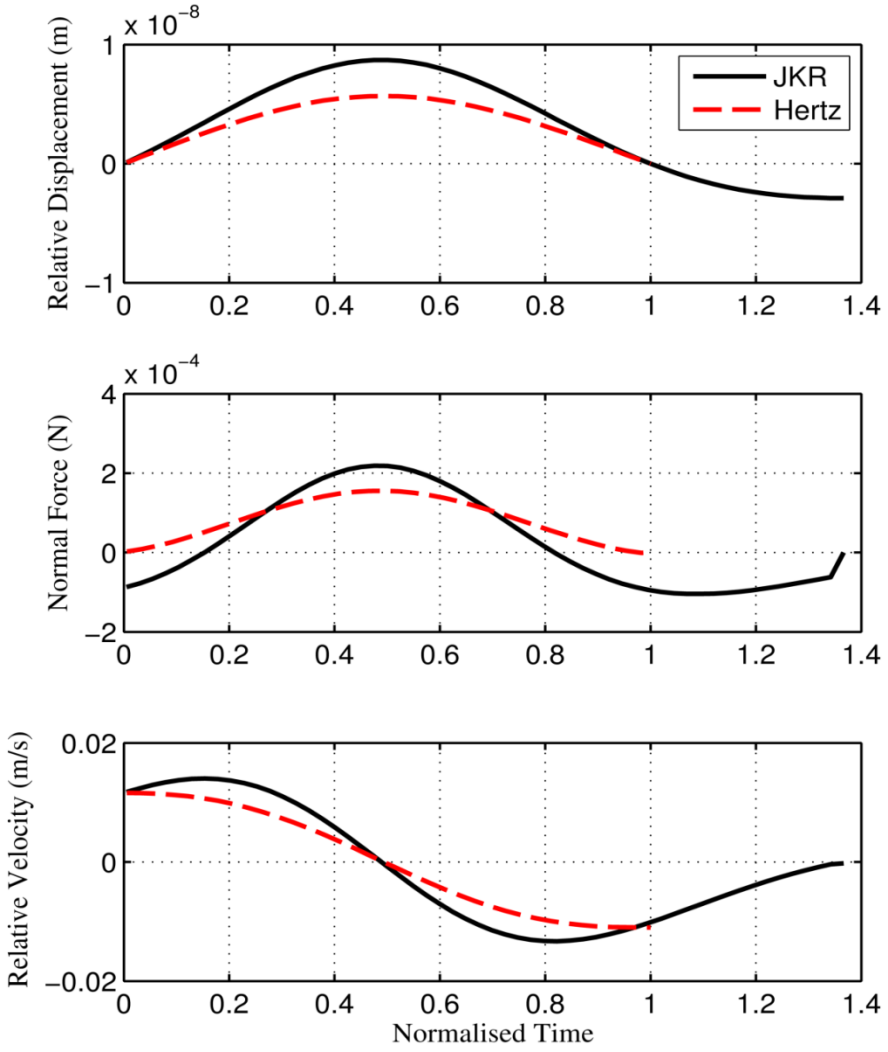

Fig. 3.3. The evolution of the relative displacement, normal force and relative velocity for the impact between two particles with initial velocities of ±0.0058 m/s.

Fig. 3.4 shows the variation of the normalized contact force with the normalized relative displacement. The force acts on the two particles only when they are in contact with each other during the loading process, and the force increases with increasing displacement until a maximum value is reached. Then the unloading process starts and the force decreases as the displacement decreases. It is worth noting that the two particles do not separate from each other when the

displacement reduces to zero due to the adhesion and they will continue moving in the opposite directions until the displacement reaches α_F, at which point they separate from each other and the impact process ends. In Fig. 3.4, the theoretical prediction using JKR theory (i.e. Eq. (3-3)) is also superimposed. It is clear that the numerical results are in excellent agreement with the theoretical predictions, which implies that the model is correctly implemented and can be used to model impact behaviour of particles in the presence of adhesion.

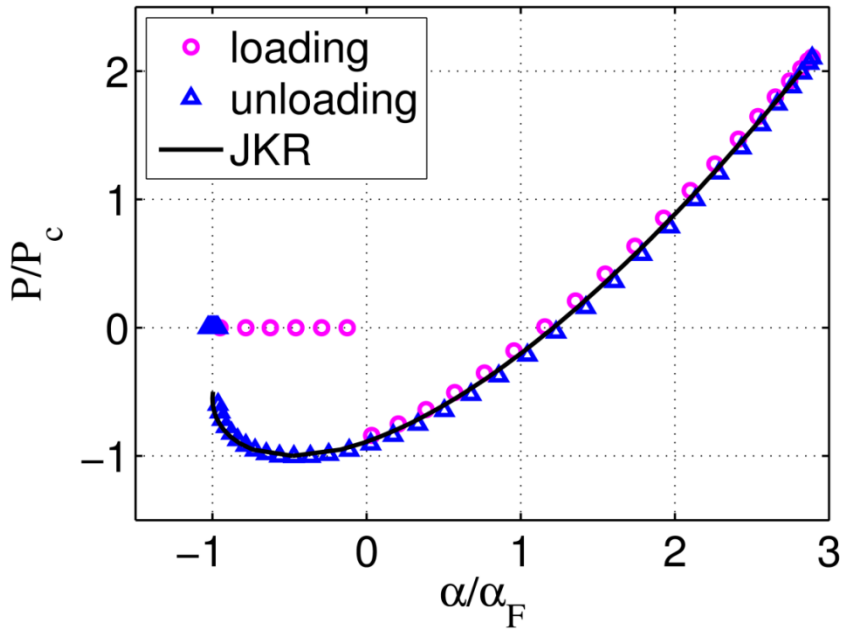

Fig. 3.4. The force-displacement relationship for impact between two particles with initial velocities of ±0.0058 m/s.

When the initial velocities of the two particles are reduced to ±0.0050 m/s, the corresponding results are shown in Fig. 3.5 and Fig. 3.6. It can be seen from Fig. 3.5 that the loading and unloading processes are similar to those shown in Fig. 3.3; however, the two spheres cannot separate from each other when the

unloading process ends. As a result, cyclic loading and unloading take place, and the relative displacement increases again, and the evolutions of normal force and velocity also repeat the similar trends as those in the first loading process. It is worth noting that the amplitudes of relative displacement, normal force and velocity monotonically decrease in the subsequent impacts and eventually the two spheres adhere to each other, since some kinetic energy is dissipated due to the adhesion in each impact. Fig. 3.6 shows the normalized impact force as a function of the normalized displacement. It can be seen that the loading and unloading curves are similar to those shown in Fig. 3.4. However, the two particles cannot separate from each other and will continue reloading until they stick together.

From the impacts with different initial velocities, it is found that due to the effect of the attractive force only the particles with sufficient initial kinetic energy (i.e. initial velocity) can rebound, while particles without sufficient initial kinetic energy will stick to each other. Therefore, there must be a critical initial velocity above which particles will rebound. An accurate determination of this critical velocity is crucial for the analysis of the attachment and detachment processes in DPIs and will be discussed in the next subsection.

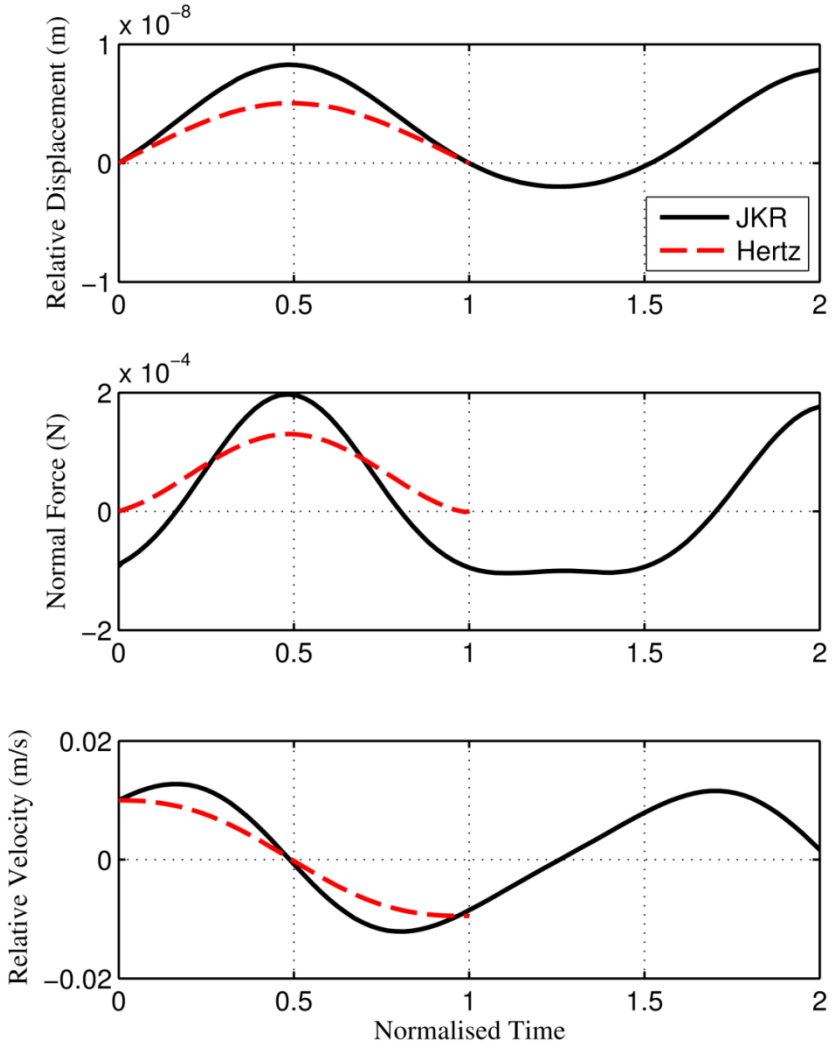

Fig. 3.5. The evolution of relative displacement, normal force and relative velocity for the impact between two particles with initial velocities of ±0.0050 m/s.

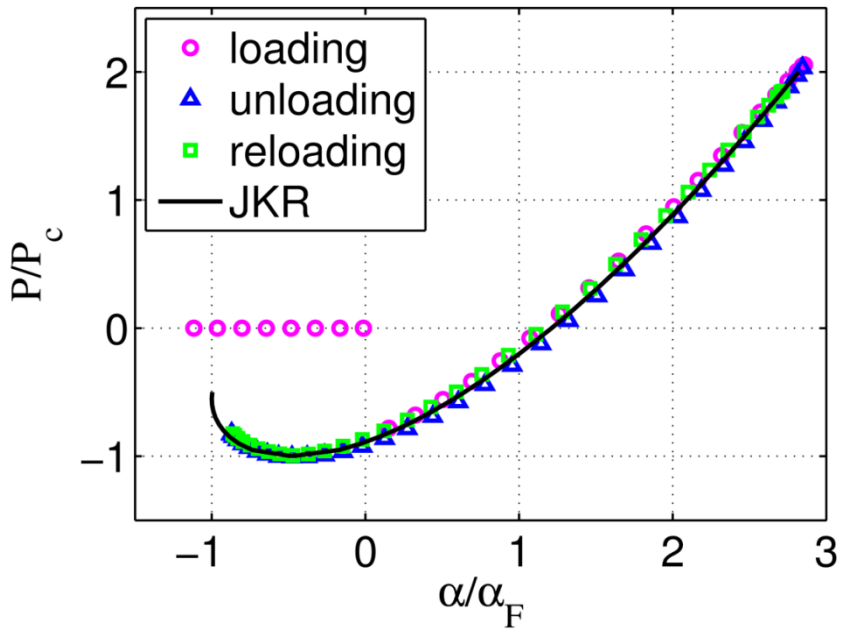

Fig. 3.6. The force-displacement relationship for the impact between two particles with initial velocities of ±0.0050 m/s.

3.4.2. Critical Velocity

As shown in Fig. 3.3, there is still a finite force acting on the spheres when the relative displacement reduces to zero during the unloading process. Thereafter the two spheres move in the opposite directions and the work done by the adhesive force dissipates some kinetic energy and possibly all the kinetic energy, which prevent the spheres separating. Therefore, only particles with sufficiently high kinetic energy will be able to rebound by overcoming the adhesive work, while others will stick to each other.

In order to accurately obtain the critical velocity, it is essential to calculate the work done by the adhesive force. Thornton and Ning (1998) integrated the JKR

force-displacement curve (described as Eq. (3-3)) in the region of $-1 \le \alpha / \alpha_F \le 0$ and obtained the initial kinetic energy or the work to break the adhesive contact W_S :

$$W_S = 7.09\left(\frac{\Gamma^5 R^4}{E^2}\right)^{1/3} \tag{3.9}$$

Therefore, if energy loss due to elastic wave propagation is negligible, particles will rebound only when

$$\frac{1}{2}m_1 V_1^2 + \frac{1}{2}m_2 V_2^2 \ge W_S \tag{3.10}$$

where m_1 , m_2 are the mass of the two particles and V_1 , V_2 are the impact velocities of the two particles.

For the cases $m_1 = m_2$, $V_1 = -V_2$, Eq. (3.10) can be rewritten as

$$\frac{1}{2}m^* V^2 \ge W_S \tag{3.11}$$

where

$$m^* = \frac{m_1 m_2}{m_1 + m_2} \tag{3.12}$$

and the relative impact velocity, V, is defined as

$$V = |V_1 - V_2| \tag{3.13}$$

Using Eq. (3.9), the critical velocity, V_C, can be obtained as

$$V_C = \left(\frac{14.18}{m^*}\right)^{1/2} \left(\frac{\Gamma^5 R^4}{E^2}\right)^{1/6} \tag{3.14}$$

For the cases in which two different spheres rebound from each other, denoting the rebound velocities of the two spheres as V_{1r} and V_{2r}, the following equation should be satisfied:

$$\frac{1}{2} m_1 V_1^2 + \frac{1}{2} m_2 V_2^2 - \frac{1}{2} m_1 V_{1r}^{\ 2} - \frac{1}{2} m_2 V_{2r}^{\ 2} = W_S \tag{3.15}$$

From Eq. (3.13) and Eq. (3.14), we have

$$\frac{1}{2} m^* V_C^2 = W_S \tag{3.16}$$

Since in current cases, $m_1 = m_2$, $V_1 = -V_2$ and $V_{1r} = -V_{2r}$, substituting Eq. (3.16) into Eq. (3.15) yields:

$$V_C = \left(V^2 - V_r^2\right)^{1/2} \tag{3.17}$$

where the relative rebounding velocity V_r is defined as

$$V_r = \left|V_{1r} - V_{2r}\right| \tag{3.18}$$

In the current numerical analysis, a low impact velocity was initially set for the two particles at which they will stick to each other after impact. The velocity was then incrementally increased until the two particles separate from each other after the impact. V and V_r, defined in Eq. (3.13) and Eq. (3.18) respectively, can be obtained from the case in which two spheres rebound from each other, then the critical velocity can be obtained using Eq. (3.17).

As the critical velocity is crucial for the understanding of the attachment and detachment process in DPIs, different cases with different particle sizes and work of adhesion are then simulated to investigate their effects on the critical velocity. Fig. 3.7 shows that for the same material (i.e. the same work of adhesion, Γ=0.44 J/m^2), the critical velocity decreases with increasing particle radius. Fig. 3.8 illustrates the effect of the work of adhesion on the critical velocity. For a given particle radius (i.e. $R_1 = R_2$ =100 μm), the critical velocity increases with increasing work of adhesion. It can also be seen that the DEM results are in excellent agreement with the theoretical values obtained from Eq. (3.14), which indicates that the current model can accurately predict the critical velocity for impacts in the presence of adhesion.

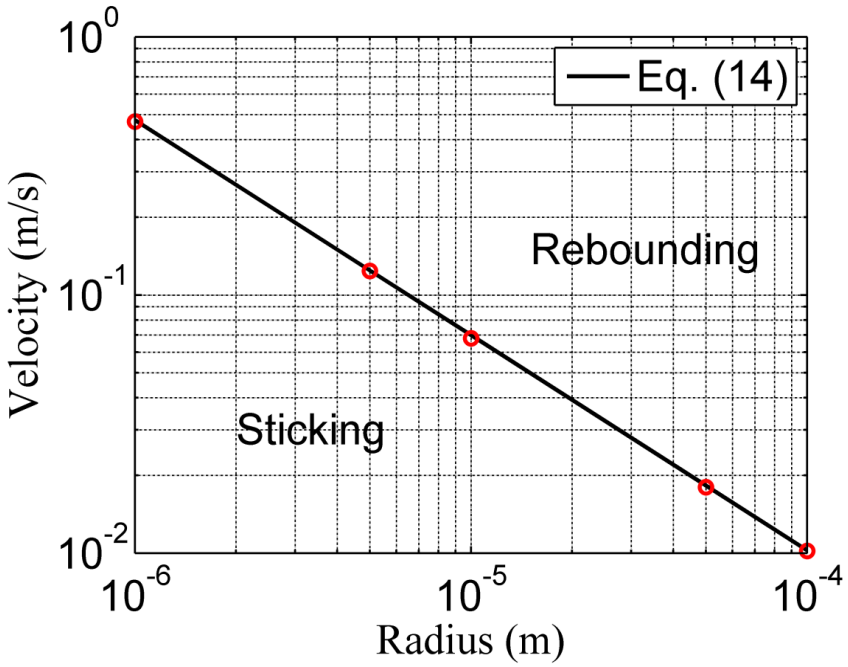

Fig. 3.7. The variation of the critical sticking velocity with particle radius (Γ =0.44 J/m).

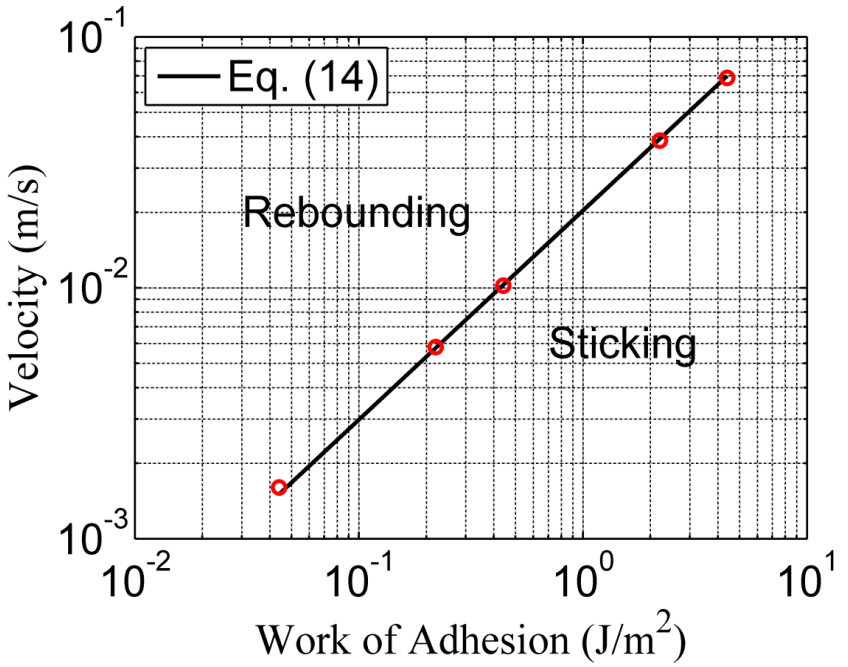

Fig. 3.8. The variation of the critical sticking velocity with the work of adhesion ($R_1 = R_2$ =100 μm).

3.5. Mixing of carrier and API particles in a vibrating container

In this section, the mixing process of one carrier particle and a number of API particles in a vibrated container is analysed using DEM, and the effects of the vibration amplitude and frequency on the mixing performance are discussed.

3.5.1. Vibration process

Fig. 3.9 shows snapshots at various time instants during the vibration process for a typical case. It can be seen from Fig. 3.9a that a few API particles adhere to the carrier when the container starts to vibrate. During the vibration process the carrier and API particles oscillate in the vertical direction and an increasing number of impacts occurs between the carrier and API particles as shown in Fig. 3.9b. An increasing number of API particles stick to the carrier as the vibration continues until a stable status is reached (Fig. 3.9c).

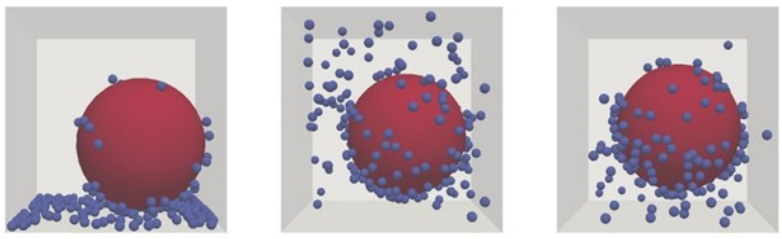

a) t=0.0750 s b) t=0.1205 s c) t=0.2251 s

Fig. 3.9. Snapshots at different time instances.

Fig. 3.10 illustrates the corresponding evolution of the contact number (N_c , the number of API particles contacting with the carrier). During the deposition process, about 50 API particles adhere to the carrier and a steady state value of N_c is reached. Once the container starts to vibrate, the contact number increases as the time is increased until it reaches a stable status. Fluctuations are apparent during the vibration process due to the impact between the container walls and the carrier particle. The results in the stable state (i.e. time period in the rectangular box shown in Fig. 3.10) are further analysed to obtain the mean and standard deviation of the contact number, which will be discussed in the following sections.

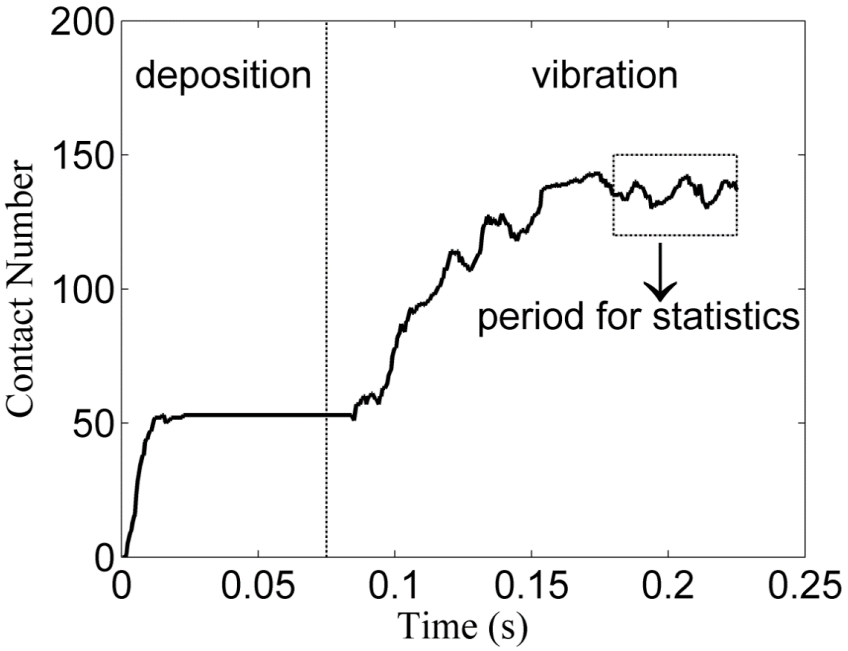

Fig. 3.10. The evolution of the contact number.

3.5.2. Effect of vibration amplitude

The variation of the mean and standard deviation of the contact number with vibration velocity amplitude, during the period indicated in the rectangular box in Fig. 3.10, is shown in Fig. 3.11. The vibration amplitudes V_0 in these cases are different while the vibration frequency is fixed at f =60 Hz. The contact number first increases and then decreases with increasing vibration velocity amplitude. As a result there is an optimal amplitude at which the contact number is a maximum. Moreover there exists a threshold amplitude below which the container cannot agitate API particles. On the other hand, the contact number will decrease due to “over-vibration” when the amplitude is larger than the optimal value.

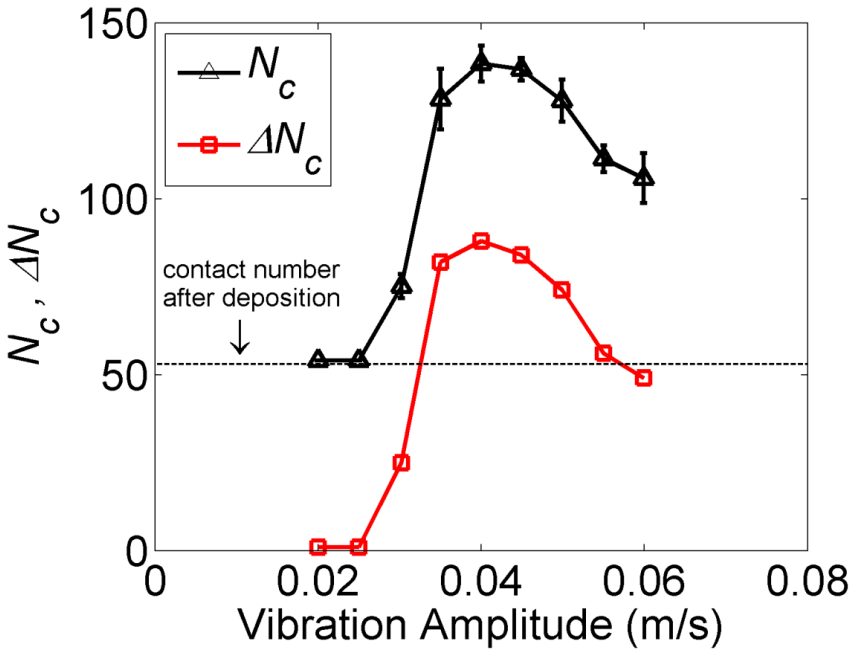

Fig. 3.11. The variations of contact number and incremental contact number with the vibration velocity amplitude.

The incremental contact number ΔN_c during the whole vibration process is also shown in Fig. 3.11. Impacts between the API particles and the carrier particle are monitored during the process, then ΔN_c can be obtained as:

$$\Delta N_c = N_i \eta_s - N_d \tag{3.19}$$

where N_i is the total number of impacts between the carrier and API particles during the process, η_s is the sticking efficiency that indicates the percentage of API particle adhering to the carrier after an impact, and N_d is the total detachment number (the number of API particles which originally adhered to the carrier but are detached due to impact between the carrier particle and container wall or other removal forces). The variations of the impact number, sticking efficiency and detachment number as a function of the vibration amplitude are shown in Fig. 3.12. It can be seen that the impact number and detachment number both increase with increasing vibration amplitude while the sticking efficiency slightly decreases as the amplitude is increased. According to Eq. (3-19), the incremental contact number first increases and then decreases with increasing vibration amplitude. It is worth noting that the incremental contact number is obtained for the whole vibration process while the contact number gives the average value during the stable period highlighted in Fig. 3.10.

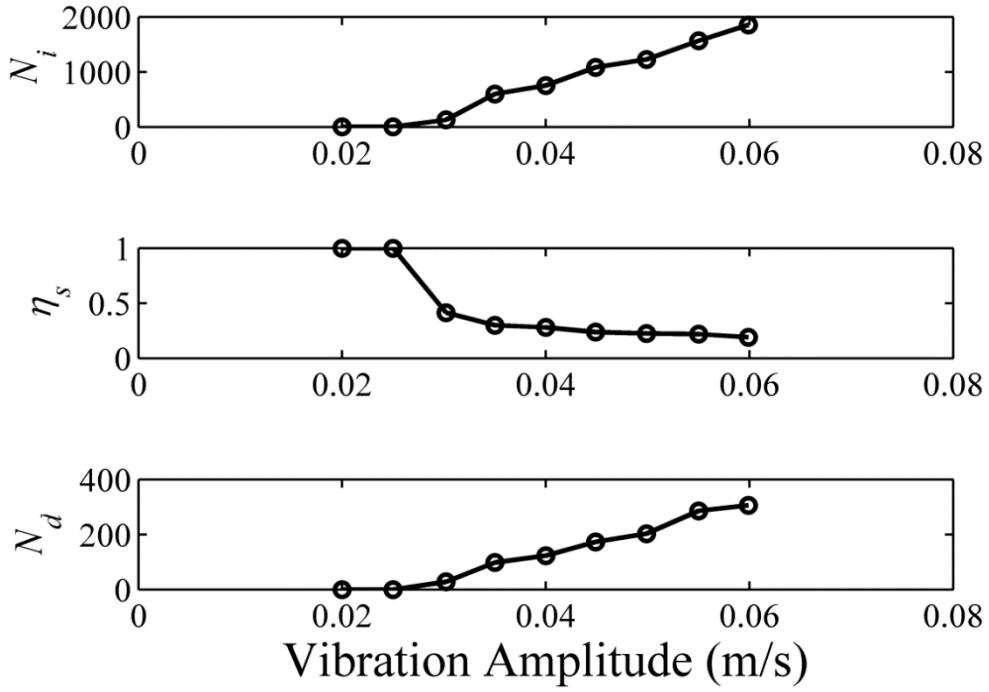

Fig. 3.12. The variations of the impact number, sticking efficiency and detachment number as a function of vibration amplitude.

3.5.3. Effect of vibration frequency

Fig. 3.13 indicates the effect of vibration frequency on the contact number for a fixed vibration velocity amplitude V_0=0.04 m/s. It shows that an optimal vibration frequency can be obtained as the contact number first increases and then decreases with an increase in the vibration frequency. Moreover, vibration with a very low frequency (< 40 Hz) cannot agitate the particles efficiently as the contact number hardly increases during the vibration process. It also can be seen that the incremental contact number obtained by Eq. (3-19) presents a similar trend. Fig. 3.14 shows the variations of the impact number, sticking efficiency and detachment number as a function of the vibration frequency. The

impact number and detachment number both increase with increasing vibration frequency while the sticking efficiency slightly decreases as the frequency is increased.

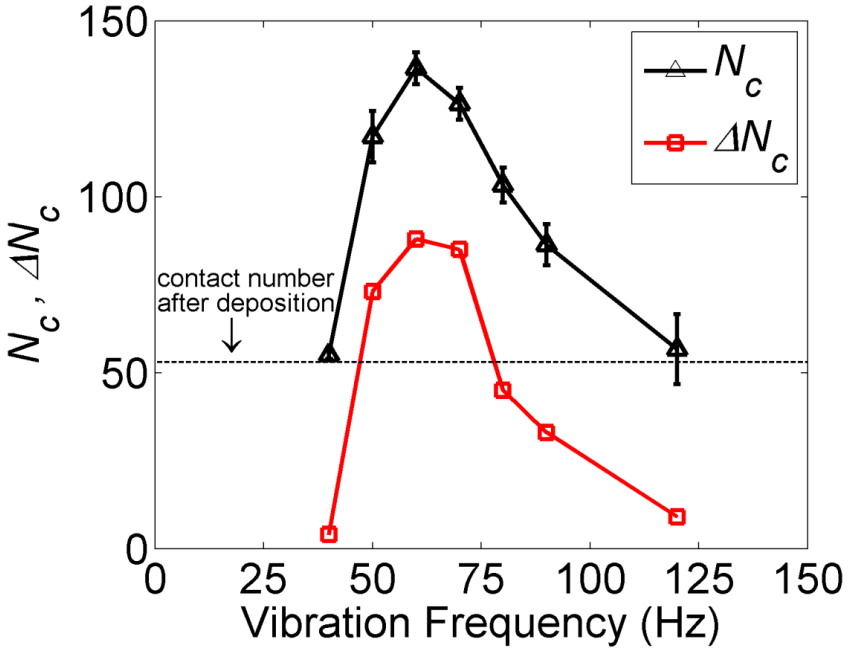

Fig. 3.13. The variations of contact number and incremental contact number with the vibration frequency.

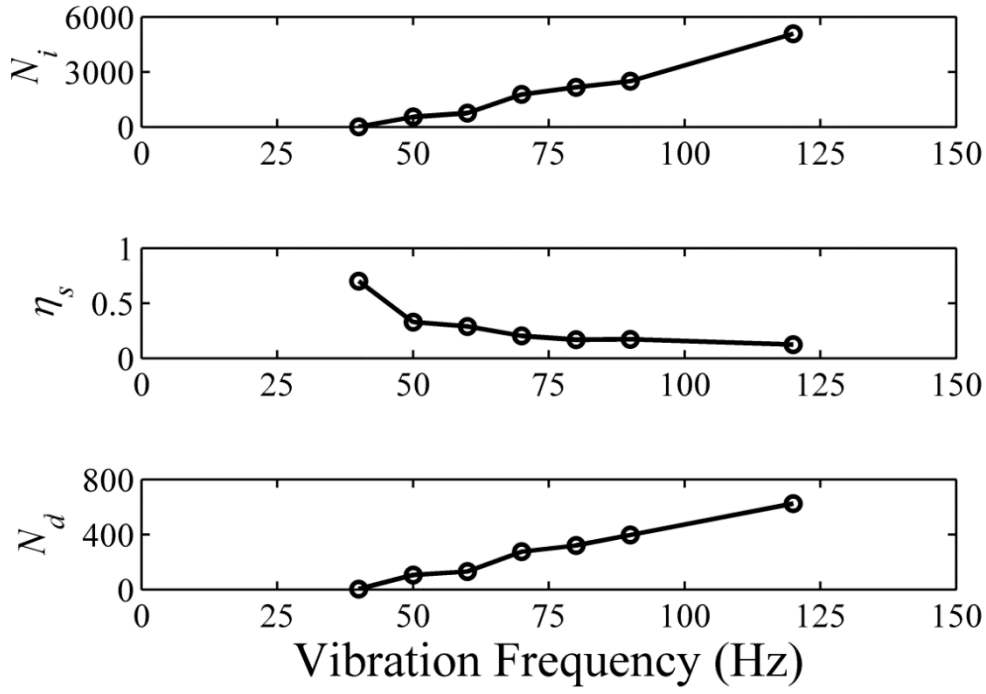

Fig. 3.14. The variations of impact number, sticking efficiency and detachment number against vibration frequency

3.6. Discussion

3.6.1. Critical velocity during impact between two spheres

A knowledge of the critical sticking velocity is very important for understanding the macroscopic behaviour of DPI formulations and provides science-based guidance for DPI formulation design. It is clear from the DEM simulations and predictions using Eq. (3-14) that increasing particle radius and decreasing work of adhesion can decrease the critical velocity. This implies that, for impact-dominant dispersion processes, the dispersion performance in DPIs can be improved by using large particles with low work of adhesion, which will have a

low critical sticking velocity so that particles can be dispersed more easily. It should be noted that the present analysis focuses on collinear impacts. Further analysis is needed for investigating the dispersion performance in processes dominated by oblique impacts of particles.

3.6.2. Attachment process during mixing in a vibrating container

Generally, the contact number during the attachment process is determined by the balance of the removal forces (i.e. impact force and gravitational force in the current cases) and adhesive forces (i.e. caused by the effect of the thermodynamic work of adhesion in the current cases) acting on the particles. However, the overall performance of attachment can be affected by many factors (e.g. vibration velocity amplitude and frequency). The current numerical analysis shows that there are optimal vibration velocity amplitude and frequency that maximise the contact number. API particles are oscillated in the vertical direction within the vibrating container, which may impact with the carrier particle. Once the impact velocity is lower than the critical sticking velocity, API particles may stick to the carrier. The optimal amplitude and frequency corresponding to the maximum contact number should be sufficiently large to agitate API particles from the bottom of the container but sufficiently small in order to avoid too many particles that initially stick with the carrier but are detached during impacts when the vibrating velocity and frequency are too high (i.e., over-vibration). As shown in Fig. 3.12, the total impact number during the vibration process increases as the vibration velocity is increased, which indicates that API particles have more

opportunities to impact with the carrier. On the other hand, as the vibration velocity is increased, the sticking efficiency decreases. This can be explained by the increasing impact velocity between the carrier and API particles with the increase of vibration velocity. As a result, many particles impact with the carrier with an impact velocity that is greater than the critical sticking velocity and thus rebound from the carrier. In addition, a higher vibration velocity causes more originally sticking API particles to detach from the carrier due to impacts between the carrier particle and the container walls. Therefore, there is an optimal vibration condition that maximises the contact number.

3.7. Conclusions

A discrete element method taking into account the adhesion is employed to investigate the attachment processes in DPIs. The analysis of the impact behaviour of two elastic spheres shows that spheres with different initial kinetic energy can either stick or rebound. A critical sticking velocity from an energy analysis is introduced to determine whether two elastic spheres rebound or stick to each other during impact in the presence of adhesion. Moreover, it shows that the critical sticking velocity increases with increasing work of adhesion and decreasing particle radius. An excellent agreement between the numerical results and the theoretical predictions for the two-sphere impact indicates that DEM can be used to model impact behaviour of particles in the presence of adhesion. The attachment process of API particles with a carrier particle in a vibrating container is then investigated. It is shown that there are optimal

vibration velocity amplitude and frequency to maximise the contact number. A close examination of the mixing process reveals that the impact number and detachment number during the vibration process both increase with increasing vibration amplitude or frequency while the sticking efficiency decreases as the amplitude or frequency is increased.

CHAPTER 4: ELECTROSTATIC FORCE INDUCED ADHESION

*Published as “Yang, J., Wu, C.Y., Adams, M. DEM analysis of the effect of electrostatic interaction on particle mixing for carrier-based dry powder inhaler formulations. *Particuology*. 2015. DOI: 10.1016/j.partic.2014.12.007”.

Abstract

Particle interactions play a significant role in controlling the performance of dry powder inhalers (DPIs), which mainly arise through van der Waals potentials, electrostatic interactions, and capillary forces. Our aim is to investigate the influence of electrostatic charge on the performance of DPIs as a basis for improving the formulation of the particle ingredients. The mixing preparation process of carrier and active pharmaceutical ingredient (API) particles in a vibrating container is investigated using a discrete element method (DEM). The number of API particles attaching to the carrier particle (i.e., contact number) increases with increasing charge and decreases with increasing container size. The contact number decreases with increasing vibrational velocity amplitude and frequency. Moreover, a mechanism governed by the electrostatic force is proposed for the mixing process. This mechanism is different from that previously proposed for the mixing process governed by van der Waals forces, indicating that long-range and short-range adhesive forces can result in different mixing behaviours.

Keywords: electrostatic; particle mixing; dry powder inhaler; discrete element method.

4.1. Introduction

Drug delivery using dry powder inhalers (DPIs) has been shown to be increasingly efficient for treating pulmonary and respiratory diseases (Islam and Gladki, 2008; Newman and Busse, 2002; Smith and Parry-Billings, 2003). In order to be directly delivered to the lungs and respiratory tracts, the sizes of the active pharmaceutical ingredient (API) particles in DPIs are generally small (< 5 μm), resulting in strong cohesion and poor flowability (Pritchard, 2001). Hence, API particles are normally mixed with large carrier particles to improve the flowability and dispersion efficiency (Aulton and Taylor, 2001). The interactions between carrier and API particles, such as van der Waals potentials, electrostatic interactions, and capillary forces, are key factors that determine how the fine API particles adhere to and detach from the carrier particle. Therefore particle interactions are of significant importance in controlling the performance of DPIs (Hinds, 1999).

Because electrostatic charge can be generated when two different materials are brought into contact and then separated, it is common for particles to become charged in DPIs owing to the frequent number of contacts between carrier and API particles or particles and surfaces (Karner and Urbanetz, 2011). Recently the electrification phenomenon during powder mixing processes has drawn much attention (Karner and Urbanetz, 2012; Karner and Urbanetz, 2013; Zhu *et al.*, 2007b). It was shown that inhalation powders were charged because the frequent contact and high impact velocities, and the net charge was influenced

by factors such as the carrier particle size, the air flow rate, the API content, and the addition of carrier fines (Karner and Urbanetz, 2013).

When particles become charged, attractive or repulsive electrostatic interactions may change their dynamic behaviour. The effect of electrostatic charge on powder behaviour has also been widely investigated (Adi *et al.*, 2010; Nwose *et al.*, 2012; Pu *et al.*, 2009). Previous experimental results showed that blending of positively charged carrier particles and negatively charged API particles improves particle uniformity because of strengthened inter-particle adhesion (Pu *et al.*, 2009). Nwose *et al.* (2012) investigated the effects of electrostatic charge on the powder flow during die filling using DEM–CFD, and found that electrostatic charge hindered powder flow and induced a loose packing structure since the electrostatic attractive forces facilitate particle agglomeration. Adi *et al.* (2010) initially charged mannitol powder to varying magnitudes by tumbling inside containers of different materials and then examined the dispersion performance. They found that the initial charge from tumbling did not significantly affect the aerosolisation.

Mixing of carrier and API particles is a critical unit operation that controls DPI performance. The influence of mixing time (Le *et al.*, 2012; Selvam *et al.*, 2011), addition of fine excipient particles (Jones and Price, 2006; Zeng *et al.*, 1999), surface energy (Saleem *et al.*, 2008; Yang *et al.*, 2013b), and carrier and API contents (Dickhoff *et al.*, 2003; Yang *et al.*, 2013a) on the mixing process have been intensively investigated. However, the effects of the electrostatic charge on

the preparation of carrier-based DPI formulations is still not fully understood and needs further investigation, since electrostatic interactions have a considerable effect on powder behaviour. Therefore, in this study, we aim to explore the influence of the electrostatic forces on the mixing process of the carrier and API particles in a vibrating container using DEM. Attempts are also made to explore how different adhesive forces affect the mixing behaviour.

4.2. Model setup

4.2.1. DEM model

The translational and rotational motions of a particle are governed by Newton's second law:

$$m_i \frac{\mathrm{d}\mathbf{v}_i}{\mathrm{d}t} = \mathbf{f}_{ci} + \mathbf{f}_{ei} + m_i \mathbf{g} \tag{4.1}$$

$$I_i \frac{\mathrm{d}\boldsymbol{\omega}_i}{\mathrm{d}t} = \mathbf{T}_i \tag{4.2}$$

where m_i, I_i, $\mathbf{v}_i$, $\boldsymbol{\omega}_i$ are the mass, moment of inertia, and translational and rotational velocities of particle i, respectively. $\mathbf{f}_{ci}$, $\mathbf{f}_{ei}$, and $\mathbf{T}_i$ are the contact force, electrostatic force, and torque acting on the particle, respectively. $\mathbf{g}$ is the gravitational acceleration.

For elastic spheres considered in this study, the contact force, $\mathbf{f}_{ci}$, is modelled using the theories of Hertz (1882) and of Mindlin and Deresiewicz (1953) for the normal and tangential directions, respectively (Kafui *et al.*, 2002). To account for van der Waals interactions in some simulations, the model developed by Thornton and Yin (1991) was employed to calculate the contact force, $\mathbf{f}_{ci}$, in which particle adhesion is modelled by JKR theory (Johnson *et al.*, 1971) such that the "pull-off" force, F_c, is defined as:

$$F_c = \frac{3}{2}\Gamma\pi R^* \tag{4.3}$$

where Γ is the thermodynamic work of adhesion and R^* is the effective radius, $R^* = r_1 r_2 / (r_1 + r_2)$, where r_i are the radii of two particles, 1 and 2.

The model developed by Pei *et al.* (2010) is employed to model the electrostatic force between particles, $\mathbf{f}_{ei}$. In this model, a cut-off distance is introduced and the electrostatic force is considered only when the distance between the particles is smaller than the cut-off distance; otherwise it is neglected. Coulomb's law (Seville *et al.*, 1997) is employed to model the electrostatic force between particles as follows:

$$\mathbf{f}_{21} = \frac{1}{4\pi\varepsilon_0\varepsilon_r}\frac{q_1 q_2}{r_{21}^2}\hat{\mathbf{r}}_{21} \tag{4.4}$$

where $\mathbf{f}_{21}$ and $\hat{\mathbf{r}}_{21}$ are the electrostatic force and unit vector from particle 2 to 1, respectively. ε_0 and ε_r are the permittivity of free space and the relative permittivity of the medium in the vicinity of the particles, q_1 and q_2 are the charges on the two particles, and r_{21} is the distance between the two particles.

4.2.2. Model formulation

Initially, a carrier particle with a radius of R is generated at the centre of a cubic container with sides of length l while a number of API particles with a radius of r are randomly generated in the empty space of the container. The carrier particle is positively charged while the API particles are negatively charged. The charge of the carrier particle is q, and the charge for each single API particle is $-q/N$ (N is the number of API particles), so that the whole system is neutral. It is assumed that the charges on the particles cannot transfer so the charge of each particle is fixed. The cut-off distance is set as 10*R*, which is large enough to accurately account for the long-range interactions while allowing for relatively efficient computation (Nwose *et al.*, 2012). After generating the particles, they are mixed by vibrating the container with a periodic velocity defined by the following expression:

$$V = V_0 \sin(2\pi f t) \tag{4.5}$$

where V_0 is the amplitude, f is frequency, and t is time. For the case in which V_0 = 0.04 m/s and f = 60 Hz, the displacement of the container in a vibration cycle is 2.1 mm. Since the size of the API particle is very small, Brownian motion may be in effect and air-particle interactions may affect the mixing behaviour. As a first step to explore the effect of electrostatic force on particle mixing, no air-particle interaction is considered in the present study. Further study using DEM coupled with computational fluid dynamics (CFD) and the immersed boundary method (Guo *et al.*, 2013) could be performed to explore this effect in applications with large particle size ratios. No electrostatic interaction between a wall and a particle is considered. The time step is 4.5×10^{-10} s. A viscous damping is introduced to consider the energy dissipation in the system. The simulation parameters are given in Table 1. It is assumed that the carrier and API particles are of the same material in this study. The material property parameters, which are also used in our previous work (Yang *et al.*, 2013b), are identical to those used in the work of Thornton and Yin (1991) while the Young's modulus of *α*-lactose monohydrate (Alderborn and Nystrom, 1996) is used. It should also be noted that only the adhesion between carrier and API particles is considered, but the cohesion among API particles is ignored. It is believed that the interactions between the carrier and API particles are dominated in current cases. In the following section, the contact number, defined as the number of API particles attaching to the carrier particle, is used to quantify the mixing behaviour.

Table 4.1. Simulation parameters.

Parameter	Value
Density (kg/m^3)	2650
Young's modulus (GPa)	24
Poisson's ratio	0.3
Coefficient of friction	0.3
R (μm)	35
r (μm)	2.5
l (μm)	105
N	200
q (nC)	0.014–0.14
V_0 (m/s)	0.02–0.06
f (Hz)	30–120

4.3. Results and discussion

Fig. 4.1 shows typical snapshots of the mixing process. After generation of the carrier particle and the API particles in the container (Fig. 4.1(a)), electrostatic forces attract the API particles towards the carrier particle (Fig. 4.1(b)) during the vibration process, and the number of API particles attached to the carrier particle increases with time (Fig. 4.1(c)) until the displacement direction of the container changes. When the container starts to move downward, the carrier particle impacts the top wall. This impact initially causes API particles to detach from the carrier particle (Fig. 4.1(d)). Then the API particles are again attracted to the carrier particle under the influence of the electrostatic force. When the first vibration cycle ends, impact between the carrier particle and the bottom wall causes API particles to detach again (Fig. 4.1(e)). Thereafter, the second vibration cycle starts and API particles form a layer on the carrier particle until the carrier particle impacts with the top wall of the container again (Fig. 4.1(f)).

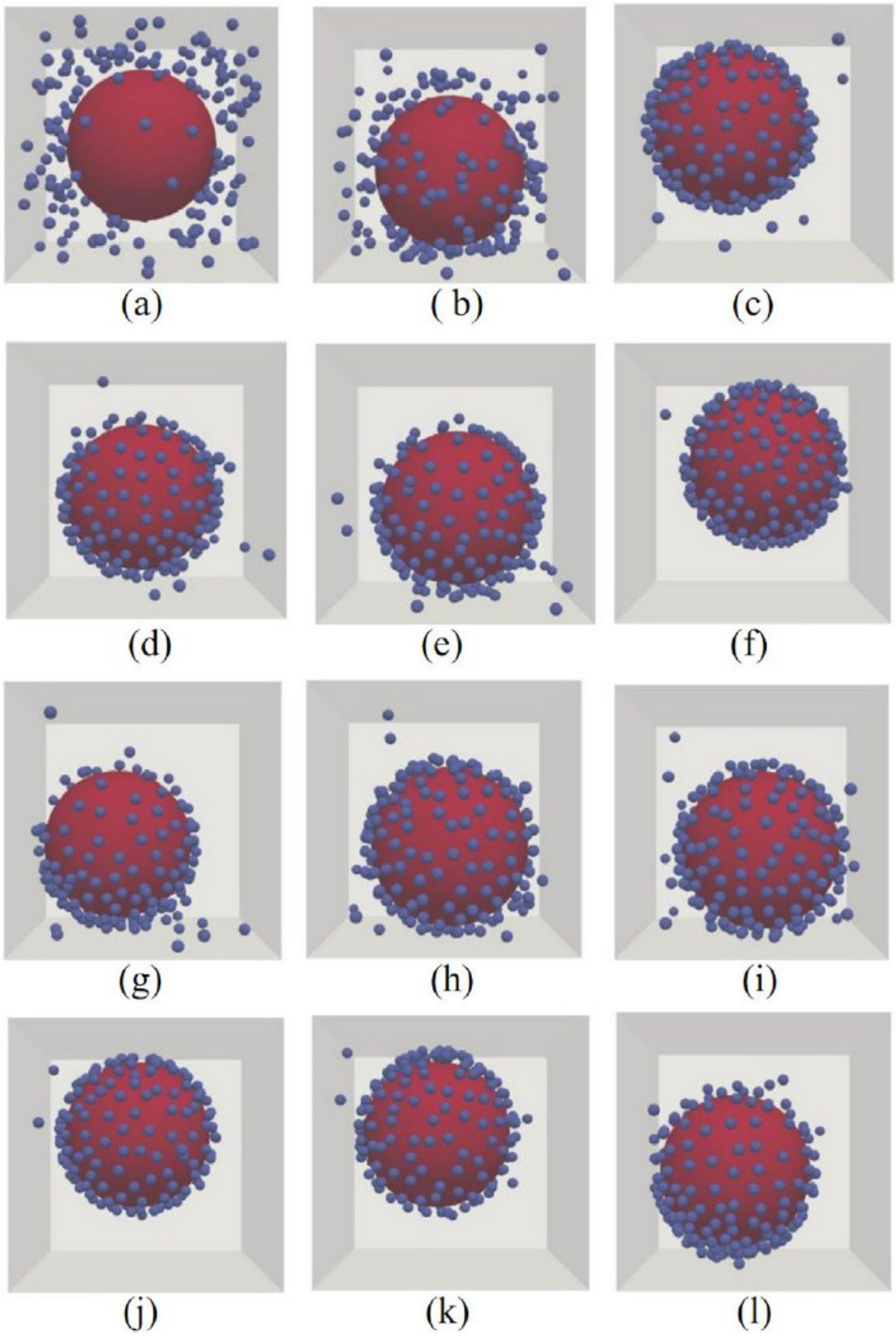

Fig. 4.1. Typical snapshots of the mixing process for the transition ((a)–(f)) and steady ((g) –(l)) states (q = 0.042 nC, V_0 = 0.04 m/s, f = 60 Hz).

At the steady state, during one vibration cycle, the API particles start to attach to the carrier particle when the container begins to move upward (Fig. 4.1(g)). The number of API particles attaching to the carrier particle generally increases but some fluctuations can also be found due to impacts between the carrier particle and the lower wall of the container (Fig. 4.1(h) & 1(i)). These impacts are not strong as both the container and the carrier particle move upward; therefore the fluctuations are not significant. An increased number of API particles are in contact with the carrier particle until the container starts to move downward (Fig. 4.1(j)). Since the carrier particle is still moving upward, a strong impact between the container top wall and the carrier particle causes a large amount of API particles to detach (Fig. 4.1(k)). Thereafter the carrier particle oscillates in the container, which further causes more API particles to detach until the beginning of the next vibration cycle (Fig. 4.1(l)).

The evolution of the contact number with time is shown in Fig. 4.2, which is labelled with letters that correspond with the time of the snapshots shown in Fig. 4.1. The contact number initially increases and then oscillates periodically. This periodicity arises from impacts between the carrier particle and the container walls and the attractive electrostatic force between the carrier particle and the API particles, such that the contact number increases and decreases in each cycle. Results from the time period highlighted in the rectangular box shown in Fig. 4.2 are further analysed to obtain the mean and standard deviation of the contact number, which will be discussed in the following sections.

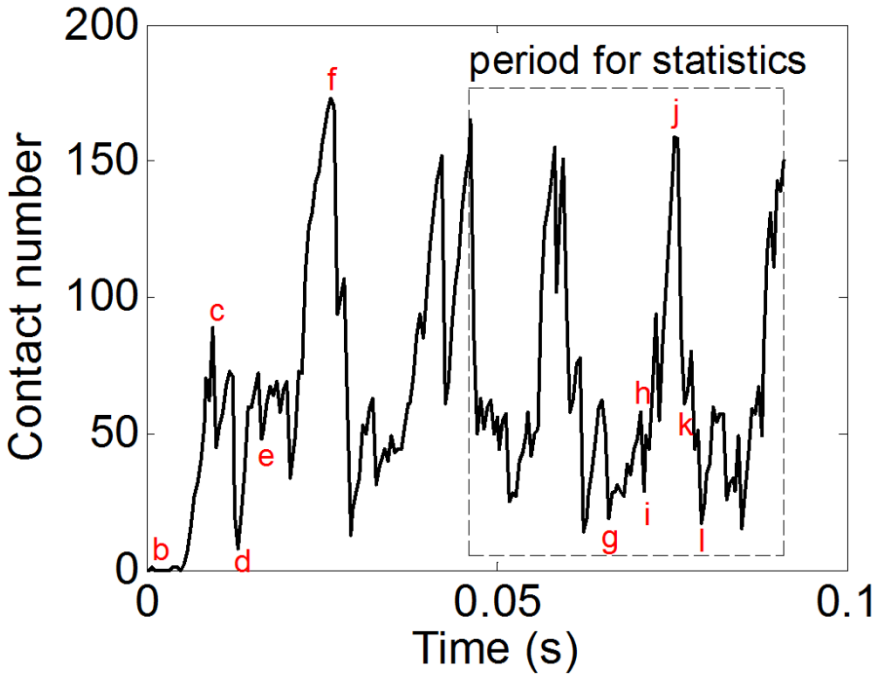

Fig. 4.2. Evolution of the contact number with time (q = 0.042 nC, V_0 = 0.04 m/s, f = 60 Hz).

The mean contact number decreases with increasing amplitude of the vibrational velocity, as shown in Fig. 4.3, because the increased impact energy causes more particles to detach from the carrier particle. It is worth noting that vibrations with large amplitudes also result in more API particles impacting the carrier particle. However, whether the API particles attach to the carrier particle is determined by the electrostatic attractive force, which acts even when there is no direct contact. Therefore, changing the vibrational amplitude only affects detachment of the API particles, but not the attachment itself.

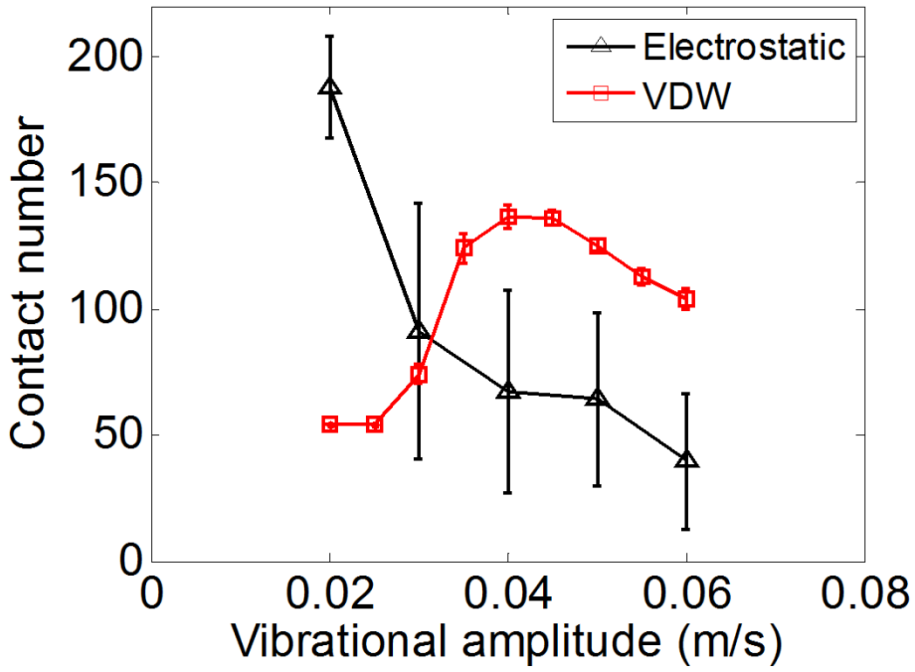

Fig. 4.3. Effect of the vibrational amplitude on the contact number during the mixing process (f = 60 Hz, electrostatic: q = 0.042 nC, VDW: Γ = 0.006 J/m^2).

As seen in Fig. 4.4, the mean contact number decreases with increasing vibrational frequency. In addition to increasing the impact energy, increasing the vibrational frequency also reduces the cycle period time, which is inversely related to the vibrational frequency, and therefore reduces the time available for the API particles to attach to the carrier. Correspondingly, the mean contact number is smaller and impact with the container wall causes more API particles to detach. Therefore, fluctuations during the process decrease with increasing vibrational frequency. As mentioned previously, the electrostatic charge provides an attractive potential even when there is no direct contact. Therefore, the mean contact number is determined only by the removal force (caused by the impacts) and the attractive force (electrostatic force) and, as a result, decreases with increasing vibrational frequency.

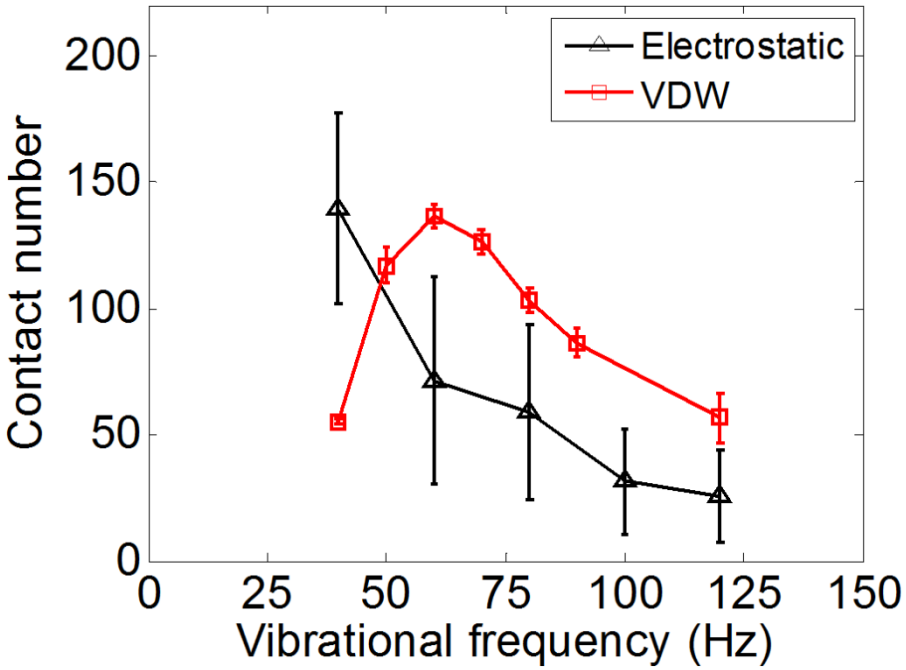

Fig. 4.4. Effect of the vibrational frequency on the contact number during the mixing process (V_0 = 0.04 m/s, electrostatic: q = 0.042 nC, VDW: Γ = 0.006 J/m^2).

In order to compare the influence of electrostatic forces on the mixing behaviour with van der Waals forces (implemented using JKR theory), our recently published results (Yang *et al.*, 2013b) are also superimposed in Figs. 4.3 and 4.4. It can be seen that in the case of the electrostatic forces, the mean contact number decreases with increasing amplitude and frequency while for van der Waals forces there exist an optimal amplitude and frequency corresponding to the maximum contact number. When only van der Waals forces act, high amplitudes and frequencies allow more opportunities for the API particles to impact with and attach to the carrier particle; at the same time, the higher energy of impact between the carrier particle and the container walls will cause more API particles to detach. That is to say, in the van der Waals regime, it is a competitive process. For the electrostatic case, the higher the amplitude and

frequency, the higher the impact energy will be. However, vibration does not affect the electrostatic force in the current case as the particles are pre-charged with fixed charges. The adhesive forces acts only when two particles are in contact (short range) for cases in which van der Waals forces are considered through the model proposed by Thornton and Yin (1991), while for cases incorporating the electrostatic force, adhesive force always exists (long range). Therefore, there is an optimal amplitude and frequency for cases with van der Waals forces, while the mean contact number decreases with both amplitude and frequency for cases with electrostatic forces.

A mechanism for the mixing process governed by the short-range adhesive forces was previously proposed as (Yang *et al.*, 2013b):

$$\Delta N_c = N_i \eta_s - N_d \tag{4.6}$$

where ΔN_c is the incremental contact number during the mixing process, N_i is the total impact number during the process, η_s is the sticking efficiency that indicates the percentage of API particles adhering to the carrier particle after an impact, and N_d is the total detachment number (the number of API particles that were originally adhered to the carrier particle but detached because of impact between the carrier particle and container wall or other removal forces). It is clear that the incremental contact number depends on the impact number. Accordingly, a mechanism for the long-range adhesive force is also proposed as:

$$\Delta N_c = N_f \eta_s - N_d \tag{4.7}$$

where N_f is the number of the API particles that are not in contact with the carrier particle. The difference between the two mechanisms is that the incremental contact number in the current case is not related to the impact number and that all API particles that are not in contact with the carrier particle have the potential to attach to the carrier particle because of long-range electrostatic interactions. This is because long-range adhesive forces always act between particles while short-range adhesive forces only act between particles that are in contact.

As shown in Eq. (4.4), the charge on the particles and the distance between them are two primary factors that determine the magnitude of the electrostatic force and the sticking efficiency, η_s, in Eq. (4.7). Because the size of the container can be related to the distance between particles, the influences of container size and the charge of the carrier and API particles on the mixing behaviour are also explored.

Fig. 4.5 illustrates the effects of container size and carrier particle charge on the mixing behaviour. The container size is increased from a factor of three times the radius of the carrier particle to a factor of six. The trends in the mean contact number as a function of carrier charge for different container sizes are similar. However, the magnitude of the mean contact number decreases with increasing container size. This is because for a larger container, there is a larger volume

within which the API particles reside, and the mean distance between the carrier particle and API particles is larger, which results in smaller electrostatic adhesive interactions and smaller contact numbers.

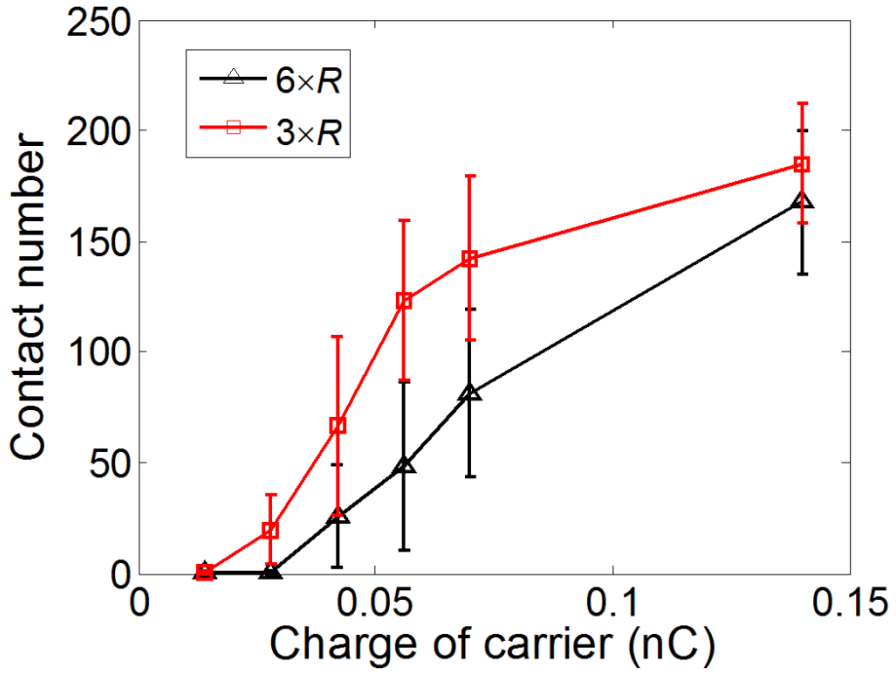

Fig. 4.5. Effects of the container size (expressed in terms of carrier particle radius *R*) and carrier particle charge on the contact number during the mixing process (V_0 = 0.04 m/s, f = 60 Hz).

The mean contact number increases with increasing charge because the attractive force between the carrier and the API particles scales directly with the charge. Moreover, the fluctuation of the mean contact number during the process first increases and then decreases with increasing particle charge. This is because most of the API particles with a higher charge attach to the carrier particle (i.e., high mean contact number) while those with a lower charge cannot attach to the carrier particle (i.e., small mean contact number). API particles with intermediate charge may attach to the carrier particle; however, the attractive

forces between them are not sufficiently strong to maintain their contact after an impact between the carrier particle and the container walls. Therefore, API particles attach to and then detach from the carrier particle, resulting in larger fluctuations in the mean contact number.

The effect of the charge distribution of the API particles on the mixing performance is shown in Fig. 4.6. Two charge distributions are examined: (1) the API particles are pre-charged uniformly and (2) the particles have random charges that follow a normal distribution:

$$f(q_{API}) = \frac{1}{\sigma\sqrt{2\pi}} e^{-\frac{(q_{API}-\mu)^2}{2\sigma^2}} \tag{4.8}$$

where q_{API} is the charge of the API particle, $\mu = -q/N$, and $\sigma = 0.1\mu$. q and N are the charge of the carrier particle and the number of API particles, respectively, as described in Section 4.2.2. It can be seen from Fig. 4.6 that the mixing performance of the different charge distributions are the same. This is because changing the charge on the API particle has little effect on the electrostatic adhesive force between the carrier and API particles as the charge of the carrier particle is about N times larger than that of the API particle. This indicates that the charge of the carrier particle dominates the electrostatic interactions between the carrier and API particles.

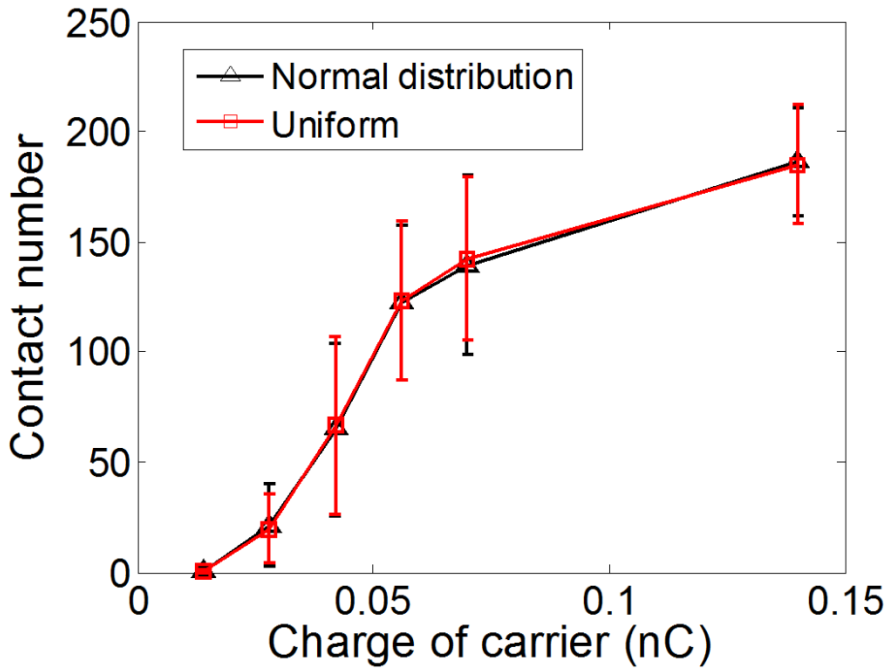

Fig. 4.6. Effect of the API particle charge distribution on the contact number during the mixing process (V_0 = 0.04 m/s, f = 60 Hz).

The mixing homogeneity for cases considering van der Waals forces and electrostatic forces is examined in Fig. 4.7. The surface of the carrier particle is divided into 12 sub-regions with an equal polar angle of 30° in the spherical coordinate system. The mean contact number for the period shown in the rectangle in Fig. 4.2 is then assigned to each of the twelve sub-regions. The mean contact number of each sub-region is normalized by the total mean contact number of the carrier particle. The homogeneity of mixing is quantified by the deviation of the normalized mean contact number of each sub-region. That is, the greater the deviation, the less homogeneous is the mixing. It can be seen from Fig. 4.7(a) that for electrostatic cases, the homogeneity value is stable except for when the vibrational amplitude is small, which corresponds to a large total mean contact number (Fig. 4.3). However, the homogeneity for cases with

van der Waals forces generally decreases as vibrational amplitude increases. This is a consequence of the container vibrating the API particles more strongly, which leads to more API particles impacting the carrier particle in all directions, which results in a more homogeneous mixing. A similar trend is also found in Fig. 4.7(b). Therefore, the mixing homogeneity in electrostatic cases is better than in the van der Waals cases when the vibrational amplitude and frequency are small, while the mixing homogeneity for the van der Waals cases are superior when the vibrational amplitude and frequency are high.

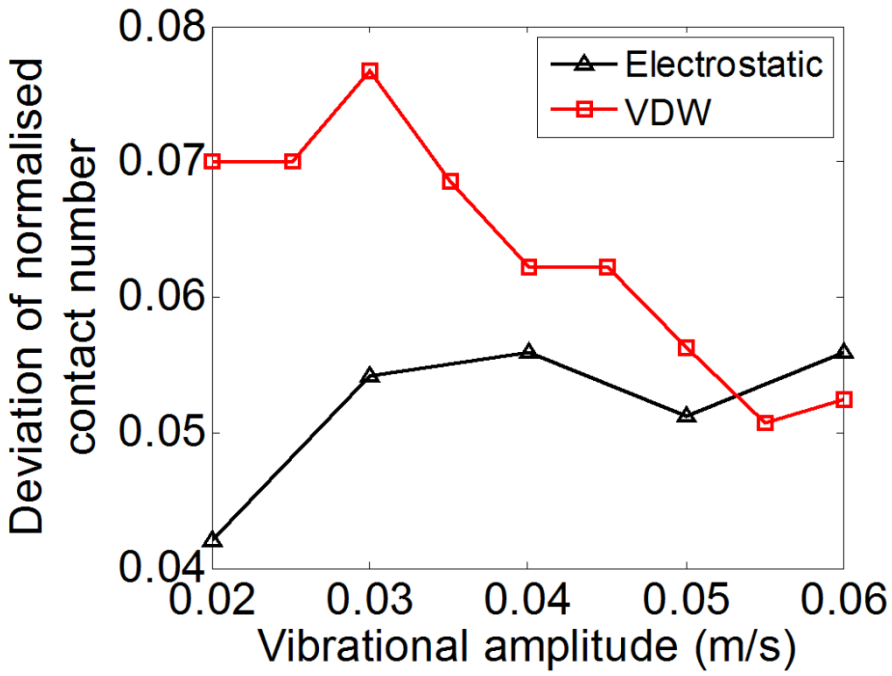

(a)

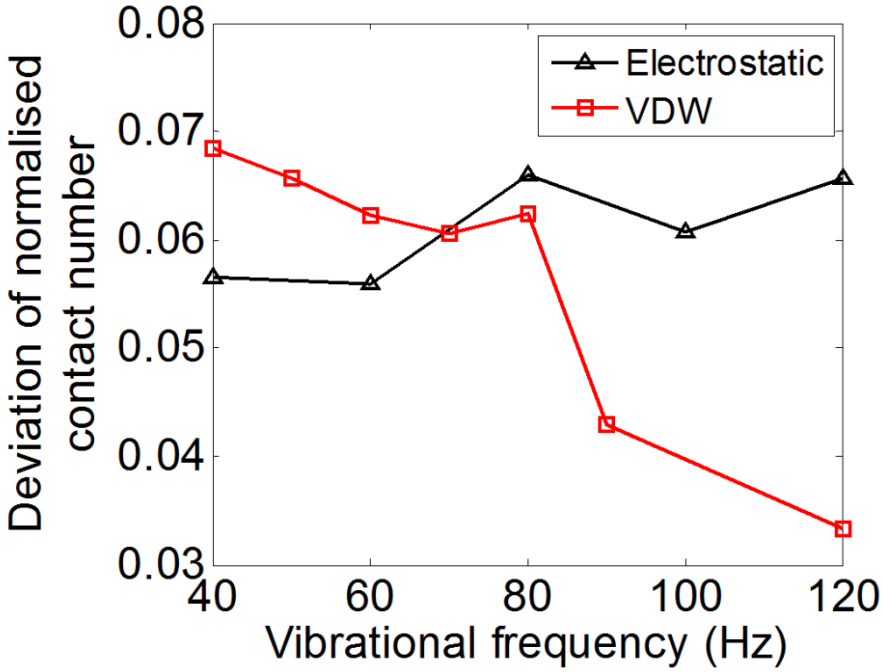

(b)

Fig. 4.7. Comparison of mixing homogeneity for electrostatic and VDW cases (a) f = 60 Hz and (b) V_0 = 0.04 m/s (electrostatic: q = 0.042 nC,VDW: Γ = 0.006 J/m^2).

4.4. Conclusions

The DEM is employed to investigate the effect of electrostatic force on a DPI formulation preparation process in which a pre-charged carrier particle and API particles are mixed in a vibrating container. It is shown that the mean contact number increases with increasing carrier charge and decreases with increasing vibrational velocity amplitude and frequency. The charge of the API particle plays an insignificant role in the electrostatic interactions between carrier and API particles. The contact number decreases with increasing container size. Comparison of the influence of electrostatic forces and that of van der Waals forces on the mixing process shows that the difference between these long- and

short-range adhesive forces results in the different mixing mechanisms. A mechanism is proposed for describing the mixing process governed by long-range adhesive forces.

CHAPTER 5: AIR FLOW INDUCED DISPERSION

*Published as “Yang, J., Wu, C.Y., Adams, M. Three-dimensional DEM-CFD analysis of air flow induced detachment of API particles from carrier particles in dry powder inhalers. *Acta Pharmaceutica Sinica B*, 2014, 4, (1) 52-59”.

Abstract

Air flow and particle-particle/wall impacts are considered as two primary dispersion mechanisms for dry powder inhalers (DPIs). Hence, an understanding of these mechanisms is critical for the development of DPIs. In this study, a coupled DEM-CFD (Discrete Element Method-Computational Fluid Dynamics) is employed to investigate the influence of air flow on the dispersion performance of the carrier-based DPI formulations. A carrier-based agglomerate is initially formed and then dispersed in a uniformed air flow. It is found that air flow can drag API particles away from the carrier and those in the downstream air flow regions are prone to be dispersed. Furthermore, the influence of the air velocity and work of adhesion are also examined. It is shown that the dispersion number (i.e. the number of API particles detached from the carrier) increases with increasing air velocity, and decreases with increasing the work of adhesion, indicating that the DPI performance is controlled by the balance of the removal and adhesive forces. It is also shown that the cumulative Weibull distribution function can be used to describe the DPI performance, which is governed by the ratio of the fluid drag force to the pull-off force.

Keywords: dry powder inhaler; dispersion; detachment; air flow; DEM-CFD.

5.1. Introduction

Using dry powder inhalers (DPIs), active pharmaceutical ingredient (API) particles with diameters of *ca.* 5 μm can be directly delivered to the lung or respiratory tracts (Islam and Gladki, 2008; Smith and Parry-Billings, 2003). However, the flowability of fine API particles is poor due to strong particle adhesion (Pritchard, 2001). Therefore, API particles need to be either agglomerated to large granules that are subsequently de-agglomerated, or "carried" by other large particles then detached from the carrier particles, during the inhalation process (Aulton and Taylor, 2001). Due to the complicated nature of the process, the efficiency of current DPIs is low (i.e. fine particle fraction (FPF) is normally less than 30% (Smith and Parry-Billings, 2003)). Generally, DPI performance is determined by the design of the device, the formulation, and the patients' respiration manoeuvre (Aulton and Taylor, 2001); a number of studies have recently been performed to investigate the dependency of DPI performance on these factors (Newman and Busse, 2002; Wong *et al.*, 2012). Both numerical and experimental approaches were employed to investigate the influence of air flow (Coates *et al.*, 2005a), grid structure (Coates *et al.*, 2006), mouthpiece length (Coates *et al.*, 2006), mouthpiece geometry (Coates *et al.*, 2007), and the air inlet size (Coates *et al.*, 2006). The influence of formulation properties on DPI performance, such as particle size (Kaialy *et al.*, 2012a), particle concentration (Young *et al.*, 2005), particle morphology (Kaialy *et al.*, 2011), particle surface roughness (Young *et al.*, 2008), density and porosity (Kaialy and Nokhodchi, 2012) and crystal form (Shur *et al.*, 2012), have also been explored. The DEM or

DEM-CFD approach was also applied to investigate the effects of impacts among particles/agglomerates/walls (Ning *et al.*, 1997a), fluid flow (Calvert *et al.*, 2009), particle adhesion (Yang *et al.*, 2013b) and device design (Zhou *et al.*, 2013).

Despite the above work, inconsistent results still exist and the understanding of the dispersion process and relative importance of the contributory factors is still unclear. For example, it was reported that air flow can dominate the dispersion performance (Calvert *et al.*, 2011; De Boer *et al.*, 2004; Voss and Finlay, 2002) while particle-particle and particle-wall impacts were also found to play an important role in dispersion process of DPIs (Tong *et al.*, 2010; Wong *et al.*, 2010; Wong *et al.*, 2011).

Voss and Finlay (2002) developed a powder de-agglomeration device, which was designed to entrain a dose of powder into the air stream and expose the powder to either a controllable level of turbulence or a mesh; the aim was to explore the effects of turbulence and mechanical impaction on dry powder de-aggregation. They found that the extent of de-aggregation increased as the level of turbulence was increased. De Boer *et al.* (2004) investigated the rate at which API particles are detached from carrier particles in adhesive mixtures in an air classifier, and found that the rate increased with increasing flow rate and the dispersion time. Aerodynamic dispersion of loose aggregates in a uniform fluid flow was investigated using DEM-CFD by (Calvert *et al.*, 2011). They found that there was a threshold velocity above which dispersion occurred quickly and

approached equilibrium asymptotically. These work explored the influence of air flow on the DPI detachment process, however, they were generally concerning the overall behaviour of the DPIs and the mechanical analysis of dispersion behaviour of loose agglomerate (i.e. drug-only formulations). The investigation for carrier-based DPIs at the micro-mechanical level was barely reported.

On the other hand, the effect of particle-particle and particle-wall impact on the dispersion behaviour of DPIs was also explored. Wong *et al.* (2010) investigated the influence of turbulence on the break-up and aerosol performance of DPI formulations using a combination of computational fluid dynamics and standardized entrainment tubes. They argued that there was no correlation between the extent of the turbulence and aerosol performance and the impact dominated agglomerate break-up in the system considered. The influence of impact on DPI performance was further examined by Wong *et al.* (2011), who found that particle-wall impacts resulted in initial agglomerate fragmentation followed by re-entrainment in the airstream. Tong *et al.* (2010) applied a combined CFD and DEM approach and investigated powder dispersion. In their study, agglomerates of different particle sizes and poly-dispersities were dispersed in a cyclonic flow at different flow velocities. It was shown that the dispersion was governed by particle-wall impacts and particle-particle adhesion.

Nevertheless, it is still unclear whether the air flow plays a role in DPI dispersion and the mechanism for the detachment process needs further investigation. Therefore the objective of this study is to investigate the effects of air flow on the

detachment process for carrier-based DPIs. A coupled DEM-CFD is used to explore both gas-particle interactions and particle-particle adhesion. The effects of air velocity, work of adhesion, and initial positions of API particles are examined and a mechanism governing the detachment performance is proposed.

5.2. Numerical model

5.2.1. DEM-CFD model

The coupled DEM-CFD model developed by Kafui *et al.* (2002) is used in this study, in which particle adhesion is analysed using the JKR theory (Johnson *et al.*, 1971) that was implemented by Thornton and Yin (1991). The translational and rotational motions of a particle are governed by the Newton's second law:

$$m_i \frac{\mathrm{d}\mathbf{v}_i}{\mathrm{d}t} = \mathbf{f}_{ci} + \mathbf{f}_{api} + m_i \mathbf{g} \tag{5.1}$$

$$I_i \frac{\mathrm{d}\boldsymbol{\omega}_i}{\mathrm{d}t} = \mathbf{T}_i \tag{5.2}$$

where m_i , I_i , $\mathbf{v}_i$, $\boldsymbol{\omega}_i$ are the mass, moment of inertia, translational and rotational velocities of particle i , respectively. $\mathbf{f}_{ci}$, $\mathbf{f}_{api}$ and $\mathbf{T}_i$ are the particle-particle/wall contact force, air-particle interaction force and torque acting on the particle. $\mathbf{g}$ is the gravitational acceleration.

Since the sizes of API particles are small, particle adhesion becomes significant. According to JKR theory, for the adhesion between particles, a “pull-off” force is defined as:

$$F_c = \frac{3}{2}\Gamma \pi R^* \tag{5.3}$$

where Γ is the thermodynamic work of adhesion, and R^* is the effective radius, which are defined as:

$$\Gamma = \gamma_1 + \gamma_2 - \gamma_{12} \tag{5.4}$$

$$R^* = r_1 r_2 / (r_1 + r_2) \tag{5.5}$$

where γ_1 and γ_2 are the surface energies of particles 1 and 2, γ_{12} is the interface energy, r_1 and r_2 are the radius of the two particles.

The air-particle interaction force, according to Anderson and Jackson (1967b), can be obtained from:

$$\mathbf{f}_{api} = -v_{pi}\nabla p + v_{pi}\nabla \cdot \boldsymbol{\tau} + \varepsilon \mathbf{f}_{di} \tag{5.6}$$

where v_{pi} is the volume of particle i, and p, $\boldsymbol{\tau}$, ε, and $\mathbf{f}_{di}$ are local air pressure, viscous stress tensor, void fraction and drag force on particle i, respectively.

According to Di Felice's correlation (Di Felice, 1994), the drag force can be obtained by:

$$\mathbf{f}_{di} = \frac{1}{2} C_{Di} \rho_a \frac{\pi d_{pi}^2}{4} \varepsilon^2 |\mathbf{u} - \mathbf{v}_i| (\mathbf{u} - \mathbf{v}_i) \varepsilon^{-(\chi+1)} \tag{5.7}$$

where C_{Di} and d_{pi} are the fluid drag coefficient and the diameter of the particle i, and ρ_a and $\mathbf{u}$ are the density and the velocity of the air. The determination of C_{Di} and χ can be found in reference (Di felice, 1994).

The continuity and momentum equations for the fluid phase are given as:

$$\frac{\partial(\varepsilon \rho_a)}{\partial t} + \nabla \cdot (\varepsilon \rho_a \mathbf{u}) = 0 \tag{5.8}$$

$$\frac{\partial(\varepsilon \rho_a \mathbf{u})}{\partial t} + \nabla \cdot (\varepsilon \rho_a \mathbf{u}\mathbf{u}) = -\nabla p + \nabla \cdot \boldsymbol{\tau} - \mathbf{F}_{\mathbf{ap}} + \varepsilon \rho_a \mathbf{g} \tag{5.9}$$

where $\mathbf{F}_{\mathbf{ap}}$ is the air-particle interaction force per unit volume and can be obtained by:

$$\mathbf{F}_{\mathbf{ap}} = \left(\sum_{i=1}^{n_c} \mathbf{f}_{api} \right) / \Delta V_c \tag{5.10}$$

where n_c is the total number of particles in a fluid cell and ΔV_c is the volume of the fluid cell.

5.2.2. Model setup

Initially, a carrier particle with a radius *R* and 242 API particles with radii r randomly positioned around the carrier are generated (Fig. 5.1a). Then the API particles are set to move towards the centre of the carrier at a specified velocity until they attach to the carrier and reach a stable state (Fig. 5.1b). The work of adhesion between the carrier particle and API particles is initially set to a relatively high value during this attachment process. When all API particles are in contact with the carrier, the work of adhesion is gradually decreased to the required value that is used for the simulation at a very small decrement. Thereafter, an air flow with a specific velocity *V* is introduced from the bottom boundary. The gravity is also introduced. Consequently both the carrier particle and the API particles move with the air flow until they reach the top boundary. The fluid domain is 1260 μm long, 1260 μm wide and 2100 μm high. The lower boundary is set as the gas inlet velocity, and the upper boundary is set as a continuous outflow outlet while the other boundaries are set as non-slip impermeable walls. The fluid cell size is twice as larger as the size of the carrier. The particle and fluid properties used in the simulation are listed in Table 5.1. It is assumed that the carrier and API particles have the same material properties as that of α-lactose monohydrate (Alderborn and Nystrom, 1996). Due to the relatively small air flow rate in current cases, small works of adhesion are chosen, which are still comparable with the experimental results measured using AFM by Louey *et al.* (2001).

To quantify the detachment behaviour, a series of new parameters are introduced, including the contact number, N_c, dispersion number, N_d, retention ratio, ϕ, and dispersion ratio, Φ. The contact number N_c is defined as the number of API particles attaching to the carrier, while the dispersion number as the number of API particles detached from the carrier. The retention ratio ϕ is then defined as the ratio of the contact number, N_c, to the initial number of API particles, N:

$$\phi = N_c / N \tag{5.11}$$

The detachment ratio is defined as the ratio of the dispersion number, N_d, to the initial number of API particles, N:

$$\Phi = N_d / N \tag{5.12}$$

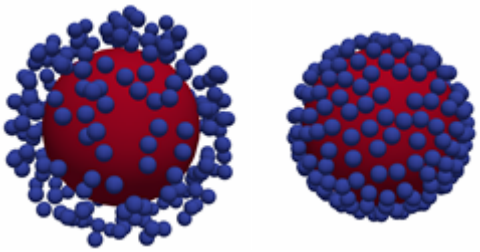

(a) (b)

Fig. 5.1. The agglomeration process: a) initial setup and b) prepared carrier-API agglomerate.

Table 5.1. Particle and fluid properties.

Parameter	Value
Radius of carrier (μm)	26.25-52.5
Radius of API (μm)	2.5
Density (kg/m^3)	2650
Young's modulus (GPa)	24
Poisson's ratio	0.3
Coefficient of friction	0.3
Thermodynamic work of adhesion (mJ/m^2)	0.1-0.6
Air velocity (m/s)	1.0-4.0
Air pressure (kPa)	101.325
Air density (kg/m^3)	1.2
Air viscosity (kg/m.s)	1.8×10^{-5}

5.3. Results and discussion

Fig. 5.2 shows a typical detachment process at different time instants. In Fig. 5.1b, API particles are randomly attached to the carrier surface before air flow is introduced. When the air flow is introduced, the API particles in the downstream regions are removed directly (Fig. 5.2a). Meanwhile, the API particles in the middle regions move (either slide or roll) around the carrier to the downstream regions and then detach from the carrier (Fig. 5.2b & 2c). Thereafter, most API particles are detached from the carrier while the API particles in the upstream regions are not removed and still in contact with the carrier (Fig. 5.2d).

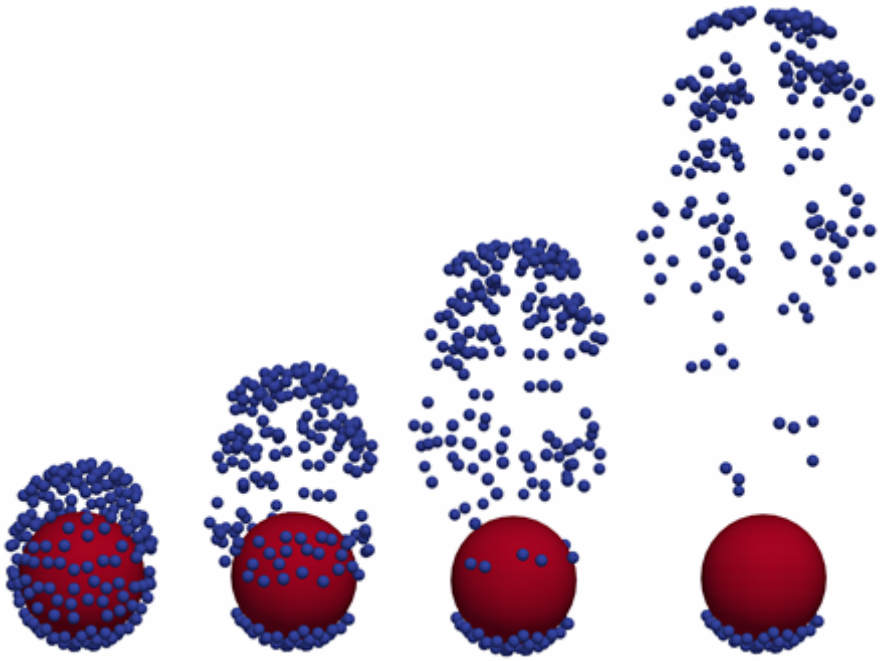

a) t = 4.55e-5 s b) t = 9.09e-5 s c) t = 1.36e-4 s d) t = 2.05e-04 s

Fig. 5.2. The detachment process at various time instants.

The evolution of the contact number with time at different air velocities is shown in Fig. 5.3, for which the carrier radius and the work of adhesion are set as 26.25 μm and 0.2 mJ/m^2, respectively. The time is normalized by the time of the dispersion process, which is the time period from the moment that gas is introduced to the moment that the agglomerate reaches the top boundary. It can be seen from Fig. 5.3 that the contact number decreases initially and then remains stable. It indicates that the air flow causes detachment of the API particles from the carrier as soon as it is introduced. This is attributed to the rapid acceleration of the agglomerate by the air flow. This dispersion mechanism was also reported by Gotoh *et al.* (2006), who analysed the forces acting on the agglomerate in a uniformed flow and suggested that rapid acceleration or deceleration was the dispersion mechanism. It is also clear that the contact

number decreases as the air velocity is increased, which suggests that an air flow with a large velocity, which causes large accelerations, can detach more particles from the carrier.

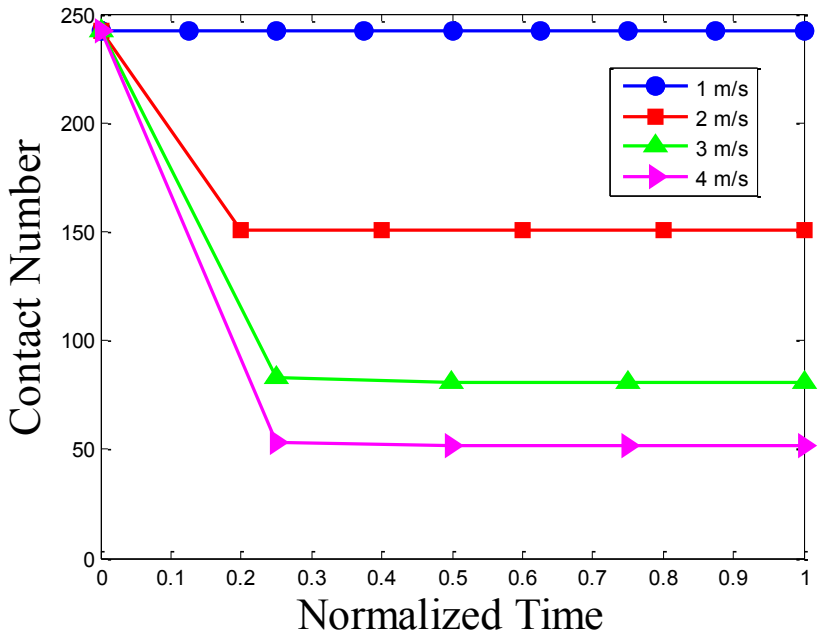

Fig. 5.3. The time evolution of contact number at different air velocities (R =26.25 μm, Γ =0.0002 J/m^2).

The effects of air velocity and work of adhesion on the dispersion ratio are shown in Fig. 5.4. The dispersion ratio increases with increasing air velocity, and decreases with increasing work of adhesion. This is consistent with the experimental observation of De Boer *et al.* (2004) who reported that the amount of API detached from the carrier increased with the flow rate. It is also found that for a smaller work of adhesion, the dispersion ratio can reach a stable state at a lower air velocity, while for a larger work of adhesion, there is a threshold air velocity above which air flow can cause the detachment of the API particles from

the carrier. This demonstrates that more API particles can be detached from the carrier by air flow at a higher velocity due to the larger fluid drag force. On the other hand, API particles with higher works of adhesion are more difficult to remove due to the strong inter-particle adhesion.

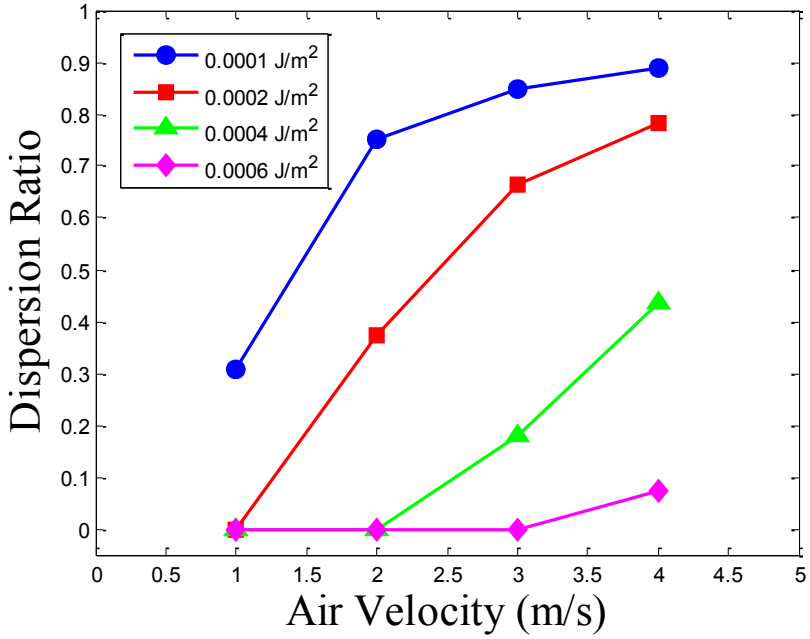

Fig. 5.4. The variation of the dispersion number with gas velocity for different works of adhesion (R =26.25 μm).

The distribution of contact normal orientations for the carrier particle is presented in Fig. 5.5, which shows the polar histogram (Zhang, 2003) of the proportion of contact normal orientations falling within a series of adjacent orientation classes that partition the full orientation space. The unit circle representing the $0-360^{\circ}$ full orientation space is partitioned into twelve bands in order to accommodate the contact normal orientations for the contacts between the carrier and API particles. Each contact is interrogated to identify its location in one of the twelve

bands. If a contact is located in band i, the total contact number for this band is increased by one. After all contacts have been scanned, the contact number of band i when the dispersion process is completed, n_i, and the original contact number of band i when the agglomerate is formed, N_i can be obtained. The radial coordinate of band i, r_i, is then determined as:

$$r_i = \frac{n_i}{N_i} \tag{5.13}$$

Referring to Eq. (5.11), r_i is equal to the retention ratio for band i.

It can be seen from Fig. 5.5a that the retention ratio in each band is equal to 1, indicating that no API particle detaches from the carrier when the air velocity is small. With an increase of the air velocity (Fig. 5.5b and Fig. 5.5c), the retention ratios in the downstream bands decrease, indicating that an increasing number of API particles detach from these regions. When the air velocity is high (Fig. 5.5d), the retention ratios in the downstream bands are equal to 0, corresponding to all the API particles in the downstream region being detached, and only the API particles in the upstream regions being still attached. That is, as the air velocity is increased, the retention ratios of the downstream regions decrease sharply while those in the upstream regions are stable. This phenomenon indicates that the API particles in the downstream regions are more likely to be removed by air flow. It could be a useful guide for engineered formulations that

would be based on locating the API particles in specific areas to improve of the overall efficiency of the DPIs.

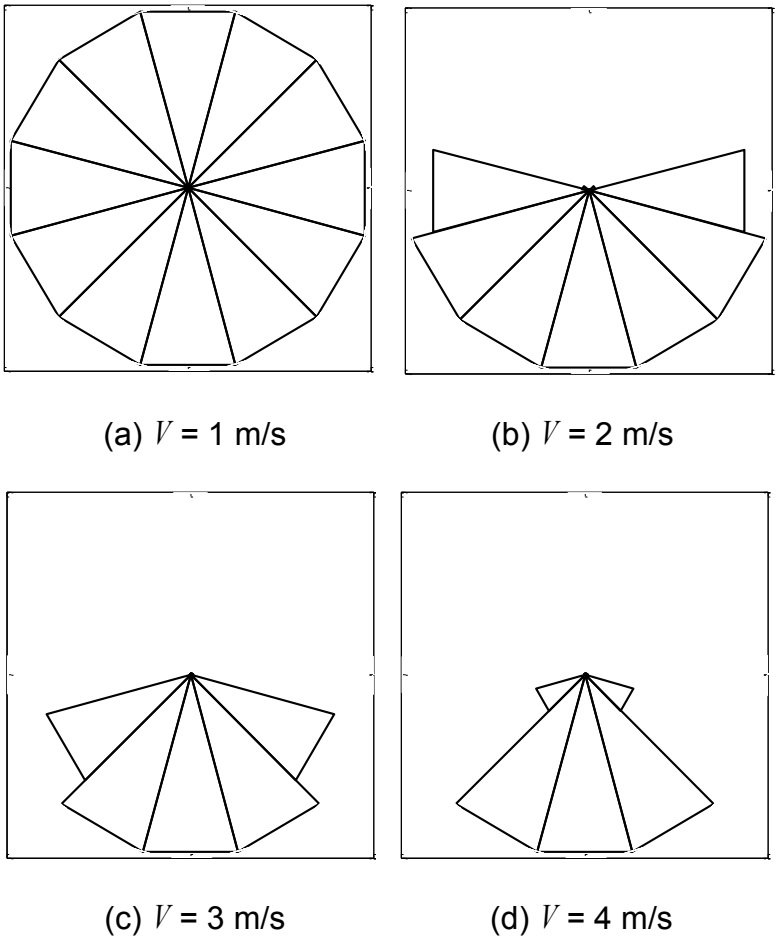

(a) V = 1 m/s (b) V = 2 m/s

(c) V = 3 m/s (d) V = 4 m/s

Fig. 5.5. Polar histograms of the contact orientations distribution (R =26.25 μm, Γ =0.0002 J/m^2).

A comparison of initial positions and detachment positions for API particles is shown in Fig. 5.6. The location of an API particle is quantified by the angle between the normal contact orientation and the vertical direction. The initial angle is that when the agglomerate is formed and the detachment angle is that when the API particle detaches. The initial and detachment angles of the detached particle are illustrated by hollow dots while those of attached particles

are plotted with solid triangles. It is clearly shown that, for the API particles in the downstream regions (i.e. regions with small initial angles), the initial and detachment positions are same, which suggests that the API particles can be directly removed by the air flow after it is introduced; for the API particles near the equator, the detachment angles are smaller than the initial angles, which suggests that the API particles first move around the carrier to the downstream region and then detach from the carrier; the API particles in the upstream regions cannot be removed.

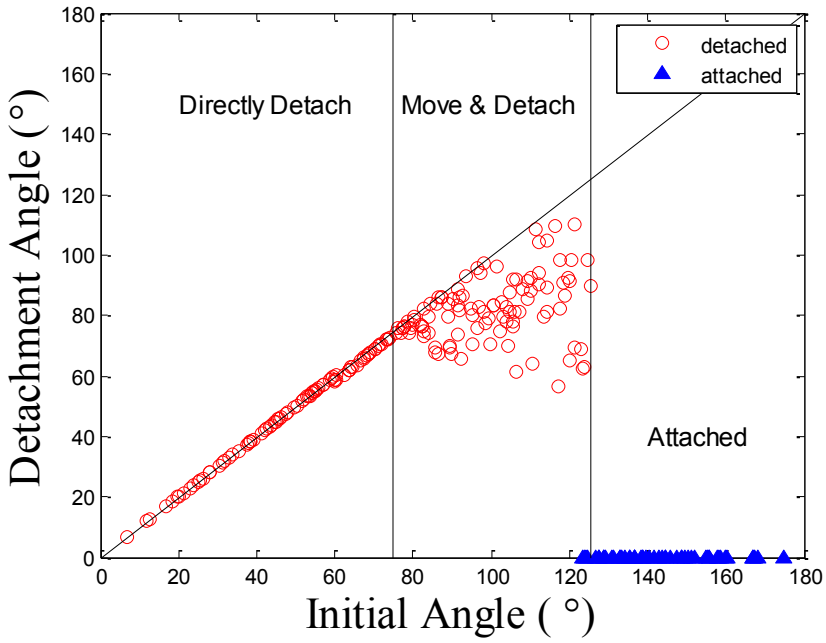

Fig. 5.6. The variation of detachment angle with initial angle (R =26.25 μm, Γ =0.0002 J/m^2, V =4.0 m/s).

The detachment process is governed by the removal force (e.g. fluid drag force) and the adhesive force (e.g. inter-particle force), and the dispersion performance is the result of the balance of these two forces. The variations of the dispersion

ratio, Φ, with the fluid drag force (eq. (5.7)) and the pull-off force (eq. (5.3)) are shown in Fig. 5.7a and Fig. 5.7b, respectively. For each carrier size, cases with four air velocities and four works of adhesion, as shown in Table 1, are systematically simulated. It can be seen from Fig. 5.7a that for a specific fluid drag force, the dispersion ratio varies as the works of adhesion are different, indicating that the detachment process is not governed by the fluid drag force only. In addition, the variation range of dispersion ratio increases with increasing drag force, suggesting that API particles are more easily removed by high speed flow. Similarly, it is clearly shown from Fig. 5.7b that for a specific pull-off force, the dispersion ratio varies with different air velocities. The variation range of the dispersion ratio decreases with increasing pull-off force, indicating that API particles are more difficult to be removed with strong adhesion. However, for either of the two figures, the data cannot superimpose into a master curve, which indicates that there is no direct correlation between the dispersion ratio and the removal force or the adhesive force.

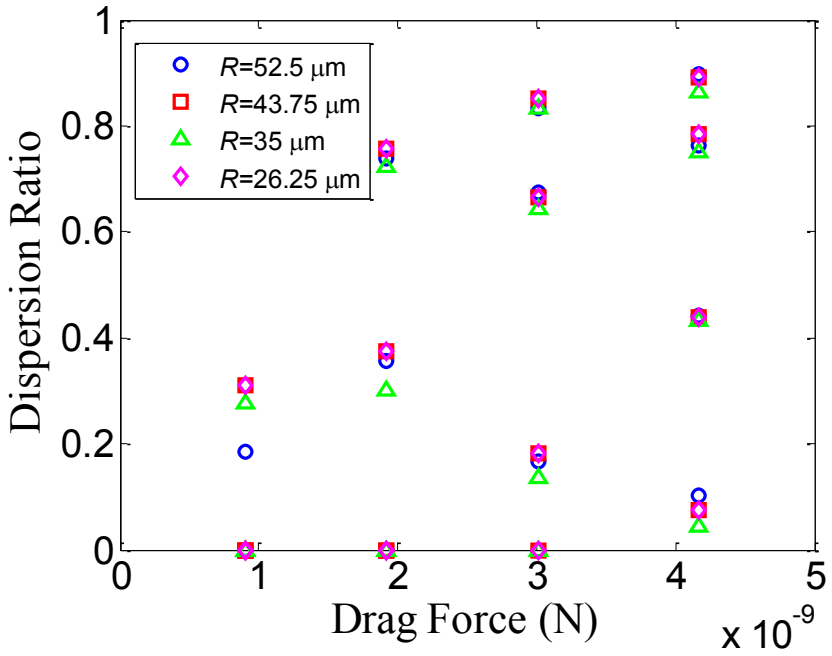

(a)

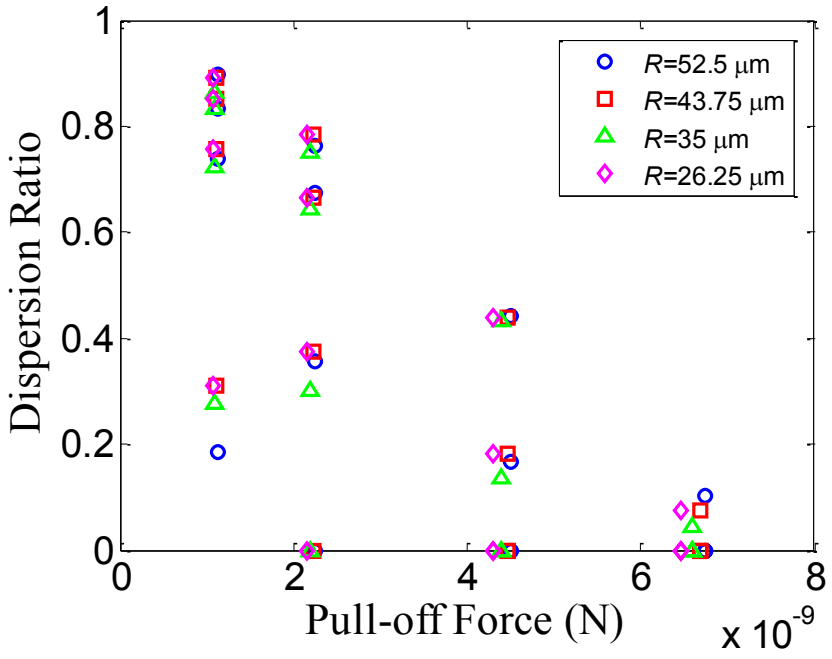

(b)

Fig. 5.7. The variation of the dispersion ratio with the fluid drag force and the pull-off force for a range of carrier radii.

Since the dispersion ratio, Φ, is a result of the balance of the removal and the adhesive forces, it is plotted as a function of the ratio of these two forces, $\eta = F_d / F_c$, as shown in Fig. 5.8. The data for all cases considered superimpose into a single master curve that can be described using the cumulative Weibull distribution function (Papoulis and Pillai, 2002):

$$\Phi = \begin{cases} 1 - \exp\left(-\left(\dfrac{\eta - \eta_0}{\lambda} \right)^{\kappa} \right), & \eta \geq \eta_0 \\ 0 \quad , & \eta < \eta_0 \end{cases} \tag{5.14}$$

The location parameter η_0 corresponds to the critical value above which API particles can be removed from the carrier. The scale parameter λ predicts the range over which the dispersion ratio increases from 0 to 1. The shape parameter κ characterises the rate of increase of the dispersion ratio. The values of these parameters are shown in Table 5.2. It can be seen from Fig. 5.8 that the dispersion ratio increases dramatically as soon as the force ratio is larger than the critical value and then asymptotically reaches 1.0 as the force ratio is further increased. Therefore, the dispersion performance can be described using Eq. (5.14) in the whole range in which the dispersion ratio changes between 0 and 1.

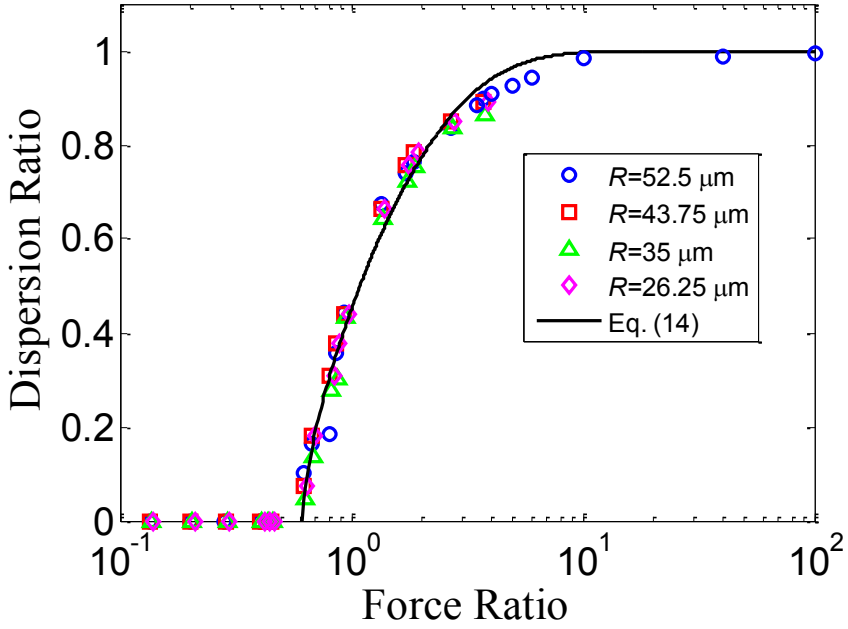

Fig. 5.8. The variation of dispersion ratio with the ratio of the fluid drag force to the pull-off force for carrier particles with a range of radii.

Table 5.2. Fitting parameters.

Parameter	Value
η_0	0.61
λ	0.80
κ	0.71

Fig. 5.9 illustrates the forces acting on the i th spherical API particle (eq. (5.1)), in which $\mathbf{f}_{ci\_n}$ and $\mathbf{f}_{ci\_t}$ are the normal and tangential components of the contact force $\mathbf{f}_{ci}$, respectively. Once the air flow is introduced, the air-particle interaction force $\mathbf{f}_{api}$ drags the API particle to a positive *y* position, since the component in the positive *y* direction of $\mathbf{f}_{api}$ is dominant. If the API particle is located in the

upstream hemisphere of the spherical carrier particle (i.e. $90^\circ \le \alpha \le 180^\circ$), the air-particle interaction force $\mathbf{f}_{api}$ actually compresses the API particle to the carrier. If the API particle is located in the downstream hemisphere (i.e. $0^\circ \le \alpha \le 90^\circ$), the air-particle interaction forces $\mathbf{f}_{api}$ actually pulls the API particle away from the carrier. When the normal component of the air-particle interaction force $\mathbf{f}_{api}$ is larger than the pull-off force F_c (eq. (5.3)), the API particle can be removed from the carrier. In addition, due to the effects of the tangential component of the air-particle interaction force $\mathbf{f}_{api}$ and the torque caused by the tangential component of the contact force, $\mathbf{f}_{ci\_t}$, the API particles located in the upstream hemisphere can move (either slide or roll) to the downstream hemisphere and then be removed from the carrier. This process is also clearly shown in the snapshots in Fig. 5.2. Therefore, the API particles in the downstream regions of the spherical carrier particle are more likely to be removed by air flow.

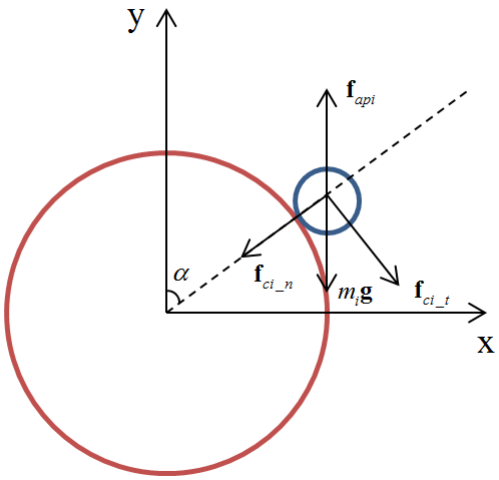

Fig. 5.9. The forces acting on the API particle.

It is worth noting that the air flow around the carrier and the air-particle interaction forces $\mathbf{f}_{api}$ for API particles are not necessarily identical. The air-particle interaction forces for API particles at different positions around the carrier are determined by the local air velocities. However, since the ratio of the size of carrier to that of APIs for carrier-based formulations is normally larger than 10, even up to 20, it is challenging to determine the localised air flow at the API size level using DEM-CFD, as the fluid cell size employed in DEM-CFD is relative large (i.e. > the carrier size). In the current DEM-CFD simulations, the fluid cell is twice greater than the size of the carrier. Therefore, the air velocity around the carrier is resolved with relatively coarse fluid grids and the air-particle interaction forces $\mathbf{f}_{api}$ for all the API particles in the same fluid cell are almost identical. Even though, the DEM-CFD with coarse fluid grids would offer a robust tool for exploring the dispersion behaviour of DPIs with a large number of carrier based agglomerates because of its high compute efficiency. Furthermore, a more accurate determination of $\mathbf{f}_{api}$ could be achieved by using the gradient interpolations proposed by (Wu *et al.*, 2006) to calculate the the Eulerian field quantities (e.g. fluid velocity, pressure and void fraction) at the particle centre in a fluid cell. Nevertheless, further investigation is needed to employ enhanced DEM-CFD methods, such as that with immersed boundary methods (Guo *et al.*, 2013), which enable a detailed analysis of gas-particle interactions using fine fluid cells, so that how significant the localised fluid flow on the dispersion behaviour of carrier based DPI formulations can be evaluated.

5.4. Conclusions

A coupled DEM-CFD with coarse fluid grids is applied to investigate the effect of air flow on the dispersion performance of carrier-based DPI formulations. A carrier-based agglomerate is initially formed and then dispersed in a uniformed air field. It is shown that air flow can detach the spherical API particles from the carrier after it is introduced. In addition, the particles in the downstream air flow regions are prone to be removed by the air flow.

The influence of air velocity and work of adhesion, which relate to the removal and adhesive forces, have also been examined. Since the dispersion ratio is governed by the ratio of the fluid drag force to the pull-off force, the current work suggests that DPI performance is the result of the balance of those two forces. It is also found that the cumulative Weibull distribution function (Eq. (5.14)) can well describe the dispersion performance of DPIs.

CHAPTER 6: PARTICLE-WALL IMPACT INDUCED DISPERSION

*Published as “Yang, J., Wu, C.Y., Adams, M. DEM analysis of the effect of particle-wall impact on the dispersion performance in carrier-based dry powder inhalers. *International Journal of Pharmaceutics*, 2015, 487, (1-2) 32-38”.

Abstract

The impact between particles or agglomerates and a device wall is considered as an important mechanism controlling the dispersion of active pharmaceutical ingredient (API) particles in dry powder inhalers (DPIs). In order to characterise the influencing factors and better understand the impact induced dispersion process for carrier-based DPIs, the impact behaviour between an agglomerate and a wall is systematically investigated using the discrete element method. In this study, a carrier-based agglomerate is initially formed and then allowed to impact with a target wall. The effects of impact velocity, impact angle and work of adhesion on the dispersion performance are analysed. It is shown that API particles in the near-wall regions are more likely to be dispersed due to the deceleration of the carrier particle resulted from the impact with the wall. It is also revealed that the dispersion ratio increases with increasing impact velocity and impact angle, indicating that the normal component of the impact velocity plays a dominant role on the dispersion. Furthermore, the impact induced dispersion performance for carrier-based DPI formulations can be well approximated using a cumulative Weibull distribution function that is governed by the ratio of impact energy and adhesion energy.

Keywords: impact; adhesion; dispersion; discrete element method; dry powder inhalation.

6.1. Introduction

Dry powder inhalers (DPIs) have become increasingly popular for treating pulmonary and respiratory diseases in recent years, due to their unique advantages compared with other drug delivery approaches (e.g. injection and oral administration), such as direct delivery of drugs to the target areas resulting in a rapid onset of activity and smaller doses; providing more drug choices especially for those poorly absorbed orally; and its environmentally friendly label (Aulton and Taylor, 2001; Frijlink and De Boer, 2004; Islam and Gladki, 2008; Newman and Busse, 2002). However, the dispersion efficiency of current DPIs is relatively low, i.e. normally fine particle fraction (FPF) < 30%, which requires considerable improvements for the further development of efficient DPIs (Smith and Parry-Billings, 2003).

DPI dispersion performance is mainly determined by three factors: device design, patients' inspiratory manoeuvre, and formulation design (Jones and Price, 2006). The patients' inspiratory manoeuvre is directly related to the air flow in the inhaler. It can also affect the impact of particles with the device wall because a high air velocity can result in a high impact velocity (Wong *et al.*, 2011). Some device designs, such as increasing the grid cross-sectional area, can increase the intensity of impact between the particle and the device wall; while other designs, such as decreasing the inlet size, can increase the air velocity and subsequently affect the impact behaviour (Zhou *et al.*, 2013). The characteristics of formulations, such as carrier size and carrier shape, also affect the dispersion

performance. It was reported that DPI performance improved with decreasing carrier particle size and particles with an elongated shape, more irregular shapes and rougher surfaces could deliver more API particles to lower airway regions (Kaialy *et al.*, 2012a; Kaialy *et al.*, 2012c).

It is well recognized that the dispersion process in DPIs is primarily governed by two mechanisms: i) air flow and ii) mechanical impact (De Boer *et al.*, 2003; Donovan *et al.*, 2012; Voss and Finlay, 2002). Voss and Finlay (2002) developed a powder de-agglomeration rig and investigated the effect of air flow on dry powder de-agglomeration and found that the rate of de-agglomeration was increased with increasing intensity of the turbulence. On the other hand, impact induced dispersion/de-agglomeration also drew much attention of researchers. Thornton and Liu (2004) investigated the impact of a cuboidal agglomerate with a wall and found that the fracture occurred as a result of strong force transmission into the agglomerate creating a heterogeneous velocity distribution. Ning *et al.* (1997a) simulated the particle/agglomerate-wall impact induced breakage of lactose agglomerate that consisted of 2000 primary particles within a diameter range of 9-11 μm. They found that the dynamic features and loading compliance of loose agglomerates were distinctly different from solid particles and strongly bonded agglomerates. More recently, Tong *et al.* (2009) used the discrete element method (DEM) to model the impact between a loose agglomerate of fine mannitol particles and a wall and found that agglomerate breakage was promoted with increasing impact velocity and an optimal breakage performance was obtained at an impact angle of 45°. These studies provided a

better understanding of the underlying mechanism of impact induced dispersion/de-agglomeration. However, they focused on the agglomerates made of particles of similar sizes, i.e. API particles only, and the study on the impact behaviour of carrier-based agglomerates is scarce.

Therefore, in this study, the impact of a carrier-based agglomerate with a wall at various impact velocities and angles is modelled using DEM, in which inter-particle adhesion is considered. The effects of work of adhesion, impact velocity and impact angle are investigated. In addition, a mechanism is proposed for predicting the impact induced dispersion performance of carrier-based DPIs.

6.2. Numerical model

6.2.1. DEM model

The DEM model is identical to the one used in the previous work (Yang *et al.*, 2013b) and summarised here. The translational and rotational motions of a particle are governed by the Newton's second law:

$$m_i \frac{\mathrm{d}\mathbf{v}_i}{\mathrm{d}t} = \mathbf{f}_{ci} + m_i \mathbf{g} \tag{6.1}$$

$$I_i \frac{\mathrm{d}\boldsymbol{\omega}_i}{\mathrm{d}t} = \mathbf{T}_i \tag{6.2}$$

where m_i , I_i , $\mathbf{v}_i$, $\boldsymbol{\omega}_i$ are the mass, moment of inertia, translational and rotational velocities of particle i, respectively. $\mathbf{f}_{ci}$ and $\mathbf{T}_i$ are the contact force and torque acting on the particle. $\mathbf{g}$ is the gravitational acceleration.

As the sizes of API particles used in DPIs are very small, they are very adhesive. Therefore, JKR theory (Johnson *et al.*, 1971) is applied to model the adhesion between particles and its implementation in DEM was detailed in (Thornton and Yin, 1991). The "pull-off" force, F_c, with which the two adhesive particles can be separated is given by:

$$F_c = \frac{3}{2}\Gamma\pi R^* \tag{6.3}$$

$$R^* = r_1 r_2 / (r_1 + r_2) \tag{6.4}$$

where Γ is the thermodynamic work of adhesion, and R^* is the effective radius. r_1 and r_2 are the radius of the particles 1 and 2, respectively.

6.2.2. Model setup

A carrier particle with a radius of r_c is initially generated. Then N monosized API particles with a radius of r_{API} are created around the carrier. The API particles are set to move towards the centre of the carrier at a very low velocity until they

are in contact with the carrier. The adhesion between the carrier and API particle is initially set as a relatively high value and is then decreased to the prescribed value. After the adhesion is changed to the required value, a number of simulation cycles are sequentially executed until the sum of the kinetic energies of carrier and API particles is smaller than a prescribed value to ensure that a stable agglomerate is formed. After the agglomeration process is finished, the carrier-based agglomerate impacts with a wall at a prescribed impact velocity V_i and an impact angle θ (Fig. 6.1). Six different velocities and four different angles are considered to examine their influence on the dispersion process. The effect of adhesion between the carrier and API particles is also investigated with various values of the thermodynamic work of adhesion. Since the primary aim of this study is to explore the influence of adhesive interactions between the carrier and API particles on the dispersion process at the microscopic level, only adhesion is considered. In the current DEM, particle-particle and particle-wall interactions are modelled using theoretical contact mechanics, in which physical properties such as Young's modulus, Poisson's ratio, particle density, coefficient of friction are the input parameters and the thermodynamic work of adhesion is chosen as a varying parameter for the sensitivity analysis. As a first approximation, the carrier and API particles are assumed to be spherical and of the same material, which is consistent with that used in our previous studies (Yang *et al.*, 2013b; Yang *et al.*, 2014; Yang *et al.*, 2015). Even so, it is believed that the present study will enhance our understanding of the underlying micromechanics of dispersion process in DPIs. The simulation parameters are given in Table. 6.1.

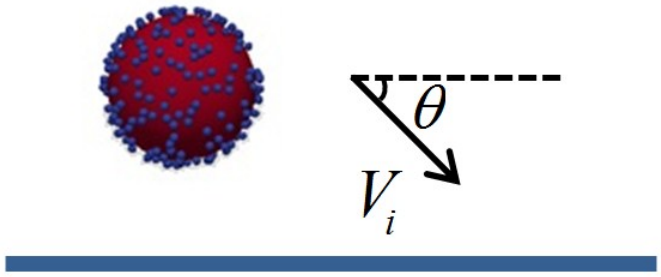

Fig. 6.1. An illustration of the impact of a carrier-based agglomerate with a wall.

Table 6.1. Simulation parameters.

Parameter	Value
Radius of carrier (μm)	43.75
Radius of API (μm)	2.5
Number of API particles	242
Density (kg/m^3)	2650
Young's modulus (GPa)	24
Poisson's ratio	0.3
Coefficient of friction	0.3
Thermodynamic work of adhesion (mJ/m^2)	0.1-0.6

6.3. Results and discussion

Fig. 6.2 shows a typical dispersion process of API particles during the impact of the carrier-based agglomerate and the wall. Once the agglomerate impacts with the wall, API particles in the lower hemisphere detach from the carrier due to the deceleration of the carrier (Fig. 6.2 a & b). During rebound, a few API particles in

the upper hemisphere move around the carrier and detach from the lower region of the carrier while others remain on the carrier (Fig. 6.2 c & d).

(a) (b) (c) (d)

Fig. 6.2. Snapshots of the impact process between the carrier-based agglomerate and the wall (V_i=100 mm/s, θ=45°, Γ=0.1 mJ/ m^2).

Fig 6.3 shows the variations of the contact number, i.e. the number of API particle sticking to the carrier, and the velocity of carrier particle with time during the impact. It can be seen that the contact number decreases drastically while the velocity of carrier increases. A coefficient of restitution e is defined as:

$$e = V_r / V_i \tag{6.5}$$

in which V_i and V_r are the impact velocity and rebounding velocity, respectively. From Fig. 6.3, the coefficient of restitution of the carrier is 0.997. This implies that very little kinetic energy of the carrier is dissipated during the impact process. The evolution of force on the wall and force on the carrier particle is shown in Fig. 6.4. It should be noted that the line for the force on the wall is reversed for better comparison. It can be seen that the force first increases and then decreases. The force on the carrier particle is essentially identical to (only a little smaller

than) that on the wall and the forces on the API particles can be ignored. This indicates that the carrier plays a dominated role in the impact process.

The evolution of the dispersion ratio (i.e. the ratio of the number of API particles detached from the carrier to the total number of API particles) with time is shown in Fig. 6.5. The dispersion process can be divided into two stages: i) the dispersion ratio drastically increases due to deceleration of the carrier particle caused by the impact between the wall and the agglomerate; ii) the dispersion ratio continues to increase but at a reduced rate during the rebound.

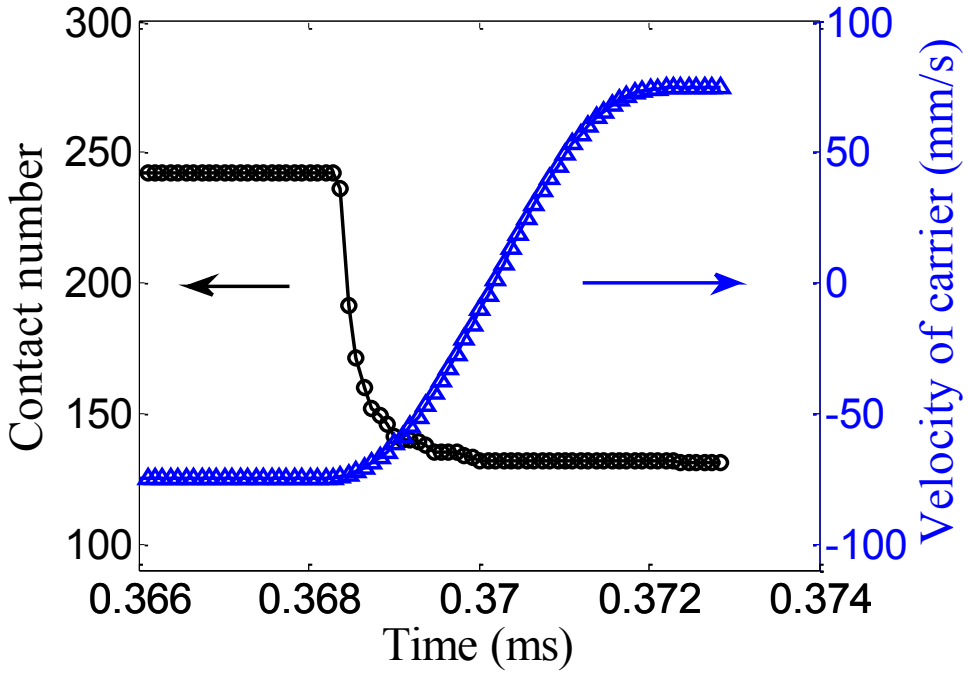

Fig. 6.3. The variations of the contact number and the velocity of carrier with time (V_i=75 mm/s, θ=90°, Γ=0.1 mJ/ m^2).

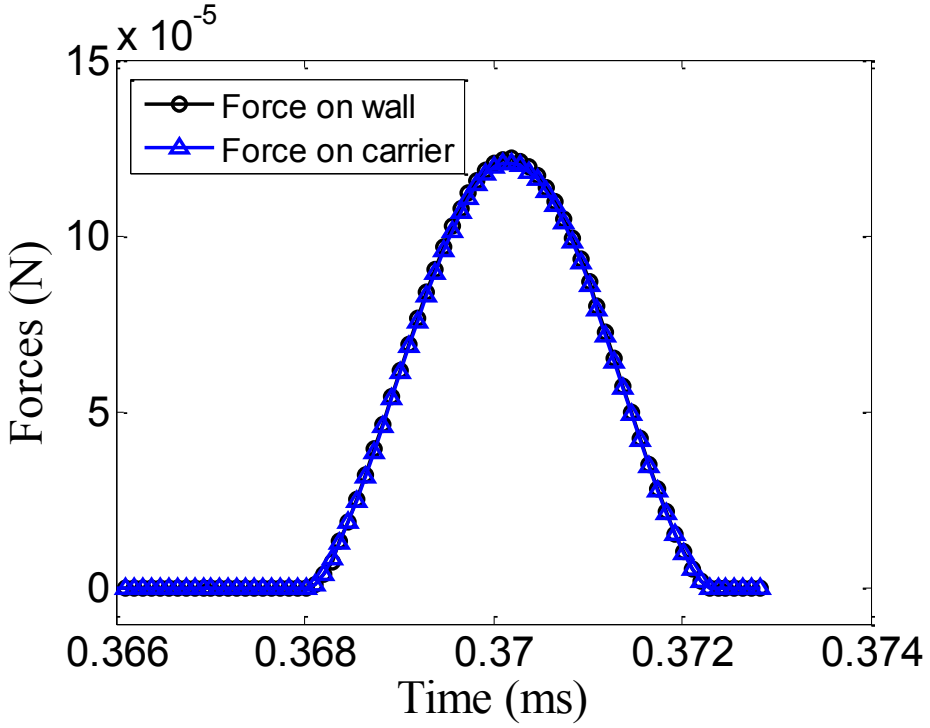

Fig. 6.4. The evolution of force on the wall and force on the carrier (V_i=75 mm/s, θ=90°, Γ=0.1 mJ/ m^2).

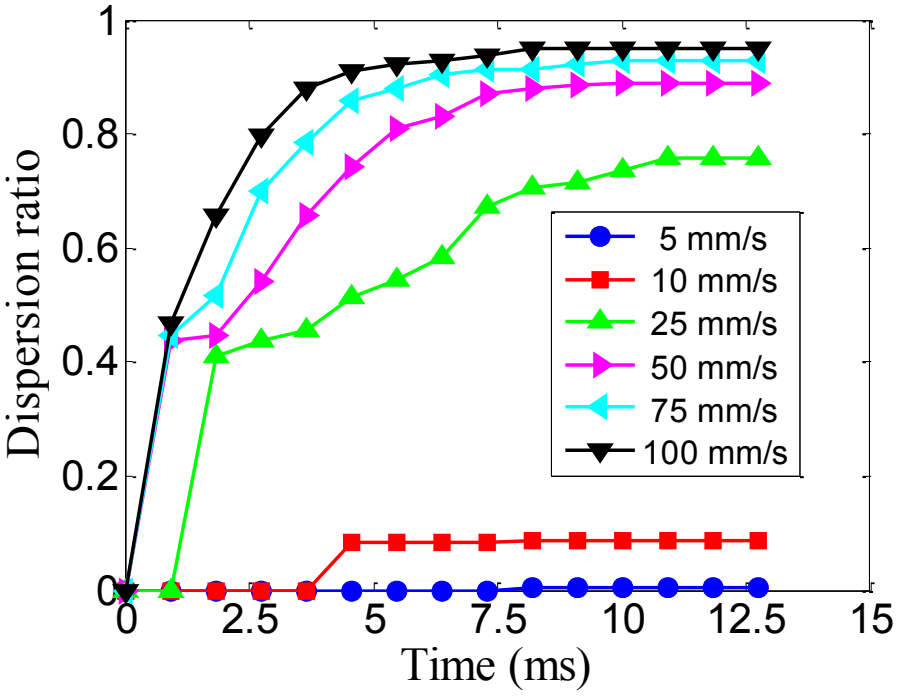

Fig. 6.5. The evolution of dispersion ratio with time (θ=45°, Γ=0.1 mJ/ m^2).

The effect of impact velocity on the dispersion ratio is shown in Fig. 6.6. For a given work of adhesion, the dispersion ratio increases with increasing impact velocity due to the higher impact energy; while for a given impact velocity, the dispersion ratio decreases with increasing work of adhesion resulting from the greater adhesion energy. This indicates that the dispersion ratio is the resultant effect of these two kinds of energy. It is also found that there is a saturated dispersion ratio, once it is reached, the effect of further increasing the impact velocity or decreasing the work of adhesion becomes insignificant. This might be because the API particles on the top of the carrier are difficult to disperse under the effect of the deceleration only, resulting in the saturate value.

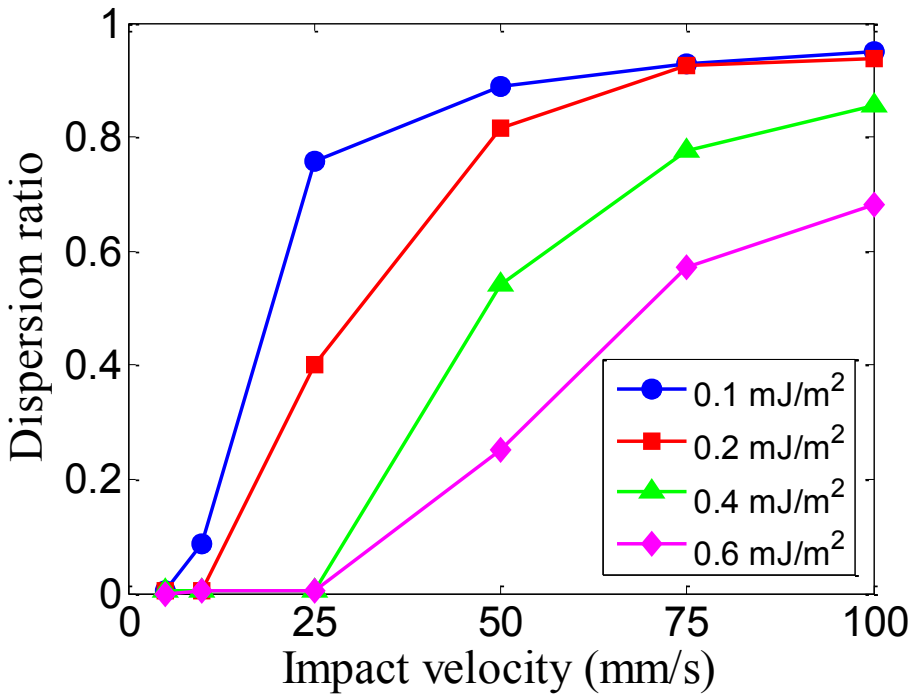

Fig. 6.6. The effect of impact velocity on the dispersion ratio (θ=45°).

The effect of impact angle on the dispersion ratio is shown in Fig. 6.7. For a given impact velocity and work of adhesion, the dispersion ratio increases with increasing impact angle. In other words, an impact at an impact angle of 90° can maximize the dispersion performance. Similar to the results shown in Fig. 6.6, the dispersion ratio decreases with increasing work of adhesion for a given impact angle.

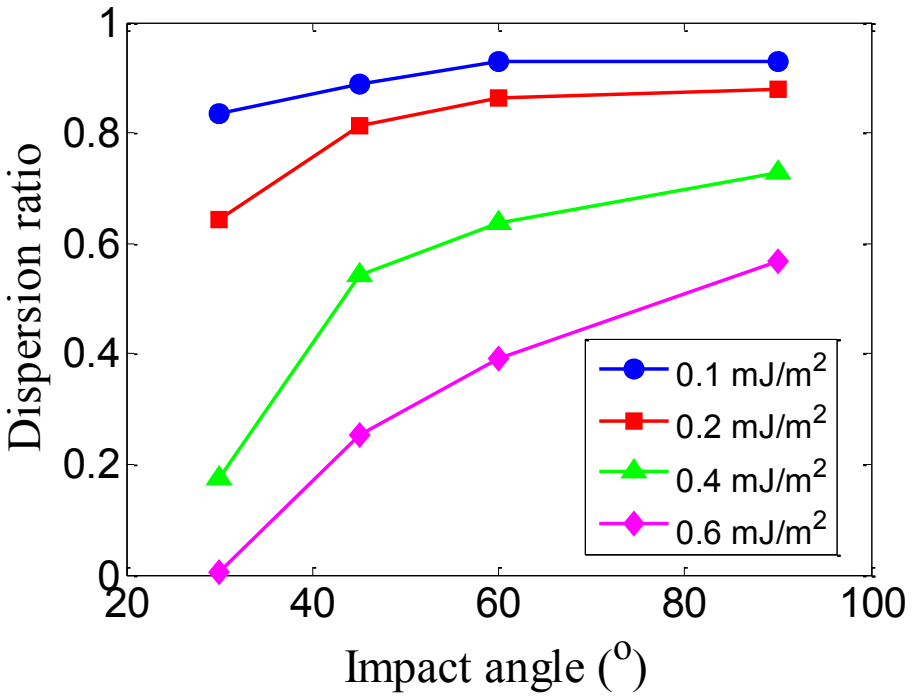

Fig. 6.7. The effect of impact angle on the dispersion ratio (V_i=50 mm/s).

The relationship between the dispersion ratio and the Weber number that is defined in Eq. (2.35) for cases with various impact velocity, impact angle and work of adhesion, is shown in Fig. 6.8. It is found that the dispersion ratio increases dramatically to a saturated value once the Weber number is larger than a critical value. This is consistent with previous findings (Moreno-Atanasio

and Ghadiri, 2006). However, the underlying mechanism behind this trend for carrier-based agglomerates might be different from those for drug-only agglomerates and it still needs further investigation.

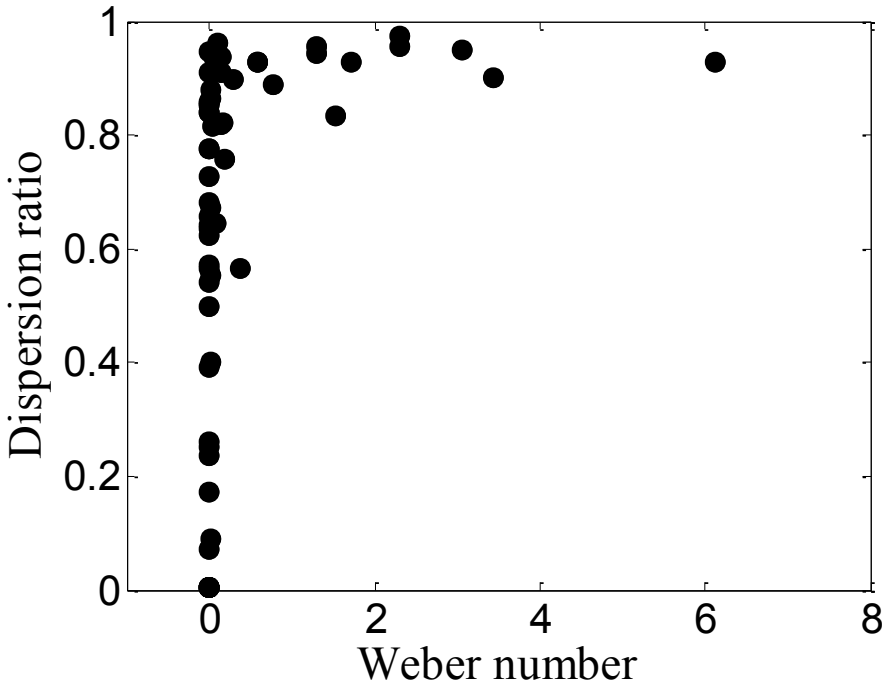

Fig. 6.8. Relationship between the dispersion ratio and Weber number.

The polar histograms (Zhang, 2003) for the contact orientation distribution are used to illustrate the preferential location for the API particles to detach from the carrier. The method to obtain the polar histograms can be found in our previous work (Yang *et al.*, 2014). The radius of each triangular band represents the residual ratio of API particles on that carrier surface area, i.e. the fraction of API particles still sticking on the carrier. The dashed circle line represents the residual ratio of 1. It can be found from Fig. 6.9 that for various impact velocities considered, all the API particles located on the lower hemisphere detach from

the carrier after impact. When the impact velocity is small, most of the API particles in the upper hemisphere remain on the surface of the carrier after impact. With the increase of impact velocity, the residual ratios of those bands near the equator decrease until all API particles in those areas detach. The polar histograms of the contact orientation distribution for varying impact angles are shown in Fig. 6.10. Similarly, with the increase of the impact angle, only the API particles in the upper hemisphere still stick on the carrier. It indicates that API particles in the near-wall regions are prone to be dispersed during the impact induced dispersion process.

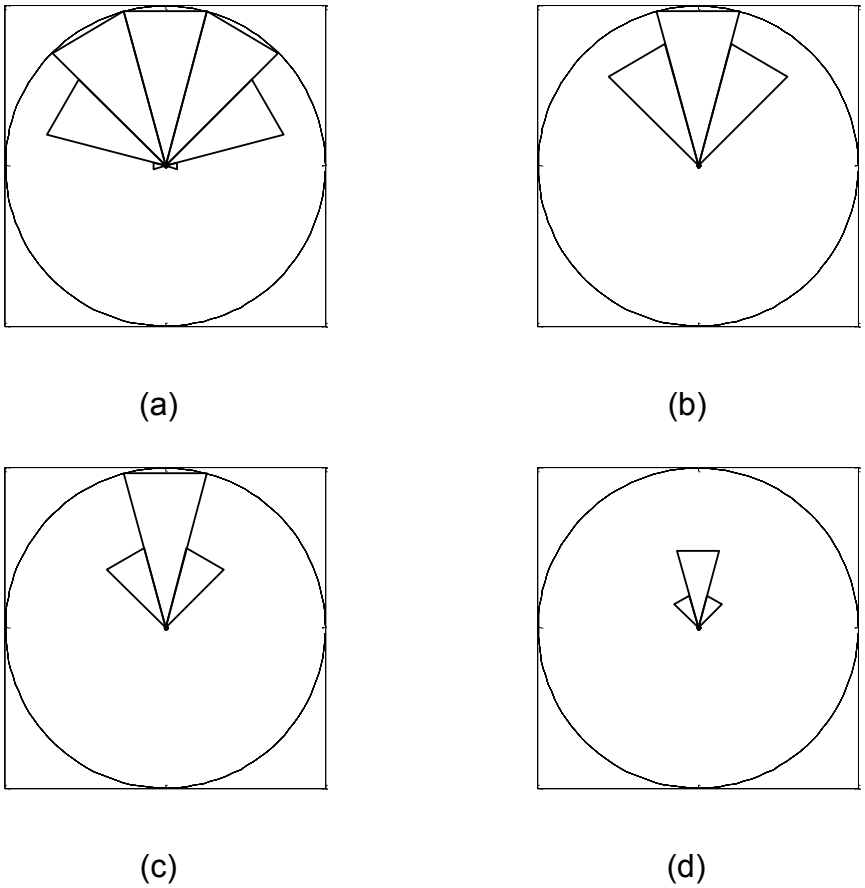

Fig. 6.9. Polar histograms of the contact orientation distribution for different impact velocities (θ=90°, Γ=0.2 mJ/ m^2); a) V_i=25 mm/s, b) V_i=50 mm/s, c) V_i=75 mm/s, d) V_i=100 mm/s.

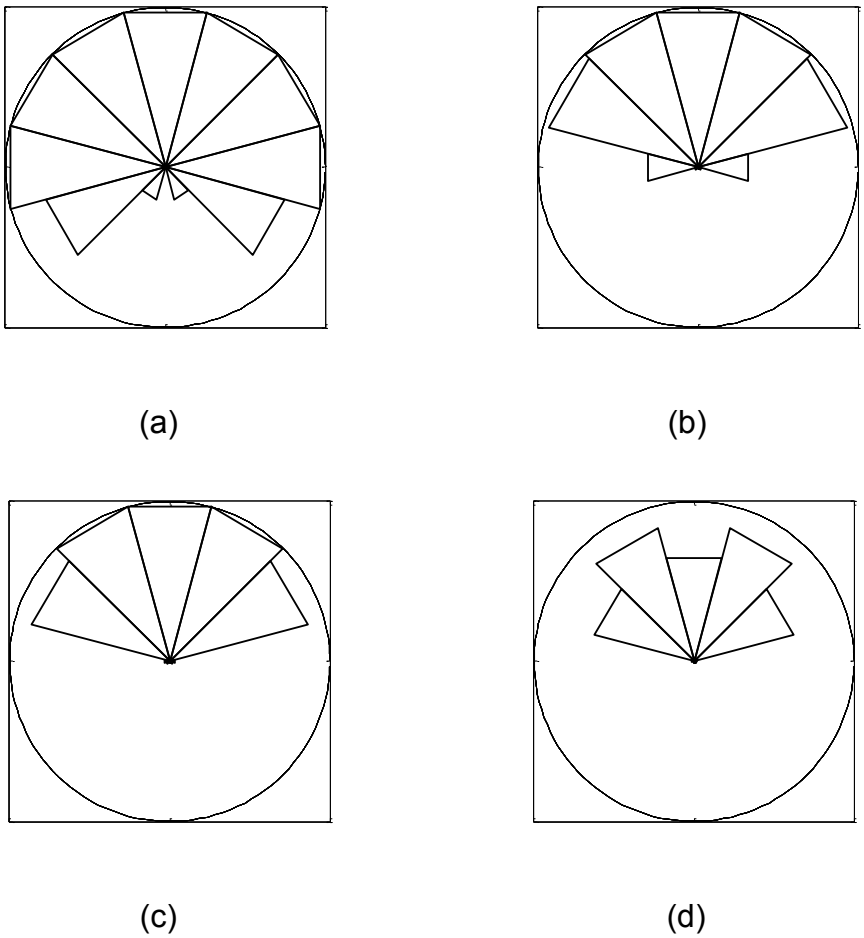

Fig. 6.10. Polar histograms of the contact orientation distribution for different impact angles (V_i=50 mm/s, Γ=0.4 mJ/ m^2); a) θ=30°, b) θ=45°, c) θ=60°, d) θ=90°.

As aforementioned, the dispersion performance is determined by the balance of the impact energy and the adhesion energy. Therefore, an energy ratio η is introduced as:

$$\eta = E_i / E_a \tag{6.6}$$

$$E_i = \frac{1}{2} m_{API} V_i^2 \tag{6.7}$$

$$E_a = 7.09\left(\frac{\Gamma^5 R^4}{E^{*2}}\right)^{1/3} \tag{6.8}$$

where E_i and E_a are the impact and adhesion energies of a single API particle, respectively. The impact energy is defined as the kinetic energy of the API particle; the adhesion energy is defined as the work to break the adhesive contact between the API particle and the carrier and was described by (Thornton and Ning, 1998). m_{API} is the mass of the API particle. Γ is the thermodynamic work of adhesion and R^* is the effective radius as described in Eq. (6.3) and Eq. (6.4). E^* is the effective Young's modulus that is defined as:

$$\frac{1}{E^*} = \frac{1-\nu_1^{\ 2}}{E_1} + \frac{1-\nu_2^{\ 2}}{E_2} \tag{6.9}$$

in which ν_1 and ν_2 are the Poisson's ratios of the particle 1 and 2, respectively.

The relationship between the dispersion ratio Φ and the energy ratio η is plotted in Fig. 6.11a. It can be found that the results of the dispersion ratio for all the cases with various impact velocities, impact angles and work of adhesion follow a similar trend. The dispersion ratio sharply increases with the energy ratio at the initial stage and then gradually reaches the saturated state. However, it can be also observed that there are some divergences among the cases with different impact angles, indicating that the impact angle plays an important role in the dispersion process as shown in Fig. 6.7.

It has been found from Fig. 6.7 that the dispersion ratio increases with increasing impact angle and an impact at an angle of 90° can maximize the dispersion performance. Hence, it is believed that the normal component of impact velocity plays the dominant role. Therefore, the impact velocity in the normal direction V_{in}, i.e. the normal impact velocity, rather than the impact velocity V_i, is also used to define the effective impact energy. The normal impact velocity is defined as:

$$V_{in} = V_i \sin\theta \tag{6.10}$$

where θ is the impact angle as shown in Fig. 6.1. Similar to Eqs. (6-6) and (6-7), we have:

$$\eta_n = E_{in} / E_a \tag{6.11}$$

$$E_{in} = \frac{1}{2} m_{API} V_{in}^{\ 2} \tag{6.12}$$

With the normal impact velocity, the variation of dispersion ratio Φ with energy ratio η_n is plotted in Fig. 6.11b. It can be seen that all the results superimpose onto a master curve. This implies that the impact induced dispersion is dominated by the normal impact velocity, which is consistent with previous findings (Moreno *et al.*, 2003; Samimi *et al.*, 2004).

The dispersion performance can also be approximated using the same cumulative Weibull distribution function as proposed in the previous work for airflow induced dispersion (Yang *et al.*, 2014):

$$\Phi = \begin{cases} 1 - \exp\left(-\left(\dfrac{\eta_n - \eta_0}{\lambda} \right)^{\kappa} \right), & \eta_n \geq \eta_0 \\ 0 \quad , & \eta_n < \eta_0 \end{cases} \tag{6.13}$$

The location parameter η_0, scale parameter λ, and the shape parameter κ are given in Table 6.2, in which corresponding values for airflow induced dispersion are also listed for comparison. It is supposed that these parameters could be related to evaluate the effects of formulation and device design in the future study.

Table 6.2. Fitting parameters of cumulative Weibull distribution function.

Parameters	Eq. (6.13)	Eq. (6.18)	Airflow induced
η_0	5.4×10^{2}	3.5×10^{-3}	0.61
λ	1.2×10^{3}	1.3×10^{-2}	0.80
κ	0.47	0.58	0.71
R^2	0.99	0.95	0.99

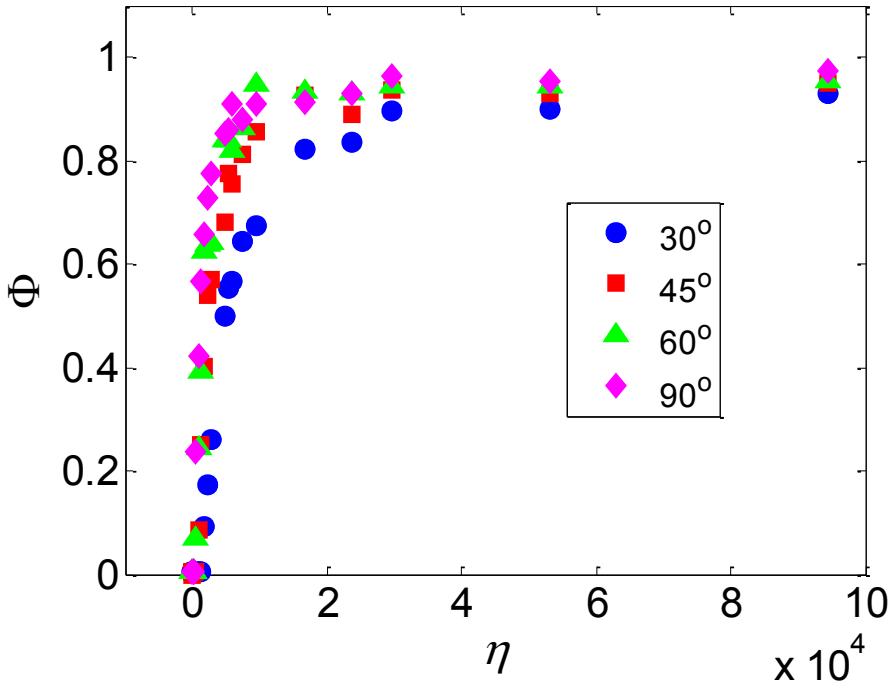

a)

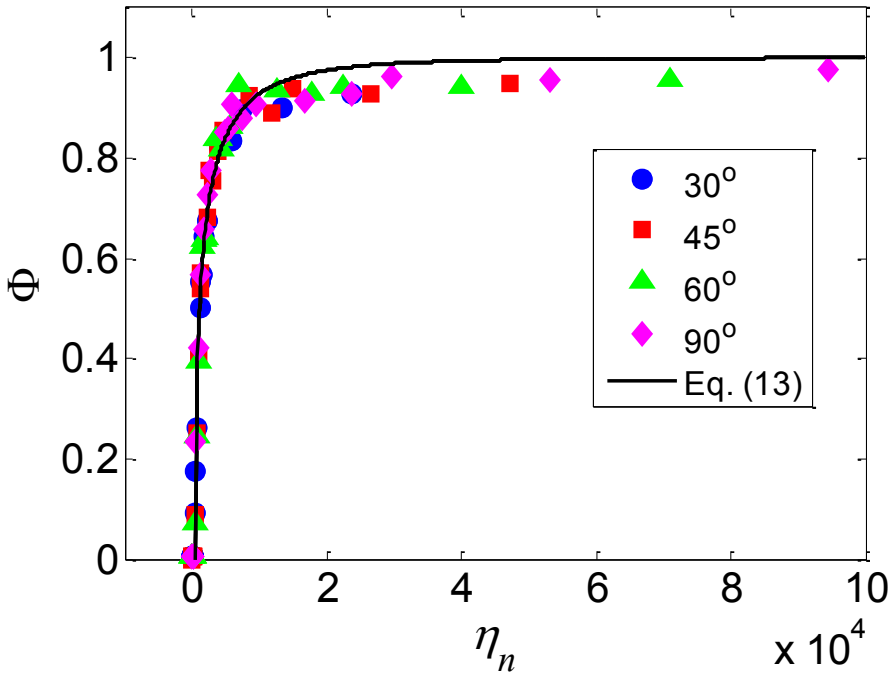

b)

Fig. 6.11. The variation of dispersion ratio with the energy ratio. a) with impact velocity; b) with normal impact velocity.

The above energy analysis is based on a single API particle. If the carrier-based agglomerate is considered as a whole, the normal impact energy is:

$$E_{in}' = \frac{1}{2}\left(m_c + Nm_{API}\right)V_{in}^{\ 2} \tag{6.14}$$

where m_c is the mass of the carrier particle and N is the number of API particles. For an agglomerate, the adhesion energy can be defined by (Tong *et al.*, 2010; Yang *et al.*, 2008):

$$E_a' = \sum_{i}^{M} r_i \left(\sum_{j=1}^{z_i} \mathbf{n}_{ij} \cdot \mathbf{F}_{ij} \right) \tag{6.15}$$

in which M is the total number of particles in the agglomerate. r_i is the radius of particle i, and z_i is the number of particle in contact with particle i. $\mathbf{n}_{ij}$ and $\mathbf{F_{ij}}$ are the unit vector connecting the centres of particle i and j and the contact force between particle i and j. In this study, if it is assumed that the contact force between two particles is the "pull-off" force F_c, Eq. (6.15) can be rewritten as:

$$E_a' = NF_c\left(r_c + r_{API}\right) \tag{6.16}$$

Then the overall energy ratio is defined as:

$$\eta_n' = E_{in}' / E_a' \tag{6.17}$$

The variation of dispersion ratio with the overall energy ratio is shown in Fig. 6.12. It can be seen that all the results follow a general trend and the cumulative Weibull distribution function can also be used to approximate the dispersion performance as:

$$\Phi = \begin{cases} 1 - \exp\left(-\left(\dfrac{\eta_n' - \eta_0}{\lambda} \right)^{\kappa} \right), & \eta_n' \geq \eta_0 \\ 0 \quad , & \eta_n' < \eta_0 \end{cases} \tag{6.18}$$

The fitting parameters are also given in Table 6.2. It can be found from comparing the parameters that, the values of shape parameter κ for the two methods are similar, indicating that the trends of the variation of dispersion ratio with energy ratio are similar. However, the value of location parameter η_0 in Eq. (6.18) is very small ($\approx$0), which is much smaller than that in Eq. (6.13). It is believed that from the perspective of an agglomerate, some of the API particles could detach from the carrier once the agglomerate impacts with the wall, even if the impact energy is small; while from the perspective of a single API particle, it can detach from the carrier only when its kinetic energy is large enough to break the contact with the carrier. From Thornton's derivation (Thornton and Ning, 1998) it can be found that the "large enough kinetic energy" is in the normal direction of the two contacting particles. In this study, the API particles stuck to the carrier are moving with the carrier; therefore the velocity in the normal direction of the contact is not high even if the impact velocity itself is sufficiently

high. Furthermore, the size of the carrier is much larger than that of the API particle and the kinetic energy of an agglomerate is much larger than that of a API particle. Therefore the value of the overall energy ratio for an agglomerate above which the dispersion ratio starts to increase is much smaller than that for a single API particle. Similar to the location parameter, the scale parameter λ in Eq. (6.18) is also much smaller than that in Eq. (6.13).

This study provides an insight into the fundamental micromechanics of dispersion processes for dry powder inhalers, which is a complicated problem demanding further investigation. It is addressed using an advanced numerical method, i.e. DEM, which is a methodology that has been developed over the last 35 years and has been widely used to analyse problems involving particles in many fields, based upon similar assumptions such as spherical particles. DEM is well recognized as a useful tool for exploring fundamental mechanisms since it provides the detailed information of particles positions, velocities, and the transient forces acting on particles, which correlates the macscopic behaviour with microscopic interactions (Zhu *et al.*, 2007a; Zhu *et al.*, 2008). The DEM code used has been validated for many applications (Guo *et al.*, 2013; Thornton and Yin, 1991) and it has also proved to be capable of modelling DPIs, such as the effects of van der Waals forces (Yang *et al.*, 2013b), electrostatic forces (Yang *et al.*, 2015), and drag forces caused by air flow (Yang *et al.*, 2014). Nevertheless, further study with more realistic particle properties should be performed in order to provide a more comprehensive understanding of dry

powder inhalation. Moreover, rigorous experimental validation will also be worth exploring further.

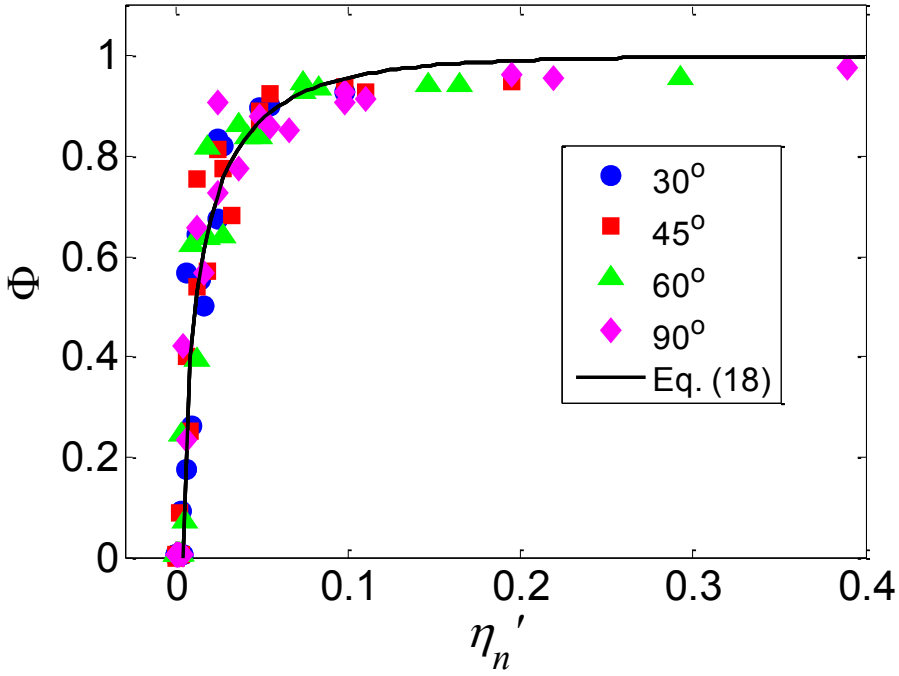

Fig. 6.12. The variation of dispersion ratio with the energy ratio from the perspective of the whole agglomerate.

6.4. Conclusions

The dispersion process during the impact of a carrier-based agglomerate and a wall at various impact conditions is modelled using DEM. It is shown that the dispersion process can be divided into two stages: i) a primary dispersion stage in which the dispersion ratio sharply increases with time; ii) a secondary dispersion where the dispersion ratio increases at a much slower rate. It is found that the API particles in the near-wall regions are prone to be dispersed. The

impact velocity, impact angle and work of adhesion all affect the dispersion performance: the dispersion ratio increases with increasing impact velocity and impact angle; while the dispersion ratio decreases with increasing work of adhesion. It is revealed that the normal component of the impact velocity plays a dominant role in the dispersion and the wall-particle impact induced dispersion for carrier-based DPI formulations can be well approximated using the cumulative Weibull distribution function governed by the ratio of the effective impact energy and adhesion energy.

CHAPTER 7: CONCLUSIONS AND FUTURE WORK

7.1 Conclusions

A discrete element method coupled with computational fluid mechanics (DEM-CFD) is employed to investigate the micromechanics of mixing and dispersion in carrier-based dry powder inhalers, including how the particles interact with each other and how other factors, such as mixing conditions, air flow, affect the interactions. Using DEM-CFD, this study explores the effects of van der Waals forces and electrostatic forces on the mixing process, and those of air flow and particle-wall impact on the dispersion process. The main findings are summarised here.

In order to investigate the effect of the van der Waals forces, JKR theory implemented into the DEM code is applied and a critical velocity criterion that determines the lowest impact velocity at which two elastic auto-adhesive spherical particles will rebound from each other during the impact is proposed based on the conservation of energy. Moreover, mixing of a carrier particle and API particles in a vibrating container is also explored. It is found that both the vibrational amplitude and frequency affect the mixing performance and there is an optimal vibration condition that maximise the mixing performance. A mechanism governed by the impact number, sticking efficiency and detachment number is proposed to describe this process and it is shown that the impact number and detachment number both increase with increasing vibrational amplitude and frequency while the sticking efficiency decreases with increasing vibrational amplitude and frequency.

The mixing process with electrostatic charges is further investigated. It is found that the mixing performance increases with increasing charge and decreases with increasing container size. The mixing performance also decreases with increasing vibration velocity amplitude and frequency. Moreover, a mechanism is proposed for the mixing process governed by the electrostatic force. However, for cases with electrostatic forces, while sticking efficiency and detachment number still affect the mixing performance, the impact number has no effect but the free API number, i.e. the number of API particles that are not in contact with the carrier, determines the mixing performance. This implies that long range and short range adhesive forces can result in different mixing behaviours.

The dispersion of API particles in DPIs is mainly affected by the air flow and particle-wall impact. Investigation of the dispersion of an agglomerate in a uniform flow showed that air flow can drag API particles away from the carrier and those in the downstream air flow regions are prone to be dispersed. It is found that the dispersion performance increases with increasing air velocity, and decreases with increasing work of adhesion. This implies that the DPI performance is controlled by the balance of the removal and adhesive forces and therefore a mechanism governed by the ratio of the fluid drag force to the pull-off force is proposed to describe the DPI performance using the cumulative Weibull distribution function.

The impact induced dispersion process is also investigated by considering the impact between an agglomerate and a wall. It is found that API particles in the

near-wall regions are more easily dispersed. It is also revealed that while the dispersion performance increases with increasing impact velocity and impact angle, indicating that the normal component of the impact velocity plays a dominant role in the dispersion, the dispersion performance decreases with increasing particle adhesion. Therefore, based on the balance of the adhesive and removal potentials, a mechanism that is governed by the ratio of the overall impact energy and adhesion energy is also proposed to describe the impact induced dispersion performance for carrier-based DPIs using the cumulative Weibull distribution function.

In summary, the performance of DPIs, including both mixing and dispersion behaviours, is determined by the balance of adhesive/cohesive and removal attempts. This study provides new insights in classifying the balance in four aspects, i.e. the effects of van der Waals forces, electrostatic forces, air flow and particle-wall impact, which could enhance the understanding of the underlying mechanism of DPIs.

7.2 Future work

Based on the improved understanding of the fundamental mechanics of the dry powder inhalers from this study, future work still needs to be conducted to better understand the mechanisms of the processes.

1) A more realistic formulation could be employed. Particles with irregular shapes (e.g. elongated carrier particle) and different materials (e.g. lactose for carrier particle and budesonide for API particle) can be generated to approximate the agglomerates. In addition, cohesion should also be considered. In that case, the effects of particle shape, density and porosity and surface roughness can be numerically investigated. The fragmentation and disintegration process can also be modelled.

2) More complicated inhaler structures could be constructed. DPI performance is collectively determined by many factors. Although we presented a few models in this study, they were normally for single factor or two competing factors. Constructing a more complicated inhaler allows us to explore the combined effects of these factors.

3) Since the size ratio in the carrier-based formulations is large, multi-scale models are needed to better characterise the interaction between carrier and API particles, and the interaction between air flow and particles.

4) Based on the more realistic formulation and inhaler, numerical results could be compared with and validated by experimental results.

5) Since the computational expenses for current cases are large, the expected improvement on modelled formulation and inhaler device and the increase of agglomerate number could considerably increase the computational expense.

Therefore, more efficient simulations, such as using parallel computing, are needed to enhance the usage of DEM.

References

Adi,H., Kwok,P.C.L., Crapper,J., Young,P.M., Traini,D., Chan,H.K., 2010. Does Electrostatic Charge Affect Powder Aerosolisation? Journal of Pharmaceutical Sciences, 99, 2455-2461.

Adi,S., Adi,H., Chan,H.K., Tong,Z., Yang,R., Yu,A., 2013. Effects of mechanical impaction on aerosol performance of particles with different surface roughness. Powder Technology, 236, 164-170.

Alderborn,G., Nystrom,C., 1996. Pharmaceutical Powder Compattion Technology. Marcel Dekker, Inc..

Anderson,T.B., Jackson,R.A., 1967a. A fluid mechanical description of fluidized beds. Industrial & Engineering Chemistry Fundamentals, 6, 527-539.

Anderson,T., Jackson,R., 1967b. Fluid Mechanical Description of Fluidized Beds. Equations of Motion. Industrial & Engineering Chemistry Fundamentals, 6, 527-539.

Aulton,M.E., Taylor,K., 2001. Pharmaceutics: The Science of Dosage Form Design. 2 Ed., Churchill Livingstone, Edinburgh.

Boerefijn,R., Ning,Z., Ghadiri,M., 1998. Disintegration of weak lactose agglomerates for inhalation applications. International Journal of Pharmaceutics, 172, 199-209.

Calvert,G., Hassanpour,A., Ghadiri,M., 2009. Mechanistic Analysis and Computer Simulation of the Aerodynamic Dispersion of Loose Aggregates: Effect of Surface Energy. Powders and Grains 2009, 1145, 1047-1050.

Calvert,G., Hassanpour,A., Ghadiri,M., 2013. Analysis of aerodynamic dispersion of cohesive clusters. Chemical Engineering Science, 86, 146-150.

Calvert,G., Hassanpour,A., Ghadiri,M., 2011. Mechanistic analysis and computer simulation of the aerodynamic dispersion of loose aggregates. Chemical Engineering Research & Design, 89, 519-525.

Carter,P.A., Rowley,G., Fletcher,E.J., Stylianopoulos,V., 1998. Measurement of electrostatic charge decay in pharmaceutical powders and polymer materials used in dry powder inhaler devices. Drug Development and Industrial Pharmacy, 24, 1083-1088.

Clark,A.R., 1995. Medical Aerosol Inhalers - Past, Present, and Future. Aerosol Science and Technology, 22, 374-391.

Cline,D., Dalby,R., 2002. Predicting the quality of powders for inhalation from surface energy and area. Pharmaceutical Research, 19, 1274-1277.

Coates,M.S., Chan,H.K., Fletcher,D.F., Raper,J.A., 2005a. Influence of air flow on the performance of a dry powder inhaler using computational and experimental analyses. Pharmaceutical Research, 22, 1445-1453.

Coates,M.S., Chan,H.K., Fletcher,D.F., Raper,J.A., 2006. Effect of design on the performance of a dry powder inhaler using computational fluid dynamics. Part 2: Air inlet size. Journal of Pharmaceutical Sciences, 95, 1382-1392.

Coates,M.S., Fletcher,D.F., Chan,H.K., Raper,J.A., 2004. Effect of design on the performance of a dry powder inhaler using computational fluid dynamics. Part 1: Grid structure and mouthpiece length. Journal of Pharmaceutical Sciences, 93, 2863-2876.

Coates,M.S., Fletcher,D.F., Chan,H.K., Raper,J.A., 2005b. The role of capsule on the performance of a dry powder inhaler using computational and experimental analyses. Pharmaceutical Research, 22, 923-932.

Coates,M.S., Chan,H.K., Fletcher,D.F., Chiou,H., 2007. Influence of mouthpiece geometry on the aerosol delivery performance of a dry powder inhaler. Pharmaceutical Research, 24, 1450-1456.

Cook,B.K., Noble,D.R., Williams,J.R., 2004. A direct simulation method for particle-fluid systems. Engineering Computations, 21, 151-168.

Cundall,P.A., Strack,O.D.L., 1979. A discrete numerical model for granular assemblies. Geotechnique, 29, 47-65.

De Boer,A.H., Hagedoorn,P., Gjaltema,D., Goede,J., Frijlink,H.W., 2003. Air classifier technology (ACT) in dry powder inhalation - Part I. Introduction of a novel force distribution concept (FDC) explaining the performance of a basic

air classifier on adhesive mixtures. International Journal of Pharmaceutics, 260, 187-200.

De Boer,A.H., Hagedoorn,P., Gjaltema,D., Lambregts,D., Irngartinger,M., Frijlink,H.W., 2004. The rate of drug particle detachment from carrier crystals in an air classifier-based inhaler. Pharmaceutical Research, 21, 2158-2166.

Derjaguin,B.V., Muller,V.M., Toporov,Y.P., 1975. Effect of contact deformation on the adhesion of particles. Journal of Colloid Interface Science, 53, 314-326.

Di felice,R., 1994. The Voidage Function for Fluid Particle Interaction Systems. International Journal of Multiphase Flow, 20, 153-159.

Dickhoff,B.H.J., De Boer,A.H., Lambregts,D., Frijlink,H.W., 2003. The effect of carrier surface and bulk properties on drug particle detachment from crystalline lactose carrier particles during inhalation, as function of carrier payload and mixing time. European Journal of Pharmaceutics and Biopharmaceutics, 56, 291-302.

Donovan,M.J., Kim,S.H., Raman,V., Smyth,H.D., 2012. Dry powder inhaler device influence on carrier particle performance. Journal of Pharmaceutical Sciences, 101, 1097-1107.

Everard,M.L., Devadason,S.G., LeSouef,P.N., 1997. Flow early in the inspiratory manoeuvre affects the aerosol particle size distribution from a Turbuhaler. Respiratory Medicine, 91, 624-628.

Favier,J.F., Abbaspour-Fard,M.H., Kremmer,M., Raji,A.O., 1999. Shape representation of axisymmetrical, non-spherical particles in discrete element simulation using multi-element model particles. Engineering Computations, 16, 467-480.

Fisher,R.A., 1926. On the capillary forces in an ideal soil, correction of formulate given by W.B. Haines. Journal of Agricultural Science, 16, 492-505.

Frijlink,H.W., De Boer,A.H., 2004. Dry powder inhalers for pulmonary drug delivery. Expert opinion on drug delivery, 1, 67-86.

Ge,W., Li,J.H., 2001. Macro-scale pseudo-particle modeling for particle-fluid systems. Chinese Science Bulletin, 46, 1503-1507.

Ge,W., Li,J.H., 2003. Simulation of particle-fluid systems with macro-scale pseudo-particle modeling. Powder Technology, 137, 99-108.

Gotoh,K., Masuda,H., Higashitani,K., 2006. Dispersion of Particles. In: Masuda,H., Higashitani,K., Yoshida,H. (Eds.), CRC Press, 449-456.

Guenette,E., Barrett,A., Kraus,D., Brody,R., Harding,L., Magee,G., 2009. Understanding the effect of lactose particle size on the properties of DPI formulations using experimental design. International Journal of Pharmaceutics, 380, 80-88.

Guo,Y., Wu,C., Thornton,C., 2013. Modeling Gas-Particle Two-Phase Flows with Complex and Moving Boundaries using DEM-CFD with an Immersed Boundary Method. Aiche Journal, 59, 1075-1087.

Hamaker,H.C., 1937. The London-van der Waals attraction between spherical particles. Physica (Amsterdam), 4, 1058-1072.

Hassan,M.S., Lau,R., 2010. Inhalation performance of pollen-shape carrier in dry powder formulation with different drug mixing ratios: Comparison with lactose carrier. International Journal of Pharmaceutics, 386, 6-14.

Heng,D., Lee,S.H., Ng,W.K., Chan,H.K., Kwek,J.W., Tan,R.B., 2013. Novel alternatives to reduce powder retention in the dry powder inhaler during aerosolization. International Journal of Pharmaceutics, 452, 194-200.

Hertz,H., 1882. Uber die Beruhrung fester elastischer Korper. Journal fur die reine und angewandte Mathematik, 92, 156-171.

Hinds,W.C., 1999. Aerosol Technology, Properties, Behavior, and Measurement of Airborne Particles. Wiley, New York.

Hoehner,D., Wirtz,S., Kruggel-Emden,H., Scherer,V., 2011. Comparison of the multi-sphere and polyhedral approach to simulate non-spherical particles within the discrete element method: Influence on temporal force evolution for multiple contacts. Powder Technology, 208, 643-656.

Hogue,C., 1998. Shape representation and contact detection for discrete element simulations of arbitrary geometries. Engineering Computations, 15, 374-390.

Hu,H.H., 1996. Direct simulation of flows of solid-liquid mixtures. International Journal of Multiphase Flow, 22, 335-352.

Islam,N., Gladki,E., 2008. Dry powder inhalers (DPIs) - A review of device reliability and innovation. International Journal of Pharmaceutics, 360, 1-11.

Jashnani,R.N., Byron,P.R., Dalby,R.N., 1995. Testing of Dry Powder Aerosol Formulations in Different Environmental-Conditions. International Journal of Pharmaceutics, 113, 123-130.

Johnson,K.L., 1985. Contact Mechanics. Cambridge University Press, Cambridge.

Johnson,K.L., Kendall,K., Roberts,A.D., 1971. Surface Energy and the Contact of Elastic Solids. Proceedings of the Royal Society of London Series A, 324, 301-313.

Jones,M.D., Price,R., 2006. The influence of fine excipient particles on the performance of carrier-based dry powder inhalation formulations. Pharmaceutical Research, 23, 1665-1674.

Kafui,K.D., Thornton,C., 2000. Numerical simulations of impact breakage of a spherical crystalline agglomerate. Powder Technology, 109, 113-132.

Kafui,K.D., Thornton,C., Adams,M.J., 2002. Discrete particle-continuum fluid modelling of gas-solid fluidised beds. Chemical Engineering Science, 57, 2395-2410.

Kaialy,W., Alhalaweh,A., Velaga,S.P., Nokhodchi,A., 2011. Effect of carrier particle shape on dry powder inhaler performance. International Journal of Pharmaceutics, 421, 12-23.

Kaialy,W., Alhalaweh,A., Velaga,S.P., Nokhodchi,A., 2012a. Influence of lactose carrier particle size on the aerosol performance of budesonide from a dry powder inhaler. Powder Technology, 227, 74-85.

Kaialy,W., Hussain,T., Alhalaweh,A., Nokhodchi,A., 2014. Towards a More Desirable Dry Powder Inhaler Formulation: Large Spray-Dried Mannitol Microspheres Outperform Small Microspheres. Pharmaceutical Research, 31, 60-76.

Kaialy,W., Martin,G.P., Larhrib,H., Ticehurst,M.D., Kolosionek,E., Nokhodchi,A., 2012b. The influence of physical properties and morphology of crystallised lactose on delivery of salbutamol sulphate from dry powder inhalers. Colloids and Surfaces B-Biointerfaces, 89, 29-39.

Kaialy,W., Nokhodchi,A., 2012. Antisolvent crystallisation is a potential technique to prepare engineered lactose with promising aerosolisation properties: Effect of saturation degree. International Journal of Pharmaceutics, 437, 57-69.

Kaialy,W., Nokhodchi,A., 2013. Engineered mannitol ternary additives improve dispersion of lactose-salbutamol sulphate dry powder inhalations. Aaps Journal, 15, 728-743.

Kaialy,W., Ticehurst,M., Nokhodchi,A., 2012c. Dry powder inhalers: Mechanistic evaluation of lactose formulations containing salbutamol sulphate. International Journal of Pharmaceutics, 423, 184-194.

Karner,S., Urbanetz,N.A., 2011. The impact of electrostatic charge in pharmaceutical powders with specific focus on inhalation-powders. Journal of Aerosol Science, 42, 428-445.

Karner,S., Urbanetz,N.A., 2012. Arising of electrostatic charge in the mixing process and its influencing factors. Powder Technology, 226, 261-268.

Karner,S., Urbanetz,N.A., 2013. Triboelectric characteristics of mannitol based formulations for the application in dry powder inhalers. Powder Technology, 235, 349-358.

Kodam,M., Bharadwaj,R., Curtis,J., Hancock,B., Wassgren,C., 2009. Force model considerations for glued-sphere discrete element method simulations. Chemical Engineering Science, 64, 3466-3475.

Latham,J.P., Munjiza,A., 2004. The modelling of particle systems with real shapes. Philosophical Transactions of the Royal Society of London Series A-Mathematical Physical and Engineering Sciences, 362, 1953-1972.

Le,V., Thi,T., Robins,E., Flament,M., 2012. Dry Powder Inhalers: Study of the Parameters Influencing Adhesion and Dispersion of Fluticasone Propionate. Aaps Pharmscitech, 13, 477-484.

Lin,X., Ng,T.T., 1997. A three-dimensional discrete element model using arrays of ellipsoids. Geotechnique, 47, 319-329.

Louey,M.D., Mulvaney,P., Stewart,P.J., 2001. Characterisation of adhesional properties of lactose carriers using atomic force microscopy. Journal of Pharmaceutical and Biomedical Analysis, 25, 559-567.

Mindlin,R.D., Deresiewicz,H., 1953. Elastic spheres in contact under varying oblique forces. Journal of Applied Mechanics, 20, 327-344.

Mishra,B.K., Thornton,C., 2001. Impact breakage of particle agglomerates. International Journal of Mineral Processing, 61, 225-239.

Moreno,R., Ghadiri,M., Antony,S.J., 2003. Effect of the impact angle on the breakage of agglomerates: a numerical study using DEM. Powder Technology, 130, 132-137.

Moreno-Atanasio,R., Ghadiri,M., 2006. Mechanistic analysis and computer simulation of impact breakage of agglomerates: Effect of surface energy. Chemical Engineering Science, 61, 2476-2481.

Newman,S.P., Busse,W.W., 2002. Evolution of dry powder inhaler design, formulation, and performance. Respiratory Medicine, 96, 293-304.

Newman,S.P., Moren,F., Trofast,E., Talaee,N., Clarke,S.W., 1989. Deposition and Clinical Efficacy of Terbutaline Sulfate from Turbuhaler, A New Multi-Dose Powder Inhaler. European Respiratory Journal, 2, 247-252.

Ning,Z., Boerefijn,R., Ghadiri,M., Thornton,C., 1997a. Distinct element simulation of impact breakage of lactose agglomerates. Advanced Powder Technology, 8, 15-37.

Ning,Z., Boerefijn,R., Ghadiri,M., Thornton,C., 1997b. Distinct element simulation of impact breakage of lactose agglomerates. Advanced Powder Technology, 8, 15-37.

Nwose,E.N., Pei,C., Wu,C.Y., 2012. Modelling die filling with charged particles using DEM/CFD. Particuology, 10, 229-235.

Pan,T.W., Joseph,D.D., Bai,R., Glowinski,R., Sarin,V., 2002. Fluidization of 1204 spheres: simulation and experiment. Journal of Fluid Mechanics, 451, 169-191.

Papoulis,A., Pillai,S.U., 2002. Probability, Random Variables And Stochastic Processes. 4 Ed., McGraw-Hill Education (India) Pvt Limited.

Pauwels,R., Newman,S., Borgstrom,L., 1997. Airway deposition and airway effects of antiasthma drugs delivered from metered-dose inhalers. European Respiratory Journal, 10, 2127-2138.

Pei,C., Wu,C.Y., Byard,S., England,D., 2010. Numerical analysis of electrostatic effects during powder deposition using DEM/CFD. Journal of Pharmacy and Pharmacology, 62, 1454-1455.

Pritchard,J.N., 2001. The influence of lung deposition on clinical response. Journal of Aerosol Medicine, 14, S19-S26.

Pu,Y., Mazumder,M., Cooney,C., 2009. Effects of Electrostatic Charging on Pharmaceutical Powder Blending Homogeneity. Journal of Pharmaceutical Sciences, 98, 2412-2421.

Rabbani,N.R., Seville,P.C., 2005. The influence of formulation components on the aerosolisation properties of spray-dried powders. Journal of Controlled Release, 110, 130-140.

Saleem,I., Smyth,H., Telko,M., 2008. Prediction of dry powder inhaler formulation performance from surface energetics and blending dynamics. Drug Development and Industrial Pharmacy, 34, 1002-1010.

Samimi,A., Moreno,R., Ghadiri,M., 2004. Analysis of impact damage of agglomerates: effect of impact angle. Powder Technology, 143, 97-109.

Savkoor,A.R., Briggs,G.A.D., 1977. The effect of tangential force on the contact of elastic solids. Proceedings of the Royal Society of London Series A, 356, 103-114.

Selvam,P., Marek,S., Truman,C., McNair,D., Smyth,H.D., 2011. Micronized Drug Adhesion and Detachment from Surfaces: Effect of Loading Conditions. Aerosol Science and Technology, 45, 81-87.

Seville,J.P.K., Tuzun,U., Clift,R., 1997. Processing of Particulate Solids. Blackie Academic & Professional.

Shinohara,K., Oida,M., Golman,B., 2000. Effect of particle shape on angle of internal friction by triaxial compression test. Powder Technology, 107, 131-136.

Shur,J., Kubavat,H.A., Ruecroft,G., Hipkiss,D., Price,R., 2012. Influence of crystal form of ipratropium bromide on micronisation and aerosolisation behaviour in dry powder inhaler formulations. Journal of Pharmacy and Pharmacology, 64, 1326-1336.

Smith,I.J., Parry-Billings,M., 2003. The inhalers of the future? A review of dry powder devices on the market today. Pulmonary Pharmacology & Therapeutics, 16, 79-95.

Steckel,H., Bolzen,N., 2004. Alternative sugars as potential carriers for dry powder inhalations. International Journal of Pharmaceutics, 270, 297-306.

Steckel,H., Muller,B.W., 1997. In vitro evaluation of dry powder inhalers .2. Influence of carrier particle size and concentration on in vitro deposition. International Journal of Pharmaceutics, 154, 31-37.

Thornton,C., Ciomocos,M.T., Adams,M.J., 1999. Numerical simulations of agglomerate impact breakage. Powder Technology, 105, 74-82.

Thornton,C., Liu,L.F., 2004. How do agglomerates break? Powder Technology, 143, 110-116.

Thornton,C., Ning,Z.M., 1998. A theoretical model for the stick/bounce behaviour of adhesive, elastic-plastic spheres. Powder Technology, 99, 154-162.

Thornton,C., Yin,K.K., 1991. Impact of Elastic Spheres with and Without Adhesion. Powder Technology, 65, 153-166.

Thornton,C., Yin,K.K., Adams,M.J., 1996. Numerical simulation of the impact fracture and fragmentation of agglomerates. Journal of Physics D-Applied Physics, 29, 424-435.

Tong,Z., Adi,S., Yang,R., Chan,H., Yu,A., 2011. Numerical investigation of the de-agglomeration mechanisms of fine powders on mechanical impaction. Journal of Aerosol Science, 42, 811-819.

Tong,Z., Yang,R., Chu,K., Yu,A., Adi,S., Chan,H., 2010. Numerical study of the effects of particle size and polydispersity on the agglomerate dispersion in a cyclonic flow. Chemical Engineering Journal, 164, 432-441.

Tong,Z., Yang,R., Yu,A., Adi,S., Chan,H., 2009. Numerical modelling of the breakage of loose agglomerates of fine particles. Powder Technology, 196, 213-221.

Tong,Z., Zheng,B., Yang,R., Yu,A., Chan,H., 2013. CFD-DEM investigation of the dispersion mechanisms in commercial dry powder inhalers. Powder Technology, 240, 19-24.

Vidgren,M., Karkkainen,A., Karjalainen,P., Paronen,P., Nuutinen,J., 1988. Effect of Powder Inhaler Design on Drug Deposition in the Respiratory-Tract. International Journal of Pharmaceutics, 42, 211-216.

Voss,A., Finlay,W.H., 2002. Deagglomeration of dry powder pharmaceutical aerosols. International Journal of Pharmaceutics, 248, 39-50.

W.C.Hinds, 1999. Aerosol Technology, Properties, Behavior, and Measurement of Airborne Particles. John willey & Sons, Inc.

Wong,W., Fletcher,D.F., Traini,D., Chan,H.K., Crapper,J., Young,P.M., 2010. Particle Aerosolisation and Break-up in Dry Powder Inhalers 1: Evaluation and Modelling of Venturi Effects for Agglomerated Systems. Pharmaceutical Research, 27, 1367-1376.

Wong,W., Fletcher,D.F., Traini,D., Chan,H.K., Crapper,J., Young,P.M., 2011. Particle Aerosolisation and Break-Up in Dry Powder Inhalers: Evaluation and Modelling of Impaction Effects for Agglomerated Systems. Journal of Pharmaceutical Sciences, 100, 2744-2754.

Wong,W., Fletcher,D.F., Traini,D., Chan,H.K., Young,P.M., 2012. The use of computational approaches in inhaler development. Advanced Drug Delivery Reviews, 64, 312-322.

Wu,C., Zhan,J., Li,Y., Lam,K., 2006. Dense particulate flow model on unstructured mesh. Chemical Engineering Science, 61, 5726-5741.

Yang,J., Wu,C.Y., Adams,M., 2013a. DEM Analysis of Effects of Particle Properties and Mixing Conditions on Particle Attachment Processes. AIP Conference Proceedings, 1542, 967-970.

Yang,J., Wu,C.Y., Adams,M., 2013b. DEM analysis of particle adhesion during powder mixing for dry powder inhaler formulation development. Granular Matter, 15, 417-426.

Yang,J., Wu,C.Y., Adams,M., 2014. Three-dimensional DEM-CFD analysis of air-flow induced detachment of API particles from carrier particles in dry powder inhalers. Acta Pharmaceutica Sinica B, 4, 52-59.

Yang,J., Wu,C.Y., Adams,M., 2015. DEM analysis of the effect of electrostatic interaction on particle mixing for carrier-based dry powder inhaler formulations. Particuology.

Yang,R., Yu,A., Choi,S., Coates,M., Chan,H., 2008. Agglomeration of fine particles subjected to centripetal compaction. Powder Technology, 184, 122-129.

Young,P.A., Edge,S., Traini,D., Jones,M.D., Price,R., El-Sabawi,D., Urry,C., Smith,C., 2005. The influence of dose on the performance of dry powder inhalation systems. International Journal of Pharmaceutics, 296, 26-33.

Young,P.M., Roberts,D., Chiou,H., Rae,W., Chan,H.K., Traini,D., 2008. Composite carriers improve the aerosolisation efficiency of drugs for respiratory delivery. Journal of Aerosol Science, 39, 82-93.

Zeng,X.M., Martin,G.P., Tee,S.K., Abu Ghoush,A., Marriott,C., 1999. Effects of particle size and adding sequence of fine lactose on the deposition of salbutamol sulphate from a dry powder formulation. International Journal of Pharmaceutics, 182, 133-144.

Zhang, Ling. The Behaviour of Granular Material in Pure Shear, Dieect Shear and Simple Shear. PhD Thesis, 2003. Aston University.

Zhou,H., Flamant,G., Gauthier,D., Lu,J., 2004a. Numerical simulation of the turbulent gas-particle flow in a fluidized bed by an LES-DPM model. Chemical Engineering Research & Design, 82, 918-926.

Zhou,H.S., Flamant,G., Gauthier,D., 2004b. DEM-LES of coal combustion in a bubbling fluidized bed. Part I: gas-particle turbulent flow structure. Chemical Engineering Science, 59, 4193-4203.

Zhou,H.S., Flamant,G., Gauthier,D., 2004c. DEM-LES simulation of coal combustion in a bubbling fluidized bed Part II: coal combustion at the particle level. Chemical Engineering Science, 59, 4205-4215.

Zhou,Q.T., Tong,Z., Tang,P., Citterio,M., Yang,R., Chan,H.K., 2013. Effect of Device Design on the Aerosolization of a Carrier-Based Dry Powder Inhaler-a Case Study on Aerolizer(A (R)) Foradile(A (R)). Aaps Journal, 15, 511-522.

Zhu,H., Zhou,Z., Yang,R., Yu,A., 2007a. Discrete particle simulation of particulate systems: Theoretical developments. Chemical Engineering Science, 62, 3378-3396.

Zhu,H., Zhou,Z., Yang,R., Yu,A., 2008. Discrete particle simulation of particulate systems: A review of major applications and findings. Chemical Engineering Science, 63, 5728-5770.

Zhu,K., Tan,R.B., Chen,F., Ong,K.H., Heng,P.W., 2007b. Influence of particle wall adhesion on particle electrification in mixers. International Journal of Pharmaceutics, 328, 22-34.